Measuring magnetic field dynamics in non-equilibrium superconductors

DISSERTATION

zur Erlangung des Doktorgrades
an der Fakultät für Mathematik, Informatik und Naturwissenschaften

Fachbereich Physik

DER UNIVERSITÄT HAMBURG

vorgelegt von

Giovanni De Vecchi

Hamburg

2024

Gutachter/innen der Dissertation:	Prof. Dr. Andrea Cavalleri Prof. Dr. Henning Moritz
Zusammensetzung der Prüfungskommission:	Prof. Dr. Andrea Cavalleri Prof. Dr. Henning Moritz Prof. Dr. Martin Eckstein Prof. Dr. Michael A. Rübhausen Prof. Dr. Ludwig Mathey
Vorsitzende/r der Prüfungskommission:	Prof. Dr. Ludwig Mathey
Datum der Disputation:	27.03.2025
Vorsitzender des Fach-Promotionsausschusses PHYSIK:	Prof. Dr. Markus Drescher

Leiter des Fachbereichs PHYSIK: Prof. Dr. Wolfgang J. Parak

Dekan der Fakultät MIN: Prof. Dr.-Ing. Norbert Ritter

Declaration on oath

I hereby declare and affirm that this doctoral dissertation is my own work and that I have not used any aids and sources other than those indicated.

If electronic resources based on generative artificial intelligence (gAI) were used in the course of writing this dissertation, I confirm that my own work was the main and value-adding contribution and that complete documentation of all resources used is available in accordance with good scientific practice. I am responsible for any erroneous or distorted content, incorrect references, violations of data protection and copyright law or plagiarism that may have been generated by the gAI.

Giovanni De Vecchi
Hamburg, den 13.11.2024

Giovanni De Vecchi

Signature of doctoral candidate

To Antonio.

Abstract

Tuning material properties to create new functionalities is one of the main drivers for society's technological developments. Quantum materials are an up-and-coming candidate for this goal, given the many coexisting and competing phases they host. Their peculiarity is that they are very susceptible to external stimuli, which induce different phases characterized by specific properties and technologically relevant functionalities. A task of condensed matter physics is to understand these new phases of matter and technologically exploit them. Superconductivity is a striking example of a macroscopic manifestation of quantum physics at macroscopic scales. Superconductors can carry currents without losses and, as such, can revolutionize our way of living. Unfortunately, a wide-scale application of superconductivity is impractical due to the low temperatures at which this phenomenon appears. Therefore, a race has started to engineer materials with consistently higher superconducting temperatures, hoping to achieve a superconductor working at room temperature one day.

An alternative approach is using light to access new and sometimes hidden phases in quantum materials. Advancements in laser physics allow us to generate intense light pulses that couple selectively to collective modes in the material responsible for changing the material properties. For example, coherent excitation of specific phonon modes using far- and mid-infrared laser pulses effectively changes the material's structural or electronic properties, achieving extreme transient conditions that cannot be replicated in an equilibrium setting.

Pioneering experiments at the crossroads between laser physics and condensed matter employed advanced optical sources to demonstrate light control of ferroelectricity, magnetism, topology, and superconductivity. This thesis focuses on the control of superconductivity with ultrafast mid-infrared light pulses. These intense pulses have been shown previously to induce transient dissipationless transport features in various classes of materials. Underdoped cuprates, irradiated with light resonant with specific phonon modes, show superconducting-like features in their conductivity spectra at THz frequencies. This work aims to provide additional information about the magnetic dynamics of these transient states. Inspired by the similarities between their transient conductivity and the transport properties of equilibrium superconductors, we ask: will these photo-excited phases show transient Meissner-like magnetic field expulsion in analogy to their equilibrium counterpart?

We developed an ultrafast optical magnetometry technique to measure magnetic fields with sub-microtesla precision and sub-picosecond time resolution to answer this question. This experimental method draws and builds on previous realizations of optical techniques to measure the magnetization of superconductors, extending them to the ultrafast domain. *Ultrafast optical magnetometry*

is a non-invasive approach that relies on a spectator magneto-optic detector placed in closed contact with the photo-excited region, acting as a transducer of the local magnetic field in the detector volume into a precisely measurable polarization rotation. Our measurement results on an underdoped $\mathrm{YBa_2Cu_3O_{6.48}}$ bulk sample reveal a magnetic transient compatible with a transient diamagnetic susceptibility as high as 30%. This result is not explainable, assuming a mere conductivity increase after mid-infrared excitation, but requires some superconducting-like coherence of the photo-excited state. Therefore, it confirms the highly unconventional nature of this photo-induced superconducting-like phase. This groundbreaking result paves the way for experiments to probe the ultrafast magnetic properties of other photo-excited superconductors.

Additionally, we measure the ultrafast magnetic dynamics ensuing upon disruption of equilibrium superconductivity using light. This experiment validates our technique's capabilities and can be exploited to control and study quantum materials. We harness the rapidly varying magnetic fields associated with ultrafast disruption of superconductivity to probe the transport properties of solids and control magnetic order in magnetic materials. The magnetic field steps we can generate have millitesla amplitude, picosecond rise times, and slew rates approaching 1 GT/s. They enable the study of "persistent currents" in transient superconductors. Moreover, these ultrafast magnetic transients pave the way for efficient magnetization switching. With the unique features of our magnetic steps, we demonstrate the possibility of switching the magnetization of a magnetic material with a coercive magnetic field of a millitesla or less.

Finally, a vast class of problems requires measuring magnetic fields varying in space with ultrafast temporal resolution. At the end of this work, we propose some scientific questions that could be answered with ultrafast optical magnetometry.

Zusammenfassung

Die Feinabstimmung von Materialeigenschaften zur Schaffung neuer Funktionalitäten gehört zu den zentralen Antriebskräften unserer technologischen Fortschritte. In diesem Kontext sind Quantenmaterialien hervorragende Kandidaten, da sie sich durch zahlreiche koexistierende und konkurrierende Phasen auszeichnen. Eine herausragende Eigenschaft dieser Materialien ist ihre hohe Empfindlichkeit gegenüber äußeren Einflüssen, die unterschiedliche Phasen mit vielfältigen Eigenschaften und technologisch relevanten Funktionalitäten hervorrufen können. Eine entscheidende Aufgabe der Festkörperphysik besteht darin, diese neuen Materiephasen zu verstehen und ihren möglichen technologischen Nutzen zu erforschen. Die Supraleitung ist ein beeindruckendes Beispiel dafür: Sie ist eine Manifestation der Quantenphysik auf makroskopischer Ebene und ermöglicht einen verlustfreien Stromfluss, der unser tägliches Leben revolutionieren könnte. Die breite Anwendung der Supraleitung wird jedoch durch die niedrigen Temperaturen, bei denen dieses Phänomen auftritt, erschwert. Daher ist die Entwicklung von Materialien mit immer höheren supraleitenden Temperaturen gegenwärtig eine bedeutende Herausforderung—in der Hoffnung, eines Tages einen Supraleiter zu erschaffen, der bei Raumtemperatur funktioniert.

Ein alternativer Ansatz ist die Nutzung von Licht, um neue und manchmal verborgene Phasen in Quantenmaterialien zu induzieren. Fortschritte in der Laserphysik ermöglichen es uns, intensive Lichtimpulse zu erzeugen, die selektiv an kollektive Moden im Material koppeln, welche für die Änderung der Materialeigenschaften verantwortlich sind. Zum Beispiel ist die kohärente Anregung spezifischer Phonon-Moden mittels Fern- und Mittelinfrarot-Laserimpulsen eine effektive Möglichkeit, die strukturellen oder elektronischen Eigenschaften des Materials zu verändern, wodurch extreme, transiente Zustände erreicht werden, die in einem Gleichgewichtszustand nicht repliziert werden können.

Richtungsweisende Experimente an der Schnittstelle zwischen Laserphysik und Festkörperphysik nutzten fortschrittliche optische Quellen, um die lichtinduzierte Steuerung von Ferroelektrizität, Magnetismus, Topologie und Supraleitung zu demonstrieren. Diese Arbeit konzentriert sich auf die Steuerung der Supraleitung mit ultraschnellen mittelinfraroten Lichtimpulsen. Es wurde bereits gezeigt, dass diese intensiven Impulse in verschiedenen Materialklassen transienten, verlustfreien Transport erzeugen können. Unterdotierte Cuprate, die mit Licht angeregt werden, das mit bestimmten Phonon-Moden resoniert, zeigen supraleiterähnliche Eigenschaften in ihren Leitfähigkeitsspektren bei THz-Frequenzen. Diese Arbeit zielt darauf ab, zusätzliche Informationen über die magnetischen Dynamiken dieser transienten Zustände zu liefern. Inspiriert von der Ähnlichkeit zwischen ihrer transienten Leitfähigkeit und den Transporteigenschaften von Gleichgewichts-Supraleitern fragen wir: Werden

diese foto-exzitierten Phasen eine transiente Meißner-ähnliche magnetische Feldverdrängung zeigen, analog zu ihrem Gleichgewichtszustand?

Um diese Frage zu beantworten, haben wir eine ultraschnelle optische Magnetometrietechnik entwickelt, die magnetische Felder mit einer Genauigkeit unterhalb eines Mikrotesla und einer Zeitauflösung im Sub-Pikosekundenbereich messen kann. Diese experimentelle Methode baut auf früheren optischen Techniken zur Messung der Magnetisierung von Supraleitern auf und erweitert diese in den ultraschnellen Bereich. Die *ultraschnelle optische Magnetometrie* ist ein nicht-invasiver Ansatz, der auf einem empfindlichen magneto-optischen Detektor basiert, der in engem Kontakt mit dem fotoangeregten Bereich platziert ist und als Wandler des lokalen Magnetfeldes im Detektorvolumen in eine präzise messbare Polarisationsrotation fungiert. Unsere Messergebnisse an einer unterdotierten $YBa_2Cu_3O_{6.48}$-Volumenprobe zeigen eine magnetische Anomalie, die mit einer transienten diamagnetischen Suszeptibilität von bis zu 30% kompatibel ist. Dieses Ergebnis kann nicht dadurch erklärt werden, indem man einfach eine erhöhte Leitfähigkeit nach der mittelinfraroten Anregung unterstellt, sondern erfordert eine gewisse supraleitende Kohärenz des photoangeregten Zustands. Daher bestätigt es den hochgradig unkonventionellen Charakter dieses fotoinduzierten supraleiterähnlichen Zustands. Dieses bahnbrechende Ergebnis ebnet den Weg für eine Reihe von Experimenten, die darauf abzielen, die ultraschnellen magnetischen Eigenschaften anderer fotoangeregter Supraleiter zu untersuchen.

Zusätzlich messen wir die ultraschnellen magnetischen Dynamiken, die nach der lichtinduzierten Störung der Gleichgewichts-Supraleitung entstehen. Dieses Experiment bestätigt die Fähigkeiten unserer Technik und kann zur Kontrolle und Erforschung von Quantenmaterialien genutzt werden. Wir nutzen die sich schnell verändernden magnetischen Felder, die mit der ultraschnellen Störung der Supraleitung einhergehen, um Transporteigenschaften von Festkörpern zu untersuchen und die magnetische Ordnung in magnetischen Materialien zu kontrollieren. Die magnetischen Feldsprünge, die wir erzeugen können, haben eine Amplitude im Millitesla-Bereich, Anstiegszeiten im Pikosekundenbereich und Anstiegsraten von bis zu 1 GT/s. Sie ermöglichen die Untersuchung von persistierenden Strömen in transienten Supraleitern. Darüber hinaus ebnet diese ultraschnelle magnetische Dynamik den Weg zu einer effizienten Magnetisierungsumschaltung. Mit den einzigartigen Eigenschaften unserer magnetischen Feldsprünge demonstrieren wir die Möglichkeit, die Magnetisierung eines magnetischen Materials mit einem koerzitivem Magnetfeld von einem Millitesla oder weniger umzuschalten.

Schließlich erfordert eine große Klasse von Problemen die Messung magnetischer Felder, die räumlich mit ultraschneller zeitlicher Auflösung variieren. Am Ende dieser Arbeit stellen wir einige wissenschaftliche Fragen vor, die mit ultraschneller optischer Magnetometrie beantwortet werden könnten.

Contents

List of Figures

Chapter 1

Introduction

In certain superconductors, coherent excitation of low-frequency collective modes using intense laser pulses can induce transient features of superconductivity at temperatures much higher than the equilibrium superconductive critical temperature (T_c). This effect has been demonstrated in cuprates [1, 2, 3], in organic superconductors [4, 5] and in iron-based superconductors[1] [6]. These experiments reported transient superconducting properties by measuring the pump-induced changes in the optical conductivity of the samples after photo-excitation. Indeed, the terahertz reflectivity of the photoexcited state resembles, transiently, the reflectivity of the equilibrium superconductor cooled below T_c.

These remarkable experiments demonstrated how light can manipulate material properties and promote particular phases in a setting beyond thermodynamic equilibrium. In the specific case considered here, light can be used to establish a dynamical state whose optical properties resemble those of an equilibrium superconductor. The scope of the work presented in this thesis is to find new observables other than optical conductivity to further characterize this transient superconducting-like state and test up to which point its properties match those of an equilibrium superconductor.

In equilibrium, the two major phenomenological cornerstones of superconductivity are dissipationless transport and the Meissner effect [7]. Terahertz spectroscopy used in the experiments cited above indicates that dissipationless transport takes place in the photoexcited state. The natural question at this point is, does this transient state also show a magnetic field expulsion analogous to the equilibrium Meissner effect? That is one of the questions we answer with the work presented here (see the results and discussion in Chapter 6).

The second aspect we focus on is extending the measurement of the conductivity of the photoexcited state to lower frequencies. Indeed, superconductivity, defined by the Meissner effect and by a vanishing resistance below T_c, is a phenomenon characterized at DC. It is, therefore, essential to explore the conductivity of the photo-excited state down to the lowest possible frequency. In principle, the lowest frequency accessible in the photo-induced state is the inverse of its lifetime [8]. One possible approach would be to electrically contact the sample and directly measure the resistivity in the photoexcited state. This approach, while apparently being the most straightforward

---

[1] Although in this last case the enhancement of superconductivity has been enhanced below T_c

way of measuring the resistance of the sample, becomes difficult at the short time scales associated with the lifetime of the photo-excited state. Even in K_3C_{60}, where the transient state becomes metastable with lifetimes up to tens of nanoseconds, these kinds of measurements are challenging [8]. In underdoped $YBa_2Cu_3O_{7-\delta}$ samples, the lifetime of the superconducting-like state is limited to the duration of the pump pulse [9] and such an approach is entirely unfeasible. To circumvent these problems in measuring transport properties of transient states directly, we develop an alternative method that exploits inductive coupling to measure persistent currents in transient superconductors by generating ultrafast magnetic field steps (see Chapter 7). Another possible approach to measure high frequency transport, is the one pursued by E. Wang et al. [10] and J. Adelinia et al. [11] who make use of Auston switches to generate and measure sub-picosecond current pulses to study light-induced superconductivity in K_3C_{60} thin films. Unfortunately, this method cannot be applied to underdoped $YBa_2Cu_3O_{7-\delta}$ samples. So far, it is not possible to grow thin $YBa_2Cu_3O_{7-\delta}$ films exposing the c-axis, along which the polarization of the mid-infrared (MIR) pump needs to be oriented to induce coherent superconducting tunneling (see for instance [12]).

Another reason it is crucial to find probes beyond optical conductivity is the intrinsic uncertainties associated with using this technique to characterize the photo-excited state. For instance, as pointed out by S. Dodge et al. [13], it is arguable which model is best suited to reconstruct the optical properties of the excited state at high pump intensities and given the considerable pump-probe penetration depth mismatch. The choice of the model would quantitatively impact the enhancement of the conductivity induced by the optical pump and blur the evidence pointing at dissipationless transport in favor of a mere enhancement of the conductivity induced by the pump. Finding that the photoexcited sample expels static magnetic fields would be an indication that this phase is qualitatively different from a metallic state which is not expected to react at all to the presence of a static field. This work concentrates on light-induced superconductivity in a specific sample: $YBa_2Cu_3O_{6.48}$. We decided on this specific doping because the samples with this composition showed the most significant light-induced conductivity enhancement, as measured with THz spectroscopy. Moreover, this effect has been shown to persist up to the highest temperatures in this compound, all the way to 400 K, roughly matching the pseudogap temperature [3].

We continue this chapter by briefly summarizing the results of previous optical conductivity measurements demonstrating superconducting-like transport. We then describe the idea of the experiment we want to execute to ascertain the presence of a Meissner-like magnetic field expulsion after photo-excitation. Finally, we describe the general idea behind using ultrafast magnetic field steps to probe “persistent” currents in a transient superconductor. We close with a brief outline showing how the rest of the thesis is structured.

1.1 Optical conductivity of $YBa_2Cu_3O_{7-\delta}$

Time domain terahertz (THz) spectroscopy is a suitable experimental technique to probe superconductors [14, 15]. It allows for the measurement of conductivity in the frequency range of the superconducting gap (i.e., the pairing energy of Cooper pairs), a superconductivity hallmark. The basic idea is to illuminate the sample with an ultrafast THz pulse and measure the amplitude and phase of the wave reflected from the surface of the material [16]. By comparing the amplitude and phase of the reflected and incoming THz pulses, we can extract the frequency-dependent real and imaginary part of the conductivity of the sample in the spectral range of the THz probe.

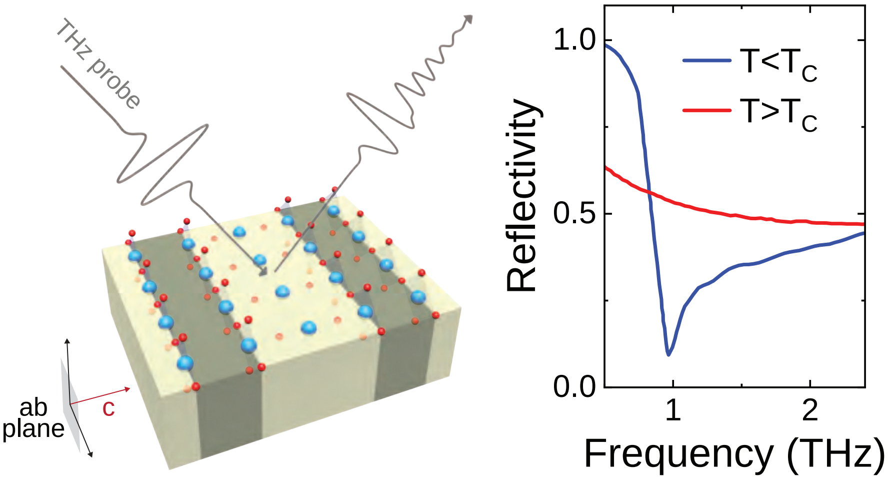

FIGURE 1.1: Experimental geometry and equilibrium terahertz reflectivity of $YBa_2Cu_3O_{6.5}$ along the c-axis. Data reproduced from [12].

The left panel of Figure 1.1 shows the geometry of a THz reflectivity experiment on a $YBa_2Cu_3O_{6.5}$ sample exposing a surface containing the c-axis. The electric field of the THz pulse is polarized along the c-axis to probe the conductivity of the cuprate sample in this direction across the copper oxide planes. The right panel of this figure displays the absolute value of the c-axis polarized THz reflectivity of the sample in the frequency range of the THz probe. By comparing the data measured at 100 K (in red) above T_c ($\sim$55 K) and below T_c at 10 K (in blue), we see a sharp feature developing in the reflectivity spectrum around 1 THz. This feature indicates superconductivity appearing along the c-axis after cooling below T_c. Figure 1.3 displays the real (σ_1) and imaginary (σ_2) parts of the optical conductivity along the c-axis above and below T_c at equilibrium (solid red and blue lines respectively). After cooling across T_c, we see both σ_1 and σ_2 changing strikingly. σ_1, associated with the dissipative properties of the sample, becomes zero while σ_2 develops a $\sim 1/\omega$ divergence at low frequency. This second spectral feature can be understood as a result of the kinetic inductance characterizing the scattering-free transport of Cooper pairs captured by a simple Drude model (see, for instance, Chapter 2 of Reference [7]).

This technique is helpful to measure equilibrium states and can be successfully employed to measure ultrafast transients. For instance, these ultrafast THz pulses can probe the temporal evolution of the conductivity of a sample upon photo-excitation. This idea is behind the pump-probe experiments hinting at transient superconducting-like transport after mid-infrared photo-excitation in $YBa_2Cu_3O_{7-\delta}$.

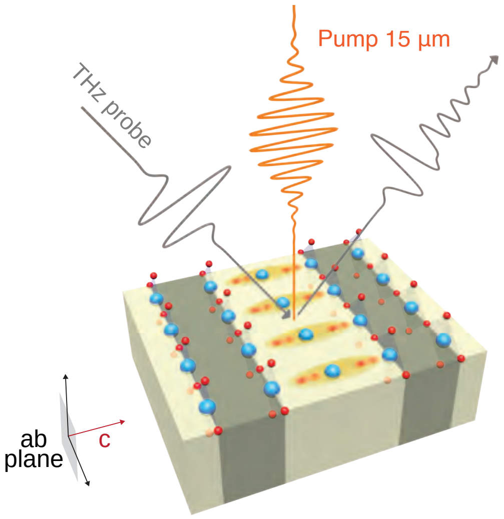

FIGURE 1.2: Geometry of a MIR pump THZ probe experiment. Adapted from [17].

Figure 1.2 shows the experimental geometry of these experiments: a pump pulse polarized along the c-axis excites specific phonon modes in the sample [12]. A THz probe pulse monitors the conductivity change ensuing upon photoexcitation.

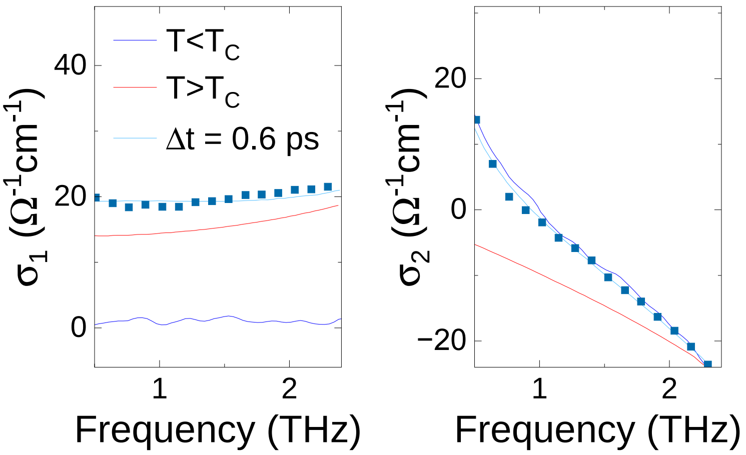

FIGURE 1.3: Measured real and imaginary part of the THz conductivity of $YBa_2Cu_3O_{7-\delta}$ at equilibrium above and below T_c and the peak of the photo-excited response (datapoints) above T_c. The light blue solid line is a fit for the photo-excited response. Adapted from [12].

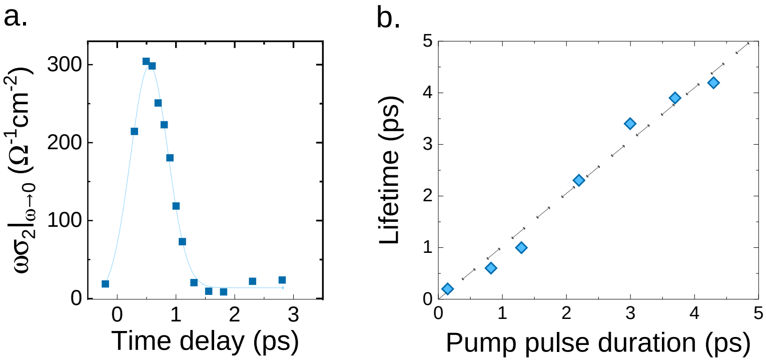

FIGURE 1.4: **a)** Time evolution of the light-induced superfluid density extracted from the imaginary part of the optical conductivity as described in the Main Text. Adapted from [12]. **b)** Lifetime of the driven state versus pump pulse duration. Adapted from [9].

In figure 1.3 also the terahertz conductivity spectra measured above T_c, at the peak of the pump probe response (Δt ∼ 0.6 ps) are reproduced (light blu datapoints, from reference [12]). A natural approach is to compare the photoexcited response to the equilibrium spectra to gain information about this driven state. In the photo-excited state, σ_2 exhibits the distinctive $\sim 1/\omega$ divergence observed at equilibrium after cooling while σ_1 increases slightly, indicating an increased dissipative character. On one hand, the first observation suggests that superconducting transport properties appear induced by the pump; on the other, the fact that dissipation increases implies an absorption of the pump energy leading to enhanced dissipation. Indeed, further experiments helped clarify this apparent contradiction: as stated in reference [9], the pump has a two-fold effect that can be captured by a model involving two conducting fluids. A superconducting fluid is created responsible for the divergence at low frequencies in σ_2. At the same time, the pump also heats the quasiparticles present in the sample, increasing its dissipative response, which conceals the dissipation-less properties of the photo-induced superconducting fluid.

Another essential characteristic of this transient state already studied by THz spectroscopy, which will become important in Chapter 6, is its lifetime. The left panel of Figure 1.4 shows the temporal evolution of the photo-induced superfluid density when the pump pulse has a duration of 600 fs. Assuming a simple Drude model to fit the conductivity of the excited state, this quantity is proportional to $\lim_{\omega\to 0}\omega\sigma_2(\omega)$. The pump produces a sizeable transient superfluid density above T_c for ∼1 ps. Within the experimental accuracy, this time scale is compatible with a lifetime of the photo-excited state equal to the pump pulse duration used for excitation. A later experiment demonstrated that the lifetime of the light-induced superconductor is equal to the duration of the pump pulse [9]. This result reproduced in the right panel of Figure 1.4, importantly implies that no metastable state exceeding the duration of the pump pulse is reachable within the accessible experimental parameters [2]. Suppose that the lifetime measured by THz spectroscopy indicates the presence of a superconducting-like state characterized by a sort of Meissner-like magnetic field expulsion. Then, another relevant consequence of this experiment for this thesis is the fact that we expect a magnetic response from the material (if any) with a duration compatible with the time scales shown in Figure 1.4. This finding forces us to find a technique that allows us to measure changes in the magnetic field at ultrafast time scales. As described in chapter 3, we opted for an optical detection technique based on the Faraday effect, which satisfies the requirements above.

1.2 Magnetic field expulsion in driven $YBa_2Cu_3O_{6.48}$

As discussed in the previous paragraphs, the probing mechanisms used so far to study photo-induced superconductivity only give access to the conductivity of the transient state. Probing its magnetic properties is a task of paramount importance to ascertain its superconducting nature. The question we want to answer is, therefore, the following: will optically-driven $YBa_2Cu_3O_{6.48}$ expel an externally applied static magnetic field from its volume similarly to an equilibrium superconductor when cooled below T_c? The requirements we have for such an experiment are many: we need a stable external magnetic bias being constant for the lifetime of the photo-excited state, we need access to a sample surface exposing the a-c crystallographic axes, for optical excitation, and we need a noninvasive technique to probe small ultrafast changes of the magnetic field in a wide temperature range.

While we discuss the technical details in Chapter 3, we already anticipate that we opted for ultrafast optical magnetometry as a probing technique. Practically, this means that we place a material with a high Verdet constant adjacent to the sample, and we propagate linearly polarized, ultrafast, probe pulses through it. We then measure the rotation of the polarization of the light emerging from the detector. This rotation is proportional, via the Faraday effect, to the value of the local magnetic field in the magneto-optic material. The measurements reported in Chapter 4 and 5 confirm that this technique has the required spatial and temporal sensitivity to measure a magnetic field expulsion from a photo-excited superconductor. Figure 1.5 shows a schematic representation of the geometry of the experiment that satisfies the requirements pointed out above and discussed in more detail in Chapter 6.

As a last introductory comment, we briefly discuss the constraints the biasing magnetic field must follow. As pointed out in Chapter 2, a superconductor expels a static magnetic field from its volume. That entails a competition between magnetic fields and the superconducting order, since an applied magnetic field higher than a critical value, called H_c, disrupts completely superconductivity in a type I superconductor. Superconductivity in type II superconductors, like the cuprates, is

---

[2] That is not the case, for instance, in K_3C_{60}, as Budden et al. demonstrated that a long-lived metastable state was established for sufficiently high pump fluence [8].

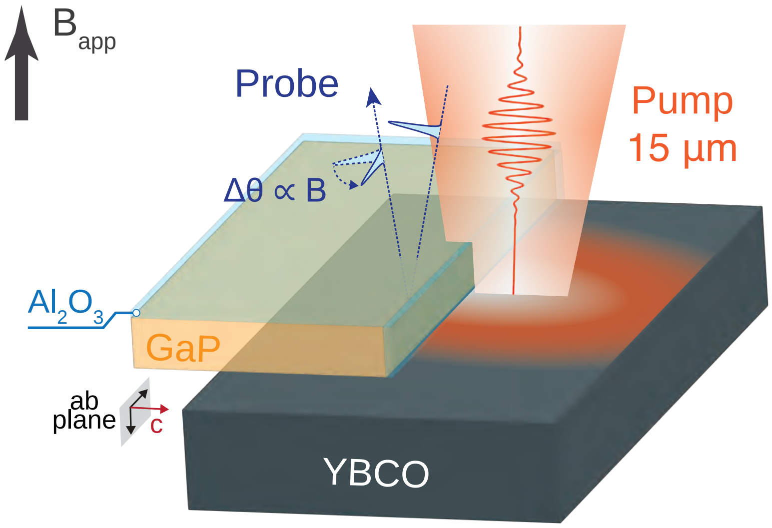

FIGURE 1.5: Experimental geometry to measure a magnetic field expulsion. The magnetic field changes induced by the photo-excited region of $YBa_2Cu_3O_{6.48}$ are measured with optical magnetometry in an adjacent magneto-optic detector (GaP) with an 800 nm probe. The magneto-optic crystal is protected from the high-intensity MIR pump by placing two thin sapphire layers above and to the side of it, respectively. Adapted from [17].

more robust against magnetic fields: there are two critical fields, a first critical field (H_{c1}) below which the sample is perfectly diamagnetic and above which the external magnetic field can penetrate the sample volume without completely disrupting the superconducting order. That is the case up to the point at which a second critical field (H_{c2}) is reached, and the superconducting order vanishes [7]. Our understanding of the physics of the photo-excited state is too little to expect it to have a specific magnetic behavior. A reasonable hypothesis we can make is to assume its properties to be similar to the equilibrium properties of our $YBa_2Cu_3O_{6.48}$ sample, which has a first critical field of ∼2 mT in the a-c plane (see data reported in Chapter 2). In our experiment, we apply a biasing external magnetic field that can be varied in the range of a few milli Tesla to avoid levels that could interfere with the light-induced state. Finally, Chapter 6 presents the results of the experiment described here. These results confirm that the photo-excited state in $YBa_2Cu_3O_{6.48}$ expels the static applied magnetic field. This magnetic response is, importantly, not compatible with a bare increase of metallicity following photo-excitation but hints that the nature of the light-induced state is crucially connected with an out-of-equilibrium superconducting order.

1.3 Probing persistent currents in photo-excited superconductors

Another consequence of superconductors' perfect conductivity is that they can sustain a DC supercurrent for infinitely long once it is launched in the material (see for instance [18]). That is mathematically indicated by the $1/\omega$ divergence of the imaginary part of the conductivity at low frequencies and by the pole in σ_1 at zero frequency (see Chapter 2). In principle, dissipationless transport and magnetic field expulsion, which characterize superconductivity, are defined as DC properties of the material. These low-frequency conductivity features are intrinsically unavailable for a transient superconductor due to their finite lifetime. The lowest frequency measurable is limited to the inverse lifetime of the photo-excited state (see Figure 1.6). Therefore, on one side, it is crucial to increase the lifetime of the photo-excited state; on the other, new probing mechanisms are needed that can access this low-frequency region while maintaining a sizable sensitivity in the typical frequency range of the superconducting gap. Regarding the first point, our group has already pursued extending the transient state's lifetime. For instance, spectacular results have been achieved in K_3C_{60}, another sample showing superconducting-like transport properties upon photo-excitation [8]. In underdoped $YBa_2Cu_3O_{7-\delta}$ the transient superconducting-like state lives as long as the pump pulse illuminates the sample [9]. That can be as long as 5 ps, limited by thermal damage in the sample (see Figure 1.4).

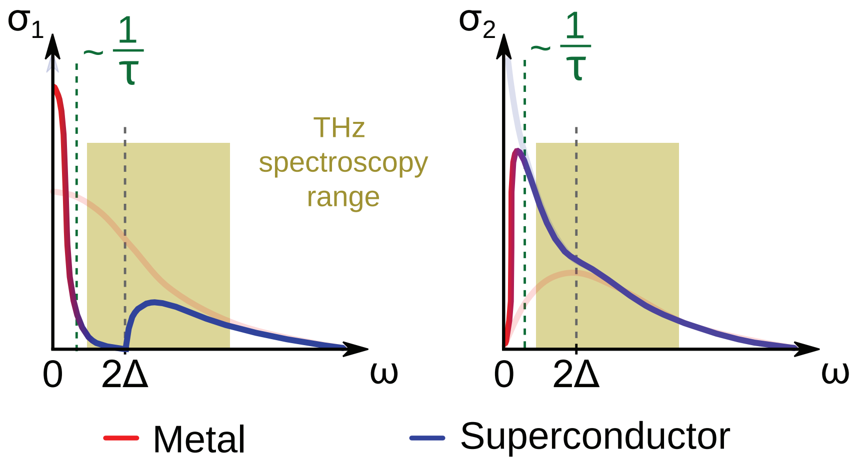

FIGURE 1.6: Complex optical conductivity of a transient superconductor with lifetime τ. Superconducting contributions to the graph are displayed in blue, while metallic ones are shown in red. For frequencies smaller than the inverse of the lifetime of the superconducting transient state, the optical properties show a metallic behavior. Thus, for low frequencies in $\sigma(\omega)$, a narrow Drude peak is formed out of the gapped state, and the divergence in $\sigma(\omega)$ converges to zero. THz spectroscopy cannot access the relation to a metallic state, lacking spectral weight at low enough frequencies. Adapted from [19]

As for the second requirement, a possibility is to apply a magnetic transient spanning a wide frequency range to induce eddy currents in the sample and then to measure the magnetic field they produce to understand their properties, especially the decay time, which would indicate the lowest frequency at which the sample effectively possess perfect conductivity. The transport currents should ideally be induced on time scales that are much faster than the lifetime of the photo-excited state to measure cleanly the free decay of the "persistent" currents (see Chapter 2, Section 2.8). As described above, a magnetic field step with a sufficiently fast-rising edge is a suitable device to launch superconducting currents. To better illustrate, with magnetic step, we mean a magnetic pulse with a short rise time and a very long decay time, ideally several orders of magnitudes longer than the rise time. The idea is based on the Faraday-Lenz law, describing how magnetically induced currents build up in conductors to shield a time-varying magnetic field. While both a metal and a superconductor would react to such a magnetic field step, the qualitative difference between the two is that the shielding of the magnetic field lasts for infinitely long times in the superconductor (or for the whole lifetime of the state for a transient superconductor). At the same time, it dies out on time scales due to its inductance and resistance in the metal. This difference can be traced back to the fact that electron transport in metals is damped while Cooper pairs move without scattering.

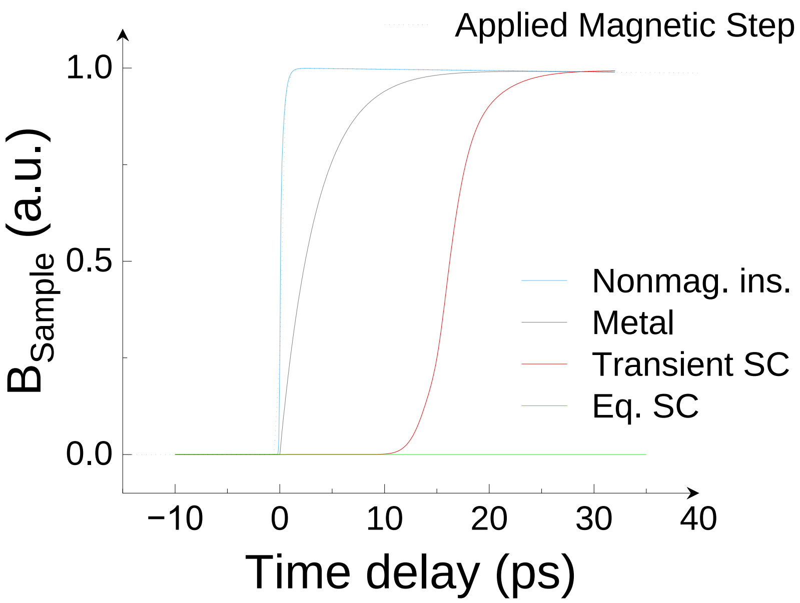

FIGURE 1.7: Schematic illustration of the magnetic response of different samples to an ultrafast magnetic field step. The higher its conductivity, the higher the magnetic shielding response of the sample. The extreme cases are a nonmagnetic insulator (light blue line), which does not modify the applied field, and an equilibrium perfect superconductor (green line), which shields completely the applied field.

These considerations are schematically summarized in Figure 1.7. Concerning speed requirements, if we want to apply this technique to study transient states, we need to ensure that the rise time and decay time of the magnetic field step are respectively shorter and much longer than the state's lifetime. Ideally, the rise time should be as fast as ∼1 ps to connect with the lowest frequencies part of previous THz conductivity measurements (see Figure 1.3). These requirements ensure that this probing technique has sufficient spectral weight to cover the range going from the inverse of the lifetime of the photo-excited state at low frequencies up to ∼0.5 THz.

The technique we have developed is a novel approach to studying the conductivity and magnetic properties of photo-excited states. It is based on the magnetic transient created when the equilibrium superconducting state in a thin superconductor is disrupted with an ultrafast optical laser pulse, as discussed in Chapter chapter:disruption. Building on this observation, we have designed and tested a device on a magnetic sample, as detailed in Chapter chapter:steps. Our results demonstrate the exciting potential of this novel technique to study the conductivity and the magnetic properties of equilibrium and transient states in a frequency range spanning several octaves from DC all the way to sub-THz frequencies.

1.4 Thesis outline

Chapter 2 outlines the equilibrium magnetic properties of superconductors and elaborates in greater depth their implications on the choices we made in designing the experiments.

Chapter 3 introduces and discusses the technique we chose to measure magnetic fields ranging from DC to ultrafast time scales.

Chapter 4 shows some experimental data collected measuring equilibrium superconductors in our experimental geometry. We also discuss the conclusions on the equilibrium properties of the material we can draw from these data with the guidance of phenomenological simulations. These results will be helpful in Chapter 6 to interpret quantitatively the magnetic field expulsion measured above T_c.

Chapter 5 describes the ultrafast magnetic dynamics we measure in a thin film of optimally doped $YBa_2Cu_3O_7$ after disrupting superconductivity below T_c with an optical pump pulse. This experiment validates our experimental technique and demonstrates that we can measure tiny magnetic field changes with ultrafast temporal resolution.

Chapter 6 shows, after discussing the technical detail of the experiment, the magnetic field expulsion measured in $YBa_2Cu_3O_{6.48}$ after photo-excitation and how the signals change upon changing the most relevant experimental parameters.

Chapter 7 presents the device we built and how to generate ultrafast magnetic steps to measure persistent currents in transient superconductors. In this chapter, we also show a test measurement on a ferrimagnetic sample that shows coherent magnetization oscillations triggered by the magnetic step.

Chapter 8 closes the thesis with some final remarks and proposes possible further experiments that could fruitfully employ the ultrafast magnetometry technique developed.

Chapter 2

Magnetic properties of equilibrium superconductivity

Superconductivity, discovered in 1911 by H. Kamerlingh Onnes [20], is an intriguing manifestation of quantum physics and has an enormous potential for applications. This phenomenon's most striking macroscopic manifestations are vanishing resistance and expulsion of static magnetic field. The first characteristic is especially interesting for applications as it can be exploited to transport energy without losses. This goal still needs to be realized owing to the extremely low temperatures required for superconductivity to set in. That is another reason light-induced superconductivity is a topic of great interest, as it represents a possible way to achieve a room-temperature superconductor. The focus of this chapter will be an operative description of the main magnetic properties of superconductors. The notions introduced here will be used to justify experimental choices and to interpret the results presented in later chapters. What we want to anticipate already now is the fact that only in specific cases is a complete expulsion of the magnetic field from the volume of the sample achieved. As discussed below, the intermediate state of a type I superconductor and the mixed state of a type II superconductor are examples of states in which superconductivity is retained even if the magnetic field penetrates some regions of the sample. This experimental observation contradicts the phenomenological definition of superconductivity given above. A more precise definition of superconducting state is given by Tinkham [7] and is based on "the existence of the many-particle condensate wavefunction $\psi(r)$, which has amplitude and phase and which maintains phase coherence over macroscopic distances.".

2.1 Field cooled and zero-field cooled magnetic properties

At equilibrium, superconductivity appears when cooling the material below a specific temperature T_c, which is material-dependent. Once in the superconducting state, the material acquires two new properties: vanishing resistance and the capability to expel static magnetic fields. This second feature is also known as the Meissner effect [21]. A simple way to visualize the magnetic response of a superconductor due to these two properties is to imagine two experiments summarized in Figure 2.1, which we call “field cooling” and “zero-field cooling”, respectively. The first experiment involves applying a magnetic field as the sample is held at a temperature T>T_c and then cooling the sample below T_c. As the superconducting transition occurs, the sample *expels* from its volume the externally applied magnetic field. The second experiment differs from the first because the order of the two operations is swapped: first, the sample is cooled below T_c, and then an external magnetic field is applied. In this case, the magnetic field is *excluded* from the sample volume. In an ideal case (defect-free superconductor with perfect diamagnetism), the results of these two experiments are the same, even if their implications are profoundly different. The expulsion of a static magnetic field is a unique property of a superconductor, not captured by classical arguments but postulating a “rigidity” of the superconducting wavefunction [7]. A perfect metal, characterized only by zero resistance, would not react to a static magnetic field. Conversely, both a perfect metal and a superconductor would exclude an externally applied magnetic field. This result is a consequence of the sample’s perfect conductivity, which implies an infinitely long scattering time. For an infinitely long scattering time, any time-varying magnetic field, no matter how slow, induces currents that completely shield the applied field, as Faraday law prescribes.

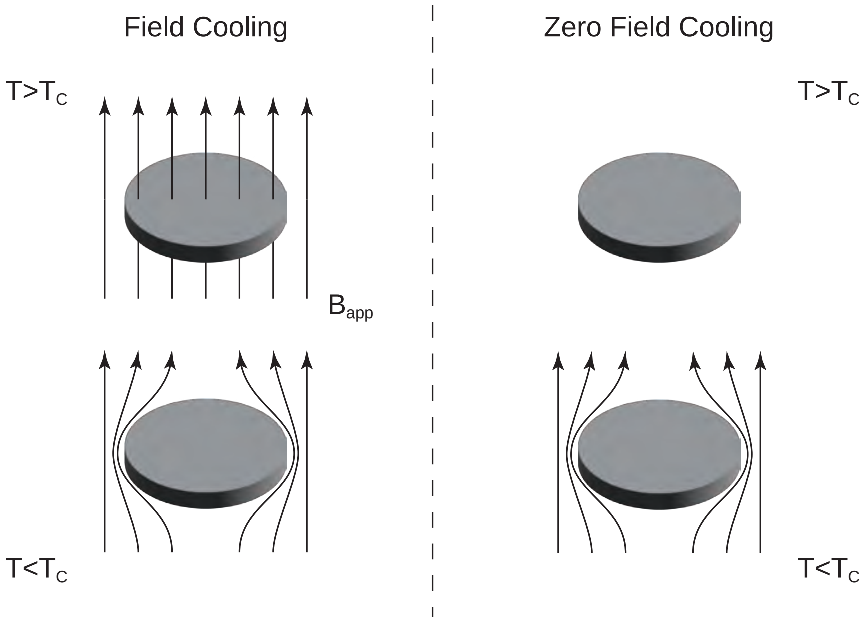

Figure 2.1: Field cooled and zero-field cooled magnetic properties of an ideal superconductor

2.2 The role of defects

The previous discussion highlights how the Meissner effect is a unique marker of superconductivity. Therefore, assessing the presence of this effect in a light-induced superconductor is essential to qualify how close this novel state of matter is to its equilibrium counterpart and the motivation for the experiment described in Chapter

6. This measurement is very informative but at a price: measuring magnetic field expulsion in an actual sample is much more complex than measuring its magnetic field shielding (equivalent to measuring its conductivity). The leading cause is defects that strongly modify the sample's magnetic response. As a simplified approach, we model the defects in our sample or its regions that are not superconducting as holes. Suppose we focus on the effect of a single hole, as depicted in Figure 2.2. In that case, we see that the deviation of the magnetic field lines of the uniform external magnetic field applied (B_{app} in the figure) is strongly reduced in the Meissner or field-cooled state compared to the case of a defect-free superconductor. The superconductor still expels the field from its volume, pushing it into the hole in its center.

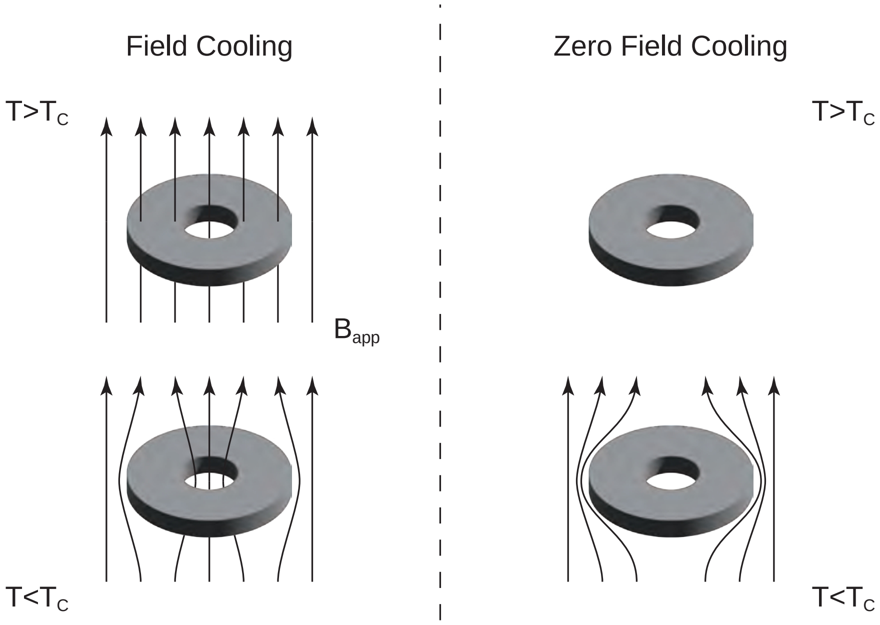

FIGURE 2.2: Field cooled and zero-field cooled magnetic properties of a superconductor with a defect

Conversely, the sample's magnetization is similar to its defect-free counterpart in the zero-field cooled case, and the magnetic field is still excluded from the central hole. That is true for every defect as long as a connected path around the defect exists along which the shielding currents can flow. An additional source of difficulty connected to measuring the magnetic properties of the photo-excited state is connected to its small thickness compared to its later dimensions. We will delve into this issue in more detail in the next section.

2.3 Notes on the electrodynamics of superconductors

Before we discuss the impact of the geometry of the (light-induced) superconductor on its magnetic response, a minimal review of their electrodynamics is required. Here, we follow closely the treatment given in Chapters 1 and 2 of reference [7]. Vanishing resistance and the Meissner effect are well described by the two London equations:

$$\mathbf{E} = \partial_t(\Lambda \mathbf{j}_s) \tag{2.1}$$

$$\mathbf{h} = -c\nabla \times (\Lambda \mathbf{j}_s) \tag{2.2}$$

with:

$$\Lambda = \frac{4\pi\lambda^2}{c} = \frac{m}{n_s e^2} \tag{2.3}$$

n_s represents the number of superconducting carriers, m is their mass, and e is the electronic charge. In the second equation, $\mathbf{h}$ indicates the local magnetic field generated by the superconducting currents. From this equation combined with Ampere's law, we extract an equation describing the screening of static magnetic fields inside the volume of the superconductor (i.e., the Meissner effect):

$$\nabla^2 \mathbf{h} = \frac{\mathbf{h}}{\lambda^2} \tag{2.4}$$

The solution of this equation implies that the magnetic field decays with a penetration depth of λ from the surface of the superconductor. As shown in Equation 2.3, λ^2 is anti-proportional to the number of superconducting carriers. It diverges approaching T_c, where the number of superconducting carriers goes to zero, recovering the penetration of the magnetic field in the normal state. λ is a phenomenological parameter depending on the superfluid density n_s. An upper limit for λ is the London penetration depth:

$$\lambda_L = \left(\frac{mc^2}{4\pi n e^2}\right)^{1/2} \tag{2.5}$$

λ_L is achieved from the phenomenological definition of λ above, assuming all the normal carriers, with density n, condense into Cooper pairs.

These are two phenomenological equations that are not justified by a comprehensive theory. A simple but incorrect derivation can be extracted by modeling the superconductor with a simple Drude model: $d\mathbf{p}/dt = \mathbf{p}/\tau + e\mathbf{E}$. The scatter-free transport of Cooper pairs is modeled here by taking the limit of τ going to infinity, so the equation reduces to $d\mathbf{p}_s/dt = e\mathbf{E}$. If we assume $\mathbf{p}_s = m\mathbf{v}_s$ and $\mathbf{j}_s = n_s e\mathbf{v}_s$, the first London equation follows directly, and the second can be achieved by taking the curl of both sides of the equation and using Faraday law.

This line of thought, although intuitive, is not in general applicable. The reason is that this simple model does not capture the *non-local* character of the dynamics of charged carriers. The current in a particular position results from the electromagnetic field in a finite region around that position. For normal carriers in a metal, the size of this region is equal to the mean free path. For Cooper pairs in a superconductor, the non-locality of the Cooper pair is indicated by a quantity, introduced by Pippard, called coherence length:

$$\xi = a\frac{\hbar v_F}{k_B T_c} \tag{2.6}$$

where a is constant of order unity, $\hbar$ the reduced Planck constant and k_B the Boltzmann constant. The coherence length can be much bigger than the typical length scales of spatial gradients of the electromagnetic field in the material, set by the London penetration depth, making the argument based on the Drude model unsound. Measurements of the magnetic field penetration depth in conventional superconductors reveal that the field penetrates more than twice as much of what would be expected from Equation 2.5 (i.e., typically 50 nm instead of the predicted ~20 nm), even at temperatures $T \ll T_c$, when all the normal electrons should condense into Cooper pairs. That is a result of the weakened response of the superconducting fluid to magnetic fields varying on length scales shorter than the coherence length.

Following the treatment of Tinkham [7], a more profound argument postulates that the superconducting wave function must be *rigid* in its ground state. That amounts to stating that the canonical momentum $\mathbf{p} = m\mathbf{v} + e\mathbf{A}$ equals zero. So, $\mathbf{v}_s = -\frac{e\mathbf{A}}{mc}$ and the London equations follow via $\mathbf{j}_s = n_s e \mathbf{v}_s$. This argument can be rigorously justified in the BCS theory framework and is generally plausible, arguing that the net momentum should be zero without an external magnetic or electric field. This definition of the current J_s is not gauge invariant and will be appropriate only for a specific gauge choice called the London gauge (see Chapter 1 of Tinkham [7]).

2.4 The demagnetizing factor

As discussed in the previous section, the superconductor shields or expels an external magnetic field within a distance λ from its surface. If we think about this phenomenon in terms of macroscopic average fields, the superconducting currents, considered as a whole, generate a magnetization ($\mathbf{M}$) equal in magnitude and opposite in sign to the external applied magnetic field ($\mathbf{H}_{app}$). In this way, the magnetic flux density ($\mathbf{B}$) in the superconducting region is zero, as required by the rigidity of the superconducting wavefunction (see the first panel of Figure 2.3).

That is true when the shape of the superconductor is that of a thin needle, and the external magnetic field is applied along the axis of the needle. If this is the case, the dipolar field generated by the sample's magnetization is small and does not significantly contribute to the magnetic field strength $\mathbf{H}_{app}$ that induces the sample's magnetization; it is sufficient to consider the externally applied magnetic field: $\mathbf{H} = \mathbf{H}_{app}$. This picture is not correct for general sample geometries anymore, and the magnetization of the sample is not only a linear function of $\mathbf{H}_{app}$ but also depends on the dipolar field it generates. This field called the "demagnetizing field" ($\mathbf{H}_d$, see the third panel of Figure 2.3), is anti-proportional to the magnetization, and the proportionality factor is called demagnetizing factor (N_d, a positive definite quantity): $\mathbf{H}_d = N_d \cdot \mathbf{M}$. N_d depends on the specific shape of the sample. In most cases, the value of N_d is not uniform throughout the sample volume. In the particular case of axis-symmetric ellipsoids, N_d can be expressed as a uniform, diagonal 3D tensor whose trace adds up to unity (to keep the formulation simple, we will assume in the following to deal with samples

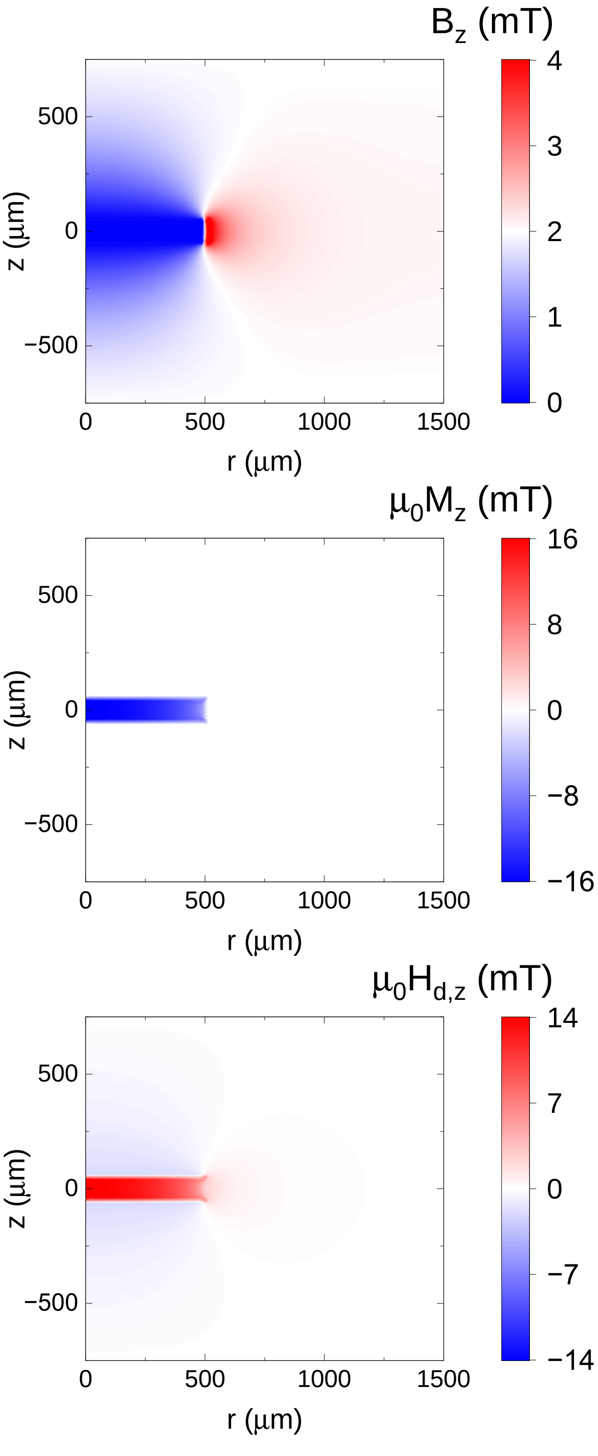

FIGURE 2.3: From the top, the panels display the simulated z-components of the magnetic flux density B_z, the magnetization M_z, and the demagnetizing field generated by the sample $H_{d,z}$, respectively. The external field applied is $\mu_0 H = 2\,\mathrm{mT}$, the sample is a disk 100 µm tick and 1 mm wide (indicated by the grey dashed line), with an associated value of $\mu_r \sim 0$, to represent the perfect diamagnetism of a superconductor. We employed COMSOL Multiphysics® as discussed in Section E.1 to perform the simulation

that are ellipsoids). For those geometrical shapes, given the axial symmetry, the two elements of the tensor associated with the directions orthogonal to the axis symmetry are equal [22]. For instance, if we consider a thin disk with a thickness much smaller than its lateral dimensions, the two components of the diagonal demagnetizing tensor orthogonal to the axis of the disk will be close to zero, while the component parallel to the axis of the disk will be close to unity. That indicates that the demagnetizing field and its associated energy cost will be negligible when the magnetization points along any of the in-plane directions, while it will be close to the value of the magnetization itself when the magnetization points along the axis of the disk.

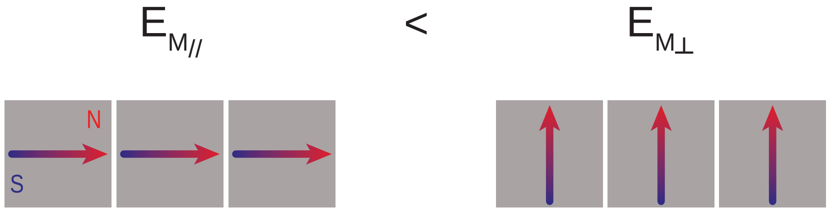

Figure 2.4: Magnetic dipoles' arrangement for the magnetization pointing in plane ($M_{\parallel}$) or out of plane ($M_{\perp}$).

Intuitively, we can understand this phenomenon by imagining building a magnetic object by bringing close to each other small magnetic dipoles initially infinitely far from each other (see Figure 2.4). As the dipoles get close, they interact: if we try to arrange them on the plane orthogonal to their magnetic moment to build a flat object magnetized out of the plane, we will have to counteract strong repulsive forces. Conversely, we all know that when we played with magnets as kids, it was easier to stack them on top of each other. In the first case, the stray dipolar magnetic field from the object extends into a large region of space and has a high magnetic energy cost associated to it (integral of $\frac{H_d^2}{2\mu_0}$). In the second configuration, resembling a magnetic rod, the overall magnetic dipole of the object is weaker since the alternating magnetic poles of the individual building dipoles compensate each other throughout most of the volume of the object, minimizing the surface of uncompensated magnetic charges at the top and bottom of the rod. The problem of the demagnetizing fields was initially studied for ferromagnets, where the magnetization is aligned with the applied field, and the demagnetizing field effectively reduces the magnetizing effect of $\mathbf{H}_{app}$. Hence, the name *demagnetizing* field and factor for $\mathbf{H}_d$ and N_d, respectively. The situation is the opposite for a superconductor that behaves like a diamagnet, and $\mathbf{H}_d$ is effectively a *magnetizing* field with the same sign as $\mathbf{H}_{app}$. Nonetheless, we will use the same convention used in literature here and call the field generated by the magnetization of the superconductor demagnetizing field and the proportionality factor between $\mathbf{H}_d$ and $\mathbf{M}$ demagnetizing factor.

Formally, the magnetic susceptibility is modified by the presence of the demagnetizing field in the following way:

$$M = \chi_i \cdot (H_{app} + H_d) \tag{2.7}$$

All the quantities in Equation 2.7 are scalars indicating the magnitude of the collinear vector vectors $\mathbf{M}$, $\mathbf{H}_{app}$, $\mathbf{H}_d$ and the component of the magnetic susceptibility tensor along the applied field. χ_i indicates the intrinsic magnetic susceptibility of the sample, measured by shaping the sample as a thin elongated rod and applying the external field along the axis of the rod. Using the definition of demagnetizing factor:

$$M = \chi_i \cdot (H_{app} - N_d \cdot M) \tag{2.8}$$

Similarly to what was stated above, N_d is the component of the demagnetizing tensor along the applied field. Rearranging the equation above, we find the apparent or effective magnetic susceptibility of the sample, which takes into account also its geometry:

$$M = \frac{\chi_i}{1 + N_d \cdot \chi_i} \cdot H_{app} = \chi_{eff} \cdot H_{app} = \chi_i \cdot H_{int} \tag{2.9}$$

With:

$$\chi_{eff} = \frac{\chi_i}{1 + N_d \cdot \chi_i} \tag{2.10}$$

$$H_{int} = \frac{H_{app}}{1 + N_d \cdot \chi_i} \tag{2.11}$$

So, the intrinsic magnetic susceptibility is renormalized to χ_{eff} by the demagnetizing factor. Alternatively we can imagine that the applied field inside the sample volume is renormalized to an effective internal field H_{int}. So, the effect of the demagnetizing factor is mitigated when the magnetic susceptibility of the sample is low, and we retain the usual proportionality between magnetization and intrinsic magnetic susceptibility regardless of the shape of the sample. This assumption holds for common diamagnets but is no longer valid for superconductors with high diamagnetic susceptibilities ranging from -0.1 to -1. When N_d and $|\chi_i|$ approach unity, the internal field and the magnetization are strongly enhanced (in theory diverging, see Figure 2.5). Due to this enhancement, the magnetic field seen by the superconductor can easily exceed the critical field and disrupt the superconducting order in type I superconductors. In Sections 2.6 and 2.7, we comment on this issue and its implications for type I and type II superconductors.

After discussing the main issues connected to the demagnetizing field, we are still left with calculating it. Although numerical simulations offer the most precise solution, we found many helpful approximated expressions in Prozorov and Kogan's paper [23]. For instance, in most of our experiments, the magnetized sample can be approximated as a thin cylinder with the magnetization aligned along its axis. The demagnetizing factor in this configuration can be estimated by the following formula: $N_d \sim \frac{1}{1+1.6/A}$, where A is the ratio between the diameter and the height of the cylinder.

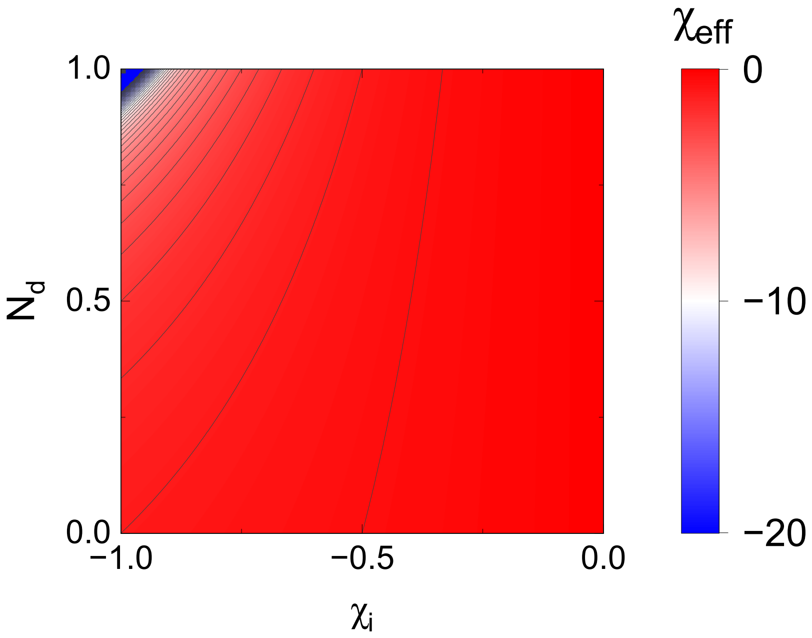

FIGURE 2.5: Effective magnetic susceptibility χ_{eff} (see Equation 2.10) versus demagnetizing factor and intrinsic magnetic susceptibility χ_i. The effective susceptibility and magnetization quickly diverge as the product $\chi_i \cdot n \rightarrow -1$. The contour lines are separated by steps of 0.5 from each other

2.5 Penetration depth in thin films

The geometry of the sample affects also the magnetic penetration depth, as seen, for instance, in thin films (see Section 3.11.4 of reference [7]). When an external magnetic field is applied *parallel* to the film plane, if the coherence length of the superconductor (ξ) is much larger than the film thickness (d), the magnetic field penetration is described by an effective value $\lambda_{eff} \approx \lambda_L \cdot (\xi/d)^{1/2}$, coinciding with the London penetration depth renormalized by the coherence length divided by the thickness of the film. Intuitively, this means that the reduced thickness of the sample hinders the screening, and the response of a *nonlocal* superconductor becomes equivalent to that of a *local* one with a mean free path approximately equal to d. Differently said, the lambda increase is equivalent to a reduction of the value of n_s defining the local constitutive relation between **A** and **J**. This reduction accounts for the new mean free path of the carriers artificially imposed by the geometrical boundary conditions.

This correction should be negligible for the measurements presented in Chapter 4. In fact, the a-b plane coherence length of optimally doped $YBa_2Cu_3O_7$ at our working temperatures (much lower than T_c) is ∼1.5 nm [24]. This value is much lower than the thickness of the films we use, ∼150 nm, so the correct penetration depth for a parallel field should be the bulk value.

The situation is different if we consider the penetration depth $\lambda_\perp$ associated with a magnetic field *perpendicular* to the film given by the following formula introduced by Pearl [25]:

$$\lambda_{\perp} = \frac{\lambda_{eff}^2}{d} \tag{2.12}$$

The magnetic field screening length ($\lambda_{\perp}$) increases by a factor λ_{eff}/d compared to the bulk value, even when λ_{eff} equals the London penetration depth. This correction reflects the effect of the two-dimensional geometry on the solution of Maxwell's equations. It does *not* imply a change in the intrinsic transport properties of the superconductor, defined by λ_{eff} and n_s. In brief, the renormalization factor λ_{eff}/d is because, in a thin film, the current flow is limited to d orthogonally to the film plane, while in a bulk superconductor, the screening currents can flow through the natural length scale defined by λ_{eff}.

The thickness of our optimally doped $YBa_2Cu_3O_7$ thin films is $d{\sim}150\,\text{nm}$ while the typical values of λ in the a-b plane at low temperatures range from 100 nm to 1 µm. That affects how the magnetic field decays from the edge of the sample into its center and, more importantly for type II superconductors, the size of the screening currents around superconducting vortices (discussed in Section 2.7). In this configuration, the size of a vortex increases to $\lambda_{\perp}$ from λ, and the functional dependence describing the decay of these currents at a distance bigger than λ from the vortex changes from $e^{-r/\lambda}$ valid in the bulk case to $1/r^2$ for $r > \lambda_{\perp}$.

2.6 Type I superconductors

As pointed out in our discussion, superconductivity is characterized by peculiar magnetic properties. The fact that, for instance, the magnetic field B should be zero in the volume of a superconductor indicates that there exists a specific critical field (H_c) above which the applied magnetic field would destroy the superconducting order and bring the sample into its normal state. This idea is indicated in Figure 2.6, showing the temperature dependence of H_c.

The superconducting transition is a second-order phase transition at zero applied magnetic field versus temperature. In contrast, when an external field is applied, the transition becomes first-order with a latent heat associated at $T_c(H_c)$. The existence of a critical field implies that we can define the energy gain associated with superconducting condensation, expressed by the difference in free energy between normal and superconducting state, by equating it to the magnetic energy as [7]:

$$\frac{H_c^2}{2\mu_0} \equiv f_{n0} - f_{s0} \tag{2.13}$$

Where f_{n0} and f_{s0} are, respectively, the Helmholtz free energies densities of the normal and of the superconducting state with no magnetic field applied. This equation is true in the Meissner state when B in the volume of the superconductor is zero and when the sample dimension is sufficiently large to disregard the contribution from the field penetrating the sample in a region λ from the surface. If we reformulate

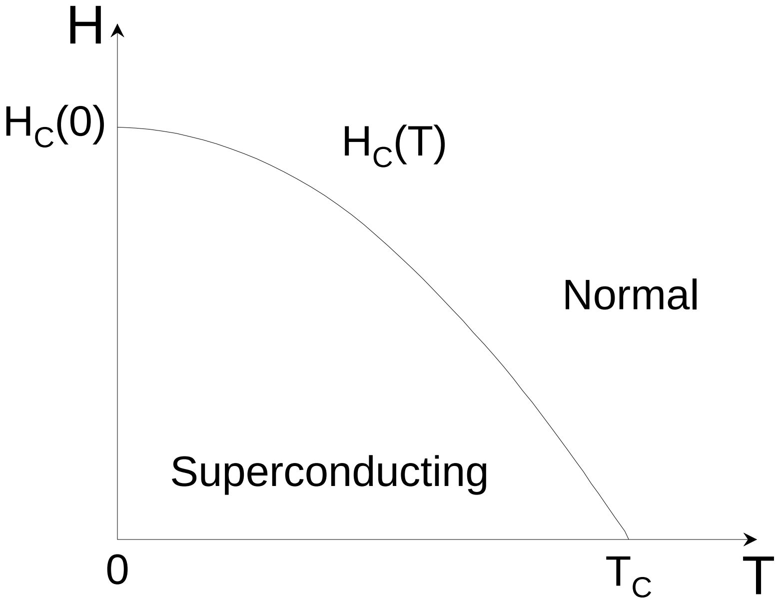

FIGURE 2.6: Critical field versus temperature. Adapted from [7]

Equation 2.13 in terms of Gibbs free energy, which is the adequate thermodynamic potential when the field H is the quantity kept fixed and not B, as happens in an actual experiment:

$$G_n - G_s = V \cdot (f_{n0} - f_{s0}) - V \cdot \frac{H_{app}^2}{2\mu_0} \tag{2.14}$$

With V, the volume of the superconductor, G_n and G_s, the Gibbs free energies of the normal and the superconducting state respectively. Inserting Equation 2.13 into Equation 2.14, we see that when $H_{app} = H_c$, the normal and the superconducting state have the same energy and can coexist. This situation in type I superconductors is called *intermediate state*. In this regime, some fractions of the sample maintain superconducting properties while others are in the normal state, and the applied magnetic field can thread through them (see Chapter 2 of [7]). The specific pattern of normal regions is set by the energy balance between the cost of bending the magnetic field lines out of the sample and the *positive* cost of creating a domain wall between a normal and a superconducting region. The magnetic flux density threading the normal regions is $\sim H_c$.

Although this state might seem analogous to the *mixed state* of type II superconductors discussed in Section 2.7, there are substantial differences. First, the size of the normal regions in the intermediate state is macroscopic and not fixed to the microscopic value of the coherence length, and it varies with the applied magnetic field. Second, the magnetic flux penetrating a type I superconductor is not quantized, as it is for fluxoids in type II superconductors. These distinct behaviors can be traced back to the different energy costs of a domain wall for type I and type II superconductors. The cost of a domain is approximately given by:

$$\gamma = \frac{H_c^2}{2\mu_0} \cdot (\xi - \lambda) \tag{2.15}$$

,

Where ξ and λ represent the coherence length and the magnetic field penetration depth defined in the framework of the Ginzburg Landau theory, their meaning is schematically depicted in Figure 2.7: the coherence length represents the spatial distance over which the superfluid density (represented in the Ginzburg Landau theory by the square modulus of the superconducting wave function) can change without additional energy cost. At low temperatures, the Ginzburg Landau coherence length coincides with the value introduced by Pippard (see Equation 2.6). λ represents the characteristic length scale for gradients in the magnetic field inside the sample (analogously to the penetration depth defined earlier). For a type I superconductor, ξ is bigger than λ, and the cost of generating a domain wall is positive. The opposite is valid for a type II superconductor with energetically favorable domain walls.

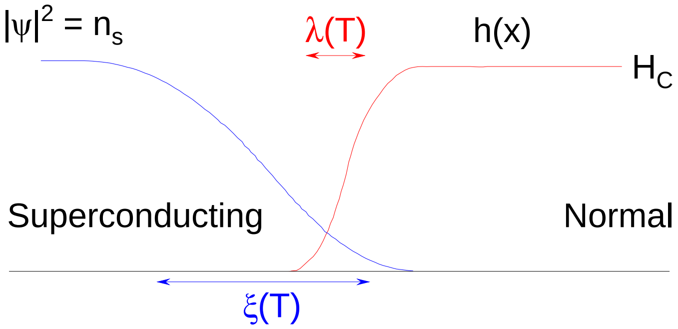

FIGURE 2.7: Coherence lenght versus magnetic field penetration depth. Adapted from [7]

2.7 Type II superconductors

Abrikosov defined type II superconductors before their experimental discovery [26]. He imagined the implications of a superconductor with $\lambda > \xi$ in the framework of the Ginzburg Landau theory. A convenient parameter to predict the magnetic properties of different superconductors is $\kappa = \lambda/\xi$, which is temperature-independent below T_c. Type I pure superconductors have typical values of $\lambda \sim 50$ nm and of $\xi \sim 300$ nm. Therefore, $\kappa \ll 1$ which implies positive surface energy associated with a domain wall between normal and superconducting regions as discussed in Section 2.6 when discussing the intermediate state of type I superconductors. In 1957, Abrikosov examined the properties of a hypothetical superconductor with $\kappa > 1$ ($\xi < \lambda$), in which domain walls between normal and superconducting regions would tend to form spontaneously having a negative energy density. To distinguish this new class of materials with entirely new properties, he called them superconductors of the *second group* or type II superconductors.

To be more precise, the breakpoint between the two different regimes happens at $\kappa = 1/\sqrt{2}$. For $\kappa < 1/\sqrt{2}$, we have type I superconductivity, while $\kappa > 1/\sqrt{2}$ defines type II superconductors. This second group does not show any breakdown of the superconducting order at H_c but displays flux penetration in the form of an array of vortices at a field higher than H_{c1} ($< H_c$). Superconductivity is completely disrupted at a second critical magnetic field called $H_{c2} = \sqrt{2}\kappa H_c \gg H_c$. A type II superconductor held in a magnetic field ranging between H_{c1} and H_{c2} is said to be in the *mixed state*. In that state, the magnetic field is allowed into the volume of the superconductor through a pattern of vortices with a normal core and a size of order of the Ginzburg Landau coherence length. Each vortex carries a magnetic flux quantum ($\Phi_0 = \frac{hc}{2e}$) and is spatially confined by superconducting currents around its core. Also in this case, like in the *intermediate state* of a type I superconductor, we have superconductivity without perfect diamagnetism: the magnetic field is allowed in the sample reducing the diamagnetic energy cost in holding the field out the sample volume at the expenses of the lost condensation energy in the core of the vortices.

We must reevaluate the definition of dissipationless transport in the mixed state. In a defect-free superconductor with a transport current J, each vortex sees a Lorentz force per unit length: $F_L = J \times \Phi_0/c$. This force leads to a lateral movement of the vortex, which would produce dissipation for any arbitrarily small J due to the presence of a quasiparticle in the vortex's normal core. In actual superconductors, defects preserve dissipationless transport, the first hallmark of superconductivity. Imperfections of the material pin magnetic vortices and do not allow them to move. Dissipation appears only above a critical value of the transport current when the Lorentz force overcomes the pinning force. That is why defects and pinning centers are deliberately introduced in superconducting magnet wire.

2.8 Extracting the conductivity from the zero-field magnetization

We conclude this chapter by showing a model that allows the extraction of quantitative information about the conductivity of a sample from the size of its magnetic shielding. The idea is to use the Drude model to express the shielding field induced in the sample as a function of the applied field. This theory complements the ultrafast magnetic steps, described in Chapter 7, as a probing technique suited to study the conductivity of photo-excited superconductors and photo-excited states in general.

First, we discuss the range of applicability of the Drude model for superconductors, which we questioned in Section 2.3. In short, we can use this model for high T_c superconductors, like $YBa_2Cu_3O_{7-\delta}$, because in these materials, the coherence length is much smaller than λ or of any typical length scale associated with a change of the electromagnetic field, and the transport becomes almost local. This argument relaxes the critique pointed out earlier and allows us to use the Drude model to describe the sample properties. We assume to deal with a sample having the shape of a thin disk with an azimuthal current j (we use cylindrical coordinates r, ϕ, z):

$$\partial_t j + j/\tau = \omega_p^2 \epsilon_0 E_\phi \tag{2.16}$$

with:

$$\omega_p^2 = \frac{ne^2}{m\epsilon_0} \tag{2.17}$$

n here is the density of carriers. We have yet to specify their nature (superconducting or quasiparticle). We can spatially integrate Faraday's law and take into account the inhomogeneous distribution of the field via a geometric factor g_1 to achieve a relation between the azimuthal electric field and the magnetic field component orthogonal to the sample plane:

$$E_\phi = -\frac{R}{2} \cdot \partial_t (H_{app} + g_1 H_{ind}) \tag{2.18}$$

H_{app} and H_{ind} are the z components at the center of the disk of the local value of the applied field and the induced field, respectively. R is the radius of the disk. Physically, the electric field felt by a carrier results from the externally applied magnetic field and the screening magnetic field, a sort of backaction generated by all other charges in the sample. The factor g_1 only multiplies the induced inhomogeneous field, while the applied field is assumed to be uniform across the sample surface. We then use Ampere's law, after neglecting the contribution from the displacement field, to calculate the induced magnetic field generated by the current in the sample:

$$H_{ind} = \mu_0 g_2 R j \tag{2.19}$$

g_2 is another factor of order unity in which we include the complications connected with the specific details of the current spatial distribution along the radius of the disk. Plugging Equations 2.18 and 2.19 into Equation 2.16, we get a differential equation for the induced field in terms of the applied field:

$$\partial_t H_{ind} + \frac{H_{ind}}{\tau(1+g_1\alpha)} = -\frac{\alpha}{1+g_1\alpha} \cdot \partial_t H_{app} \tag{2.20}$$

with:

$$\alpha = \frac{\omega_p^2 g_2 R^2}{2c^2} \tag{2.21}$$

The geometric factors of the order of unity g_1 and g_2 are a priori not known and depend on the specific sample geometry. Finite element simulations can help extract their values and disentangle them from the characteristic parameters τ and ω_p, which contain information about the intrinsic properties of the sample. We anticipate that these geometric parameters do not influence the conclusions drawn below: a superconductor will behave qualitatively differently than a metallic system. Moreover, in a pump-probe experiment, we can calibrate them by comparing the data taken with the pump off and those taken with the pump on. The particular case of a superconductor is modeled by taking the limit for the scattering time tau to infinity. The Equation 2.20 then reduces to:

$$H_{ind} = -\frac{\alpha}{1 + g_1 \alpha} \cdot H_{app} \tag{2.22}$$

From this, we see that a superconductor's shielding $(1 - H_{ind}/H_{app})$ is proportional to the applied field and is perfect if α, proportional to the carrier density, is much bigger than 1. The other limit is that of a metal with a very short scattering time. In this case, we can assume that we are in steady state conditions and set $\partial_t H_{ind} = 0$. The shielding is, therefore, proportional to the time derivative of the applied magnetic field (as expected from Faraday's law), with scattering time and the density of carriers as the proportionality factors. These two limiting results highlight the qualitative difference between the expected response for a superconductor (or perfect metal) and a standard metal from this technique and justify the simple argument made in Chapter 1. By continuity of the magnetic flux density component perpendicular to a surface, the magnetic field right on top of the center of the sample will be approximately equal to the internal field in the sample, the unknown of the above equations. Our next task will be measuring the field on top of the sample with sufficient temporal resolution. We will explain how we tackled this problem in Chapter 3.

Chapter 3

Ultrafast optical magnetometry

This chapter discusses the main properties of the technique we developed to measure the transient magnetic properties of photo-excited superconductors: ultrafast optical magnetometry. This technique is sensitive to small magnetic field changes and non-invasive, it possesses sub-picosecond temporal resolution, spatial resolution down to a few microns, and it works in a broad temperature range from room temperature down to a few Kelvins. Additionally, we can optimize different aspects of the measurement by changing the type of magneto-optic detector employed. For example, we can optimize the magnetic field sensitivity and use a ferrimagnetic magneto-optic crystal. We achieved a resolution below 50 nT with such a magnetic detector, maintaining a temporal resolution of ∼100 ps. Alternatively, we can push our time resolution by choosing a diamagnetic magneto-optic material like GaP. We measured magnetic transients with a temporal resolution below 1 ps with the latter type of crystal, with a magnetic field resolution of ∼1 µT. In the following, we will discuss the main features of this technique and the precautions we took to achieve such sensitivity.

Ultrafast optical magnetometry is based on the Faraday effect in magneto-optic materials. By placing one of those crystals adjacent to the sample, we can convert the local value of the magnetic field into a measurable rotation of the polarization of an optical beam via the known relation:

$$\theta = V \cdot \int_0^L B(z)\, dz \tag{3.1}$$

Where θ represents the rotation of the polarization of the input beam, $B(z)$ is the magnitude of the magnetic field along the light propagation direction inside the medium, and L is the thickness of the medium. The proportionality constant V is known as the Verdet constant. We will discuss in a later section in more detail the origin of this equation (see Section 3.1) and in two dedicated chapters how its functional form affects spatial and temporal resolution of the experiment (see Chapters 4 and 5).

The reason for using an additional detector to measure the magnetic properties of high T_c superconductors is the fact that no significant magneto-optical Faraday effect has been observed in those materials. Therefore, magneto-optical layers have been used as magnetic field sensing elements [27]. Magnetic imaging of vortices at equilibrium was demonstrated by exploiting the Faraday effect in ferromagnetic crystals and thin films [28, 29, 30, 31]. These types of detectors (such as $\mathrm{Bi:R_3Fe_5O_{12}}$, EuS, and EuSe) offer very high sensitivity ($V \sim 10^5\,\mathrm{rad T^{-1} m^{-1}}$) but have limited time resolution, down to 100 ps at best (see, for instance, [32] for EuS), due to the presence of low lying magnetic excitations (e.g., ferromagnetic resonance) at sub-THz frequencies.

Diamagnetic II-VI and III-V semiconductors such as ZnSe, ZnTe, and GaP have a magneto-optic response featuring Verdet constants two to three orders of magnitude smaller than those observed in ferromagnetic materials. Therefore, thicker detectors are required to accumulate the signal on longer length scales at the expense of the spatial resolution (see Equation 3.1]). Conversely, they are not magnetically ordered and offer significantly better time resolution [33, 34]. Furthermore, their Verdet constant is mostly temperature-independent, ensuring a flat detector response in a broad temperature range.

Our technique builds on and improves previous realizations of optical magnetometry, with the significant difference that we substitute the magnetically ordered detector with a thicker semiconducting one to achieve approximately the 1 ps temporal resolution we need to track the typical dynamics of photo-excited superconductors, while still maintaining sufficient spatial resolution to capture the near field spatial changes of the magnetic field profile across the sample. Specifically, we opted for GaP magneto-optic crystals with a Verdet constant of $\sim 120\,\mathrm{rad T^{-1} m^{-1}}$ [35].

3.1 The Faraday effect

In this section, we discuss the physical origin of the magneto-optic Faraday effect, which happens due to the interaction of light with a magnetized material while traversing it. As discussed in Section 3.2, this effect is more important in our geometry than the magneto-optic Kerr effect, so we focus on the former. Nonetheless, the underlying physics describing the interaction of light with magnetization is the same in both cases. What changes is the way in which the physical observable (the polarization of light) is modified: we consider a plane wave traveling along the direction z, with its electric field polarized along the x direction and the magnetic field along y. Now, the electric field couples with charges of the material via the force: $\mathbf{F}_E = q\mathbf{E}_x$, where q is the charge of the particle. Similarly does the magnetic field, with a force: $\mathbf{F}_B = q\frac{\mathbf{v}_q}{c} \times \mathbf{B}_y$, where in addition the velocity of the charged particle $\mathbf{v}_q$ and the speed of light c appear. In this instance, we express the electric and magnetic forces in *cgs units*. In fact, the magnetic and electric fields in this system have the same units, allowing for a more direct comparison between the forces. For conduction electrons, which are the particles traveling at the highest speed in a solid and which are, therefore, the most sensitive to magnetic fields, the ratio $\mathbf{F}_B/\mathbf{F}_E \sim \mathbf{v}_q/c \sim 10^{-3}$. Moreover, the light at the frequencies typically used to measure the Faraday effect (optical and near-infrared range) does not directly couple to spin excitations [36]. For these reasons, we only consider the electric part of the light pulse when describing its interaction with the material.

We can express the electric field polarized along x as:

$$\mathbf{E}(z,t) = E_0\mathbf{e}_x e^{i(\omega t-kz)} = E_0(\mathbf{e}_+ + \mathbf{e}_-)e^{i(\omega t-kz)} \tag{3.2}$$

Where we also expressed the field as a linear superposition of right circular ($\mathbf{e}_+$) and left circular ($\mathbf{e}_-$) polarized light:

$$\mathbf{e}_+ \equiv \frac{1}{2}(\mathbf{e}_x + i\mathbf{e}_y) \qquad \mathbf{e}_- \equiv \frac{1}{2}(\mathbf{e}_x - i\mathbf{e}_y) \tag{3.3}$$

This basis is useful when we consider light propagating along the positive z direction in a non-absorbing medium where a magnetic field is applied also along the positive z direction. The dielectric tensor below describes the polarization induced by the electric field of light in this situation:

$$\epsilon = \begin{vmatrix} \epsilon_{xx} & -i\epsilon_{xy} & 0 \\ i\epsilon_{xy} & \epsilon_{yy} & 0 \\ 0 & 0 & \epsilon_{zz} \end{vmatrix} \tag{3.4}$$

The off-diagonal imaginary components describe the Faraday effect and are proportional to the applied field: $\epsilon_{xy} \sim H$. We assume that the material is isotropic and homogeneous. Thus, we set $\epsilon_{xx} = \epsilon_{yy} = \epsilon_{zz} = constant$. Such a tensor has eigenvectors $\mathbf{e}_+$, $\mathbf{e}_-$, $\mathbf{e}_z$. That is why we also expressed the electric field as circularly polarized waves. The eigenvalues associated with right circular and left circular polarization are real[1]: $\epsilon_\pm = \epsilon_{xx} \pm \epsilon_{xy} = n_\pm^2$, where n is the refractive index. This difference in refractive index between right circular and left circular polarization results in a different phase delay δ accumulated by these modes as they propagate through the material. This phase delay means that after a certain propagation in the material, the polarization is still linear but rotated by an angle θ_F compared to its initial direction. Assuming a uniform and constant magnetic field H (we do not need to write an integral form as in Equation 3.1) and a propagation length of the light in the medium L [37]:

$$\theta_F = \delta/2 = \frac{\pi L}{\lambda}\,\mathrm{Re}(n_+ - n_-) \tag{3.5}$$

This equation, where λ represents the wavelength of light in vacuum, relates the Faraday rotation to the real part of the difference in refractive index experienced by right and left circular polarized light propagating in the material. In the following, we will heuristically explain the physical origin of magnetic field-dependent refractive index shift for diamagnetic, paramagnetic, and ferromagnetic materials.

---

[1] It is in reality not possible to have a purely real refractive index. As we will see in the remainder of this section, the Faraday effect is sizeable only at frequencies where the refractive index is frequency-dependent. That is usually connected with a resonance in the material, which implies absorption. However, this is still a reasonable treatment in the limit of light being sufficiently red-detuned from the absorption resonance, the case we are considering here.

3.1.1 Faraday effect in diamagnetic materials

In this subsection, we discuss the origin of the Faraday effect in non-magnetic, non-metallic materials, in which, upon application of an external magnetic field, a small (compared to paramagnets and ferromagnets) negative magnetization appears. That is the case relevant to GaP, the magneto-optic detector we chose for our experiments.

The negative magnetization developing in diamagnets can be semi-classically understood in terms of the Larmor precession [22]. To each electron orbiting around the nucleus is associated a magnetic moment μ[2]:

$$\mu = \pi r^2 I = -\frac{e\hbar}{2m_e} \equiv -\mu_B \tag{3.6}$$

Where r and I are, respectively, the mean radius and the current associated with the orbit of the electron, m_e is the mass of the electron and μ_B is the Bohr magneton in SI units, and e is the electronic charge. In the presence of an externally applied magnetic field $\mathbf{H}$, the magnetic moment of the electron will feel a torque $\tau = \mu \times \mu_0 \mathbf{H}$ and start precessing around the magnetic field axis at an angular frequency called the Larmor frequency:

$$\omega_L = \frac{e\mu_0 H}{2m_e} = |\gamma|\mu_0 H \tag{3.7}$$

Where $\gamma = -\frac{e}{2m_e}$ is the electron gyromagnetic ratio, and we assume that the magnetization of the material is negligible and, therefore, $B = \mu_0 H$ (which is a good approximation for diamagnetic materials). This rotation renormalizes the frequency $\omega_{p,0}$ of the probe pulse in different ways for its circular components: the frequency of the right circular component is reduced by ω_L and, conversely, the frequency of the left circular component is increased by the same amount. Intuitively, we can think about this effect as a Doppler shift. After the application of the external field, the electrons begin an additional magnetic-field-induced precession at frequency ω_L around the nucleus. This rotation has the same sign of the rotating electric field of right circular polarized light with Poynting vector $\mathbf{k}$ parallel to the applied field and sign opposite to the counterrotating electric field of left circular polarized light. Therefore, in the frame of reference of the electrons, the electric field of the right circular probe light has a lower frequency $\omega_{p,+}$ than that of left circular light $\omega_{p,-}$. Now, if the refractive index varies with frequency, as happens close to an optical transition at frequency ω_0, sampling it at two different frequency values ($\omega_{p,+}$ and $\omega_{p,-}$) leads to a finite difference of refractive index and therefore to a non-zero Faraday rotation:

$$\theta_F \sim n_+ - n_- = n(\omega_{p,+}) - n(\omega_{p,-}) \neq 0 \tag{3.8}$$

These concepts are summarized in Figure 3.1, where for the real part of the refractive index n we used the form deriving from classical atomic models [38, 39]:

---

[2] we neglect here the contribution of the nuclei that have an associated magnetic moment at least three orders of magnitude smaller than electrons

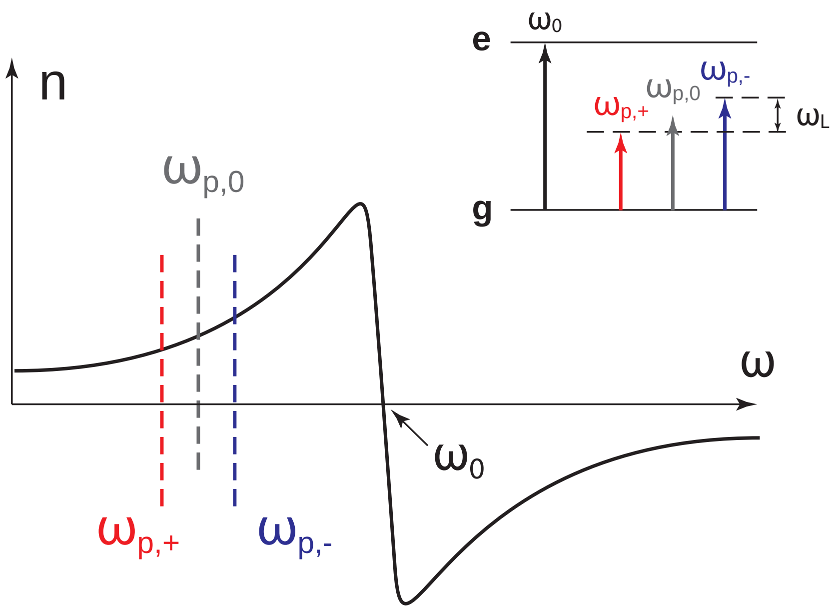

Figure 3.1: The figure shows schematically how the frequencies of right ($\omega_{p,+}$) and left ($\omega_{p,-}$) circular light split upon the application of an external magnetic field, compared to the frequency of light in vacuum ($\omega_{p,0}$). This results in two effectively different values of the refractive index for the two circular polarizations.Adapted from [37]

$$n^2(\omega) = 1 + \frac{Ne^2}{m_e\epsilon_0}\frac{1}{\omega_0^2 - \omega^2} \tag{3.9}$$

With N, ϵ_0, and ω_0 being the density of electrons, the dielectric constant of vacuum, and the resonance frequency of the absorption. This model, although primitive, is found to describe well the experimental data measured in non-magnetic glasses [37]. Alternatively, we can imagine that the frequency of the probe does not change but that the excited state of the optical transition splits and that the transition energy for the right circular and the left circular components of the polarization red shifts and blue shifts, respectively. In this case, the refractive index effectively splits into two curves, one for each renormalized resonance frequency. This picture is shown in Figure 3.2.

The splitting of the transition energies is of the order of the Larmor frequency. This frequency for any practical applied magnetic field is much smaller than the frequency of the unperturbed optical transition. Moreover, away from the transition, the refractive index change with frequency is relatively small. Therefore, we are allowed to say that $n_+ - n_- \sim \frac{dn}{d\omega} \cdot \omega_L$. We can use Equation 3.5 to calculate the Faraday rotation angle:

$$\theta_F = \frac{e\lambda}{2m_e c}\left(\frac{dn}{d\lambda}\right) BL \tag{3.10}$$

From this equation, we can recognize the usual form of the Faraday rotation expressed in terms of the Verdet constant V:

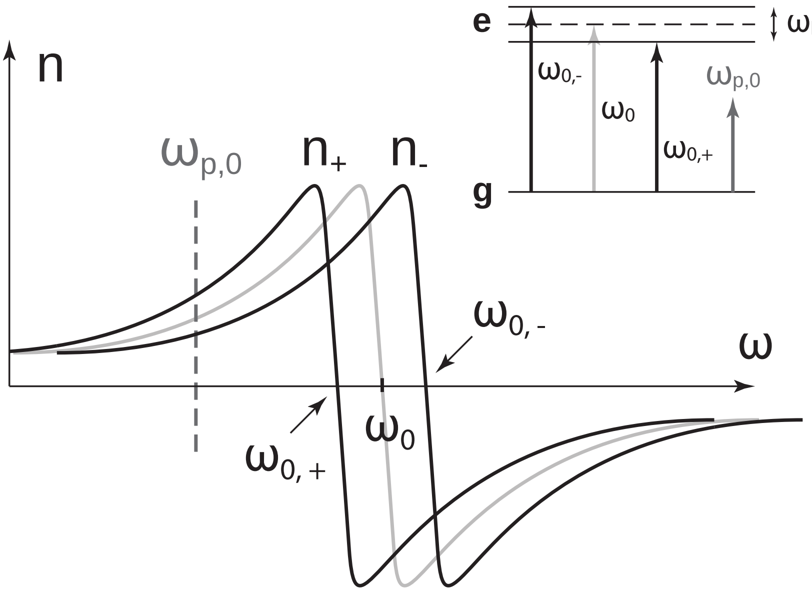

FIGURE 3.2: The figure shows schematically how the refractive indexes for right circular (n_+) and left circular (n_-) light are split upon the application of an external magnetic field compared to the unperturbed refractive index. That results in two effectively different refractive indexes for circular right and left polarizations.Adapted from [37]

$$\theta_F = VBL \tag{3.11}$$

And thus:

$$V = \frac{e\lambda}{2m_e c}\left(\frac{dn}{d\lambda}\right) \tag{3.12}$$

That is the Becquerel formula, connecting the Verdet constant to the dispersive refractive index of the material. For diamagnetic materials, the Faraday effect is weakly temperature dependent due to the fact that the main contribution to the temperature dependence is connected with the thermal expansion of the material [37]. That is another crucial reason why a diamagnetic crystal like GaP represents a good candidate for a magneto-optic detector.

3.1.2 Faraday effect in paramagnetic materials

The Faraday effect in paramagnetic and ferromagnetic materials can be understood similarly to diamagnets. The main difference for paramagnets is that the optical transition's ground state splits, not only the excited state. The splitting of the ground state, Δ, is proportional to the Zeeman splitting and can be understood as the action of the external field aligning the spins of the magnetic ions in the sample along the same direction. Right circular and left circular polarization couple selectively to specific Zeeman split levels, so, analogously to diamagnetism, the refractive indexes for left and right circular polarization split (see Figure 3.3), by an amount Δ proportional to the applied magnetic field applied via the paramagnetic susceptibility [37]:

$$V_{par} \sim \frac{\nu^2 \chi_{par}}{g} \sum_{a,b} \left(\frac{C_{ab}}{\nu^2 - \nu_{ab}^2} \right) \tag{3.13}$$

Where ν is the frequency of light, C_{ab} the transition probability, ν_{ab} the frequency of the transition, g the Landé factor, and χ_{par} the paramagnetic susceptibility of the sample, which has a strong temperature dependence $\sim 1/T$ (see for instance [22]). We understand this temperature dependence in terms of thermal fluctuations counteracting the alignment of the spins induced by the applied field; as a result, the ground state is not the only populated state, but the other Zeeman split levels are populated, albeit much less. This is qualitatively shown in Figure 3.3, where the refractive index for right circular polarization is strongly reduced, indicating the diminished coupling of the material to this polarization due to the low population of the states coupling to it.

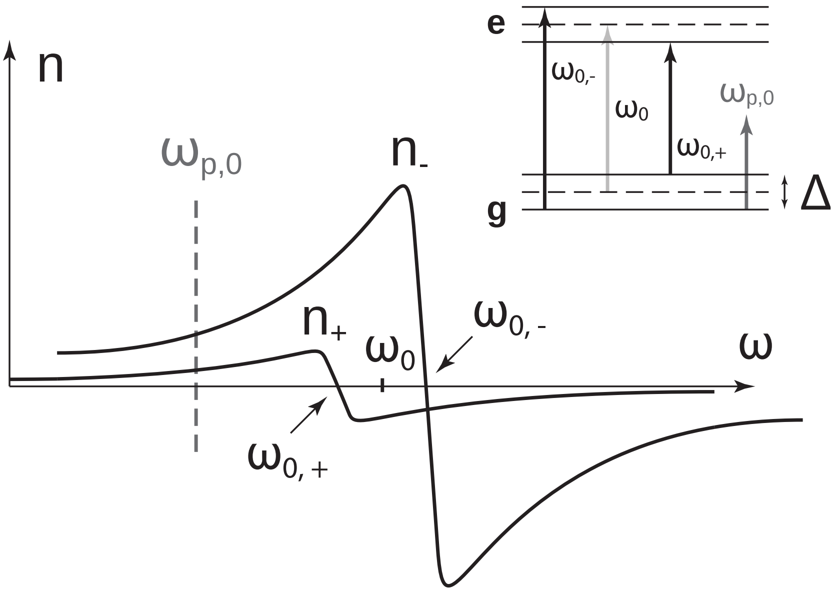

FIGURE 3.3: The figure shows schematically how the refractive indexes for right circular (n_+) and left circular (n_-) light are split upon the application of an external magnetic field compared to the unperturbed refractive index. For paramagnets, the effective refractive index is also influenced by the change in the ground state population after the Zeeman split. That results in two effectively different refractive indexes for circular right and left polarizations.Adapted from [37]

That unbalance in population has also the macroscopic effect of changing the *sign* of the Verdet constant for paramagnets compared to that of diamagnets. To be more precise, the Verdet constant of a paramagnet is composed of two contributions, both the paramagnetic and the diamagnetic $V = V_{par}(< 0) + V_{dia}(> 0)$. Usually, the paramagnetic contribution is the strongest. However, the balance can be shifted by reducing the density of paramagnetic ions, to the point to which it is possible to achieve a material with zero Verdet constant.

3.1.3 Faraday effect in ferromagnetic materials

Ferromagnetic materials can be treated like paramagnets with a much more significant splitting between the ground state levels (see Figure 3.3). For comparison, to explain the splitting of the ground state levels of a ferromagnet in terms of the Zeeman effect, we would need to invoke the presence of a *fictitious* internal field, the exchange field, orders of magnitude larger than typical fields can be practically generated. This considerable energy difference between the different spin states of the ground state also means that, at low temperatures, thermal fluctuations have a lower impact on changing their population. At higher temperatures, the Verdet constant follows the temperature dependence of the magnetization [37]. Hence, the sensitivity of a magnetic detector based on this class of materials would strongly suffer from their temperature-dependent magnetization, potential hysteresis, and domain wall dynamics.

Due to the exchange coupling, there is a preferential direction for the spins within a magnetic domain, even in the absence of an applied field. That indicates the presence of a splitting in the ground state, which can lead to a finite Faraday effect without an applied magnetic bias. It is, therefore, evident that the Faraday effect in ferromagnets results from a coupling of light with the sample's magnetization. Indeed, the externally applied magnetic field's primary role is to change the size of the magnetic domains or the direction of the magnetization compared to the Poynting vector of light. Qualitatively, the magnitude of the external field is not comparable to the size of the exchange field, and thus, the former does not modify the splitting of the ground state levels, which determines the Faraday effect. That is true also for the demagnetizing field, which results from the magnetization itself and is particularly important for thin samples (see Section 2.4). That is why, when measuring the polarization rotation in a ferrimagnetic sample, for which the comments made above hold true, we track the dynamics of the magnetization rather than the dynamics of the applied field, as shown in Chapter 7. The fact that the magnetization aligns with the direction of the applied field over time scales limited by slow spin-lattice relaxation times [40] explains why the response time of ferro/ferrimagnetic detectors is much slower compared to that of diamagnetic semiconductors, in which fast electron-electron scattering processes govern the time scales. That ultimately determines the temporal resolution of different materials used as magneto-optic detectors.

We conclude this section with a last consideration that applies both to paramagnetic and ferromagnetic materials. In general, light couples with the orbital angular momentum of matter. The applied magnetic field mostly couples with the spin part of the electronic wavefunction via Zeeman interaction. Without a connection between the orbital part and the spin part of electronic wavefunctions, the Faraday effect would be blind to the evolution of the magnetization in a magnetic material. However, we experimentally know this effect is especially marked in these materials. The key is the spin-orbit coupling that links light and the spin of electrons [22].

3.2 Experimental geometry

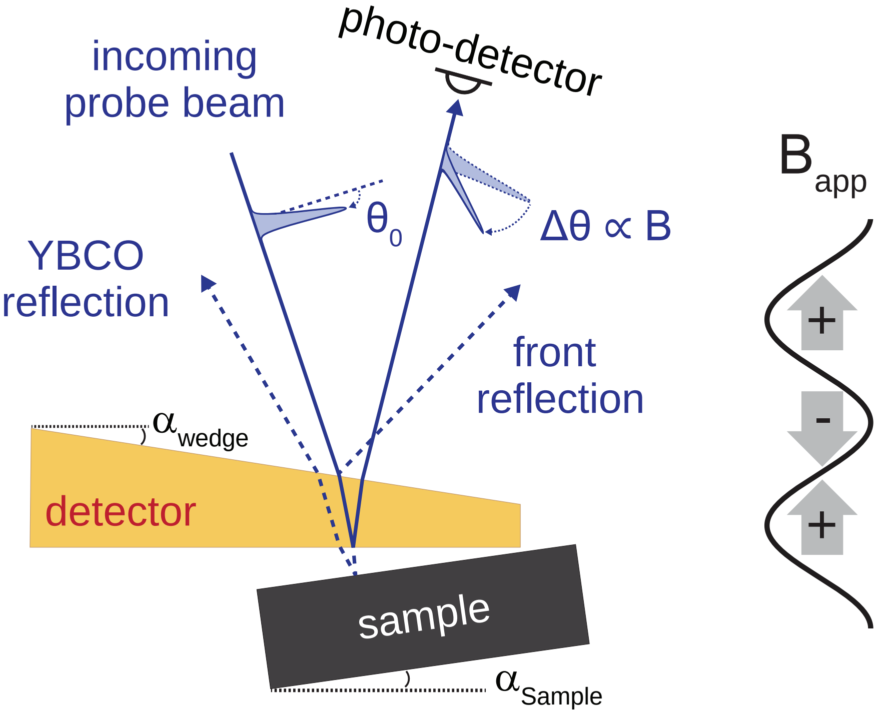

Figure 3.4: Experimental geometry for ultrafast optical magnetometry. The dashed lines represent the reflections of the probe beam that do not get analyzed, while the solid line represents the reflection carrying the magnetic signal whose polarization is analyzed. The GaP detector is wedged to separate the front and back reflections. The front surface of the sample is mounted at an angle to the GaP back surface to separate the respective reflections. θ_0 is the angle of the incoming polarization compared to a reference angle. $\Delta\theta$ the polarization rotation connected to the magnetic field. We apply an external magnatic bias (B_{app}) that switches polarity periodically.

Figure 3.4 shows essential details of the experimental geometry. Our superconducting samples are mostly opaque at 800 nm and do not show a strong Faraday effect. Therefore, we place an external magneto-optic detector on top of them, which we use to measure the local magnetic field change in their proximity. If the sample magnetizes, it modifies the uniform external magnetic field applied, altering the density of magnetic field lines in a region close to its volume (see Figure 3.4). The magneto-optic crystal close to the sample senses this change in the field. Another significant advantage of using an independent magneto-optic detector in pump-probe experiments is avoiding the ambiguity connected with direct magneto-optical measurements in the photo-excited sample. In the latter case, it is often difficult to disentangle magnetic signals from non-magnetic higher-order optical effects induced by the pump in the excited material (see, for instance, the comments made in [41] about the experiment described in [42]). By measuring outside the sample in an independent magnetic detector, which is protected from the pump radiation (see Chapters 5 and 6), we are exclusively sensitive to the magnetic field generated by the magnetization of the sample.

The average value of the magnetic field across the magnetic detector is measured with an incoming optical probe pulse traveling through it, reflecting from its back surface and emerging in a different direction than the incoming beam. The polarization rotation accumulated through the crystal before the reflection sums to the rotation accumulated after the reflection. That is because upon reflection, the circular components of the probe are swapped, and the Poynting vector changes direction compared to the magnetic field. Therefore, when measuring a static magnetic field, the polarization rotation is proportional to twice the thickness of the detector. The outcoming beam carrying the magnetic signal is measured as described in Section 3.3. A common way to increase the signal in this geometry is to deposit a mirror layer onto the back surface of the detector to increase the reflection and the intensity of the light carrying the Faraday signal. The usual choices are metallic or dielectric coatings, with a thickness of $\sim$100 nm, which does not significantly increase the distance between the sample and the detector, impacting the measured signal (see, for instance, [30] and [27]). Both of these options are not viable in our case. On one side, dielectric coatings are almost inevitably a source of strain when cooling the sample due to the difference in thermal expansion coefficients between the coating and the magneto-optic crystal. Strain, in turn, induces birefringence, which negatively affects polarization measurements (see Subsection 3.4.1). On the other, metallic coatings are not suited when measuring fast changes in the magnetic field. As schematically shown in Figure 1.7, metallic layers shield magnetic transients and, hence, influence the intrinsic signal from the sample. Without a reflecting layer for the probe, we need to tilt the sample to the back surface of the magneto-optic detector to exclude the reflection from the sample surface (see Figure 3.4).

We want to stress that even if we are measuring in a reflection geometry, the sensitivity of our technique is mainly associated with the Faraday effect rather than the magneto-optic Kerr effect (MOKE). That is the case because we analyze the light traveling twice through the whole magnetic detector thickness after reflecting from its back surface and not directly the radiation reflected from its front surface. In fact, both those magneto-optical phenomena relate the local value of the magnetic field in a magneto-optic medium to a polarization rotation [43]. The difference is the effective length of the interaction, which corresponds to the total thickness of the magneto-optic crystal in the case of the Faraday effect and to the depth explored by the reflected probe pulse below the front surface in the case of MOKE. Given the thickness of our magneto-optic detector, ∼70 µm, and the fact that it is transparent at the wavelength of our probe, it is advantageous to measure in a Faraday-like geometry rather than in a MOKE setting. This argument can be understood by comparing the interaction length of the Faraday effect, ∼140 µm (i.e., twice the thickness of the detector), with the one of the MOKE reflection signal, ∼10 µm. The latter can be estimated for an 800 nm, 100 fs probe pulse traveling in GaP ($n = 3.18$ at 800 nm) by calculating the distance traveled in the medium by the pulse [42].

In Figure 3.4, θ_0 indicates the angle of the polarization of the incoming beam. The dependence of the measured signal on this angle yields information about its nature (see Section 3.3). $\Delta\theta$ is the rotation of the polarization, proportional to twice (the light travels two times through) the average local field inside the magneto-optic crystal. Equation 3.1 describes this process. The magnetic detector is wedged, with an angle α_{wedge}∼1.5 deg. This expedient allows the separation of the reflection generated at the back surface, carrying the magnetic Faraday rotation, from the front reflection associated with a minor magnetic Kerr rotation. Finally, the $YBa_2Cu_3O_{7-\delta}$ samples are mounted at an angle, $\alpha_{Sample} > 1$ deg, relative to the back surface of the magneto-optic detector in order to filter out the radiation transmitted through the whole volume of the GaP and reflected from the surface of the sample. B_{app} is an externally applied magnetic field switching periodically between positive and negative polarity. We anticipate already here that this field has a two-fold function: it is required to study the magnetic response of superconductors (as detailed in Chapter 2) and, by switching, it helps to filter magnetic signals from non-magnetic noise (as discussed in more detail in Section 3.4).

3.3 Polarization analysis

In this section, we discuss how we employ a standard balanced photodetection scheme to extract magnetic signals from the magnetic field-dependent polarization rotation of the probe beam. Figure 3.5 displays the setup used to analyze the polarization state of the probe beam after propagation through the magnetic detector (see Figure 3.4). First, a half waveplate ($\lambda/2$ WP) rotates the polarization of the incoming probe beam to 45 deg from the horizontal. Then, a Wollaston prism separates the vertical (V) and horizontal (H) components of the probe pulse into two beams, each one hitting one of the two photodiodes (which we call A and B) of a balanced photodetector. This device measures the intensity of the two beams and outputs two analog signals equal to the average intensity of the two photodiodes and their difference multiplied by a gain factor. We call these output channels the "sum channel" and "difference channel." We use the sum channel, independent of the polarization angle, to monitor the probe beam's intensity (and the fluctuations) and the difference channel to measure deviations in the polarization direction from the diagonal.

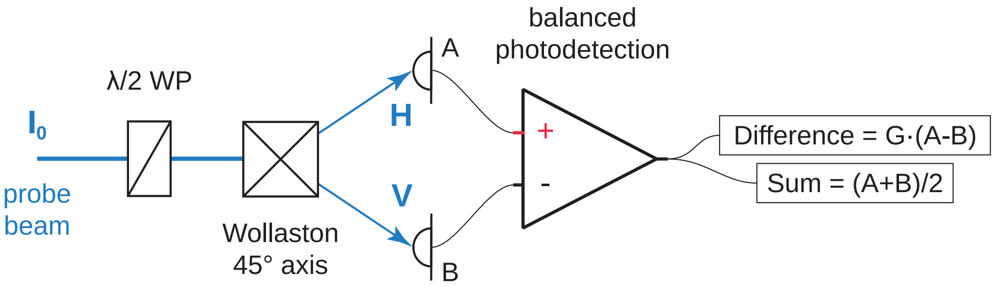

FIGURE 3.5: The figure shows the experimental setup used for analyzing the polarization state of the probe beam after propagation through the magnetic detector (see Figure 3.4). The setup comprises a half waveplate ($\lambda/2$ WP), a Wollaston prism, and a balanced photodetector.

Depending on the angle of the incoming polarization (θ_0 in Figure 3.4), the fast axis of the half waveplate can be adjusted to set the polarization of the probe to 45 deg and to achieve an equal intensity on both the horizontal and vertical channels of the balanced photodetector. That means that the intensity on the difference channel is zero, and we are measuring it in an extinction configuration. In practice, achieving perfect balance and total extinction is impossible due to noise or systematic errors. Moreover, these polarization rotation sources can be time, temperature, or position-dependent, making it difficult to separate them from a magnetic signal. By periodically switching the polarity of the applied magnetic field, our measurement protocol strongly rejects these non-magnetic contributions to the polarization rotation and highly increases our signal-to-noise ratio.

Figure 3.6 shows the different angles involved in the measurements of polarization rotation. The blue arrows indicate different directions of the polarization of the probe beam, with intensity I_0, right before the Wollaston prism. θ represents the probe's polarization without an applied magnetic field. The value of θ slightly differs from 45 deg (coinciding with the axis of the Wollaston, black dashed line) due to minor errors[3] that do not allow to achieve a perfect balancing. When a magnetic field H^- orthogonal to the magneto-optic detector with negative polarity is applied (see Figure 3.4), the polarization rotates additionally of an angle α^-. In the same way, when a field H^+ with positive polarity is applied, the polarization rotates by an angle α^+ opposite to α^-. The Wollaston prism separates the incoming polarization beams' horizontal and vertical projections. In our geometry, the horizontal projection, H, is measured by the photodiode A, and the vertical projection, V, is measured by the photodiode B. That means the two outputs of the balanced photodetector read: $S = (H + V)/2$ for the sum channel and $D = G \cdot (H - V)$ for the difference channel. We use these

---

[3] For instance, slight changes in the ellipticity of the probe beam due to tiny drifts of the probe position across the magneto-optic detector during the measurement or imperfections of the polarization analysis optics (i.e., a nonperfect half waveplate).

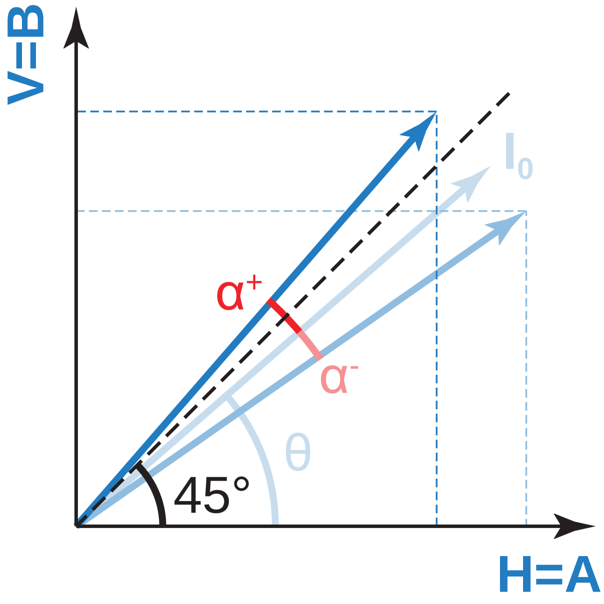

FIGURE 3.6: The blue arrows indicate different directions of the polarization of the probe beam. The black dashed line represents the axis of the Wollaston prism. The red angles α^+ and α^- indicate a Faraday rotation due to a positive magnetic field B^+ and a negative B^-, respectively.

two quantities to quantify the intensity of the probe beam, its average angle θ, and the polarization rotation angle induced by a magnetic field α. In our convention:

$$H = I_0 \cos^2(\gamma) \tag{3.14}$$

$$V = I_0 \sin^2(\gamma) \tag{3.15}$$

Where γ indicates an arbitrary angle (i.e., regarding Figure 3.6, γ is a placeholder for θ, α^+ or α^-). So, we can directly see that the sum channel of the photodetector is proportional to the intensity of the probe beam, independently of the angle of the polarization:

$$S = \frac{H+V}{2} = \frac{I_0}{2} \tag{3.16}$$

The difference channel is instead proportional to the angle $\delta = \gamma - 45\,\mathrm{deg}$, assuming we are measuring in an almost balanced configuration (i.e., $\delta \ll 1$):

$$D = G(H - V) = GI_0 \cos(2\gamma) = GI_0 \sin(2\delta) \sim GI_0 \cdot 2\delta \tag{3.17}$$

So, from this channel, we can extract the angle of the polarization. Without noise and other contributions to the polarization rotation, these two pieces of information would be enough to execute our measurements. We would see a rotation of the polarization when we apply the magnetic field, and by comparing it to the angle of the polarization without the field, we could extract the value of the field in the magneto-optic detector. In reality, this is not the case, and we have other contributions to the polarization rotation, low-frequency noise, and fluctuations in the intensity of the probe laser. To suppress the effect of intensity fluctuations on our precision in determining the polarization angle, we define a new quantity, the *normalized balancing* (NB):

$$NB = \frac{D}{S} \sim 4G\delta \tag{3.18}$$

To suppress non-magnetic contributions and low-frequency noise, we switch the polarity of the applied magnetic field at a rate ranging from 10s to 100s Hz, and we subtract the measurements done with opposite polarities. To this purpose, we define a new quantity called *normalized magnetic* (NM):

$$NM = \frac{D^+}{S^+} - \frac{D^-}{S^-} \sim 4G(\delta^+ - \delta^-) = 4G(\alpha^+ - \alpha^-) = 8G\alpha \tag{3.19}$$

Where the exponent + and - represent positive and negative polarity of the applied field respectively, α^+ and α^- are defined as in Figure 3.6 with $\alpha^+ = -\alpha^-$ and $\alpha = |\alpha^+| = |\alpha^-|$ is the *amplitude* of the symmetric magnetic field induced rotation. NM is therefore only sensitive to magnetic changes of the polarization, does not depend on the intensity of the probe beam, and is a differential, "lock-in" signal allowing for effective noise rejection (for more details, see Appendix D).

It is essential to underscore that these results are valid only for the quasi-extinction configuration in which the probe beam enters the Wollaston prism at an angle ∼45 deg. When the deviation (x) from the diagonal becomes more pronounced, the approximation $\sin(x) \sim x$ does not hold anymore, and our sensitivity to magnetic rotations becomes sublinear and asymmetric for positive and negative rotations, possibly giving rise to artifacts. We devote Subsection 3.4.1 to discussing the effect of birefringence since it is one of the main causes of deviation of the polarization from the diagonal. We minimize these deviations by minimizing the quantity NB defined in Equation 3.18. To sum up, with the quantities S, NB, and NM, we can extract a complete set of information to characterize the polarization of the probe after propagation in the magneto-optic material and monitor its intensity, its angle, and the magnetic field dependent polarization rotation.

3.4 Noise rejection

In this section, we want to discuss our techniques to reject noise in our measurements. As mentioned above, the first expedient we use to reject signals of non-magnetic origin is to switch the polarity of the externally applied magnetic field. As indicated in Equation 3.19, we subtract signals measured with a positive magnetic field applied and signals measured with a negative field. In this way, we single out only the components of the polarization rotation that depend linearly on the applied magnetic field, such as the Faraday effect. A second way in which we reject noise applies to the pump-probe measurements shown in Chapter 6. In this case, we change the polarity of the applied field periodically and subtract to signals acquired when pumping the sample, the signals measured when the pump is blocked, thus exploiting a doubly differential measurement protocol. These precautions alone are insufficient to guarantee the signal-to-noise ratio necessary for these experiments. Moreover, we need to be aware of potential sources of artifacts to avoid which we made ad hoc design choices for our setups. In the following two subsections, we will tackle the most prominent source of errors we had to deal with (optically-induced) birefringence and polarization noise.

3.4.1 Birefringence versus Faraday effect

The polarization of the probe pulse in GaP can change due to the Faraday effect, Fresnel refraction, and birefringence. The Faraday effect generates a polarization rotation dependent on the magnetic field. That is the signal we are interested in, and we want to minimize any other contribution to the change in polarization. The difference between the reflection, r_s and r_p, and transmission, t_s and t_p, Fresnel coefficients for p and s polarized light, gives rise to a non-magnetic polarization rotation depending on the direction of the polarization of the incident beam (θ_0). However, this Fresnel polarization rotation and the noise associated with it are minor due to the slight incidence angle ($< 10\,\mathrm{deg}$) of the incoming probe beam. Moreover, this rotation is magnetic field independent, so we reject it effectively with our magnetic field differential measurement protocol, and, therefore, we neglect this contribution. Birefringence is the third and last possible source of polarization change that can significantly impact our measurement result. When a material is birefringent, the component of the electric field of the light pulse parallel to the birefringence axis of the sample experiences a different refractive index. Therefore, this electric field component accumulates a phase delay compared to the component orthogonal to this axis, and the overall polarization of the light pulse becomes elliptical. Ellipticity has a detrimental impact on the sensitivity of the measurement since it reduces the magnitude of the Faraday effect. To qualitatively understand this, we can consider the extreme case of a circularly polarized probe beam, i.e., we are considering a case where the ellipticity is maximal. In an isotropic material, such as GaP, such a probe would be totally unaffected by the Faraday effect, which is, in essence, a different phase delay between left and right circularly polarized light (see Section 3.1). A further adverse effect of birefringence is that, to second order, it can rotate the polarization towards the birefringence axis if the birefringent axis is not either orthogonal or parallel to the initial direction of the polarization (this is easily seen using Poincaré sphere). The primary source of non-magnetic birefringence in our setup is the magneto-optic detector. In theory, the refractive index of our (100) GaP detector is isotropic due to the cubic symmetry of the crystal, but in practice, we have birefringence due to strain. To mitigate strain, we avoided depositing dielectric coatings on our GaP detector. Nonetheless, it is challenging in practice to avoid it altogether: for example, fixing the magneto-optic detector to the holder with glue or cooling it can induce some spatially dependent strain throughout the sample and, consequently, some birefringence that cannot be avoided. However, these residual effects are minimal and do not affect the measurement of magnetic signals. Therefore, in principle, there is no apparent preferred polarization direction for the incoming probe beam, which allows us to analyze the symmetry of the signal versus this degree of freedom (see discussion in Subsection 3.4.3). Another possible source of birefringence is non-linear optical interactions between the pump and the probe copropagating in the magneto-optic crystal. Given the high intensity of the pump required to induce superconductivity in $\mathrm{YBa_2Cu_3O_{6.48}}$, these transient non-linear effects can be very pronounced and give rise to spurious contributions that are difficult to disentangle from a real pump-probe magnetic signal. To avoid this problem, we opted for experimental configurations where the pump does not propagate with the probe in the magneto-optic detector. In the experiments described in Chapters 5 and 7, the probe and the optical pump reach the detector and the sample, respectively, from opposite directions. In this way, the sample absorbs the pump and protects the magneto-optic detector from it. In the experiment discussed in Chapter 6, the GaP detector is protected from the MIR pump by a layer of Al_2O_3, which reflects the pump radiation perfectly.

3.4.2 Minimizing polarization noise

Another challenge we had to face to achieve the sensitivity levels discussed above was minimizing the probe beam's polarization noise. The first step was to enclose the sample and the magnetic coils generating the applied field inside a vacuum chamber. Compared to a small cryostat only for the sample, this configuration has the advantage of excluding any possible Faraday rotation of the probe coming from the windows of the cryostat immersed in the externally applied magnetic field. The second primary source of polarization noise is pointing fluctuations of the probe laser beam. That translates into an error in the probe's position in the magneto-optic material. That is converted into angular polarization noise due to the magnetic detector's spatially dependent birefringence (see Subsection 3.4.1). Similarly, the difference in the reflection coefficients for s and p polarized light of mirrors also transforms pointing noise into polarization noise. To mitigate this issue, we installed a closed loop beam stabilizer, which strongly reduces the position and pointing error of the probe beam at frequencies within its bandwidth ($< 1\,\mathrm{kHz}$). We chose two different approaches to reduce fluctuations at high frequencies. We designed the setup used for the experiments presented in Chapters 5 and 7 to have only quasi-normal incidence reflections ($< 10\,\mathrm{deg}$) of the probe onto each optical element between the analyzer setting the incoming polarization and the Wollaston prism splitting the probe beam before the balanced photodiode. The difference between s and p Fresnel reflection coefficients is minimal at such small incidence angles. The other tactic we employed was placing the input analyzer and the optics required for polarization analysis (see Figure 3.5) inside the vacuum chamber directly before and after the GaP detector. This method is used in the setup employed to measure the light-induced magnetic field expulsion (Chapter 6). While the second way is the most effective in achieving the lowest possible noise, it is also technically more challenging to implement due to the constraints imposed by working in a vacuum. More details regarding the setups and their design are outlined in Appendix C.

3.4.3 Parameter dependencies

For completeness, we briefly outline here additional approaches that this technique allows to distinguish spurious signals from magnetic ones. The first possibility is to change the *temperature* and measure how the signal scales. Superconductivity has a typical temperature dependence, primarily due to the sharp superconducting transition at T_c. Barring any unfortunate coincidence, we expect any signal not associated with the sample to show a different kind of temperature scaling and not a sudden change across T_c. Another control parameter that can be changed is the externally *applied magnetic field*. Any magnetic field-dependent parameter, like the sample's magnetization, is expected to show a characteristic dependence on the applied field. Conversely, any non-magnetic signal is not expected to change with the applied magnetic bias, giving us another possible tuning knob to distinguish magnetic signals from artifacts. Since our technique is spatially resolved, we can also resort to *spatial dependencies* to tell apart signals associated with the sample from those that are not. It is reasonable to assume that if the signal scales with the distance from a magnetic sample and disappears when we are far from it, it is connected to the sample's magnetization. Finally, we can also probe the symmetry of the signal measured as a function of the polarization θ_0 of the incident probe beam (see Figure 3.4). Different physical processes present specific symmetries when we examine their *probe polarization dependence*. That is a valuable resource to distinguish time-dependent magnetic signals generated from the sample from their associated electric counterpart (see Chapter 6), a task that would be impossible for the other parameter dependencies discussed above. The flexibility and robustness against external parameters characterizing this technique allow us to tune multiple degrees of freedom to comprehensively explore the phase space of the effect we want to characterize. Moreover, this capability gives us powerful tools to reject signals not connected to the physical phenomenon we are investigating.

Chapter 4

Equilibrium magnetic properties of $YBa_2Cu_3O_{7\text{-}\delta}$

In this chapter, we discuss the equilibrium magnetic properties of $YBa_2Cu_3O_7$ thin films and of a bulk $YBa_2Cu_3O_6.48$ sample, measured with ultrafast optical magnetometry introduced in Chapter 3. The measurements presented in the following are essential to characterize the samples (see Section 4.3) and, even more, to validate the technique. Regarding the latter point, we use spatially resolved measurements of the equilibrium superconducting shielding of the thin $YBa_2Cu_3O_7$ film to prove the spatial resolution of our probe experimentally. We then extract the spatial resolution of the technique, disentangling material response from the bare response function of the probing mechanism, by fitting the measured data with the result of a finite element simulation (see Subection 4.2.2). First, we start in the next section by conceptualizing the main aspects of spatial resolution and introducing some definitions.

4.1 Spatial resolution of confocal optical magnetometry

Equation 3.1 defines the Faraday effect assuming that the Verdet constant (discussed in Section 3.1) of the material is homogeneous in space and that the magnetic field is uniform in the lateral directions x and y. To discuss the spatial resolution of the experiment, we are going to relax the second assumption and write the Faraday rotation angle as a volume integral:

$$\theta_F = V \cdot \int_0^t \int_\infty \int_\infty B_z(x,y,z) G(x,y)\, dx\, dy\, dz \tag{4.1}$$

Where t indicates the thickness of the magneto-optic crystal and G represents the spatial distribution of the probe beam along the x and y directions and has the dimensions of an inverse surface. From this equation, we see that the polarization rotation at a well-defined position of the probe beam is determined by a spatial average of the magnetic field in the surroundings of that position, which is set by the spatial extension of the probe beam. Therefore, it is not possible to resolve gradients of the field generated by the sample over length scales smaller than the size of the probe as we scan their relative position. Another factor contributing to the technique's spatial resolution is the thickness of the detector along the z direction: integrating along z

dilutes sharp spatial changes, which decay fast with the distance from the sample (see, for instance, Figure 4.5 showing the magnetic field generated by the same sample and measured with two detectors of different thicknesses).

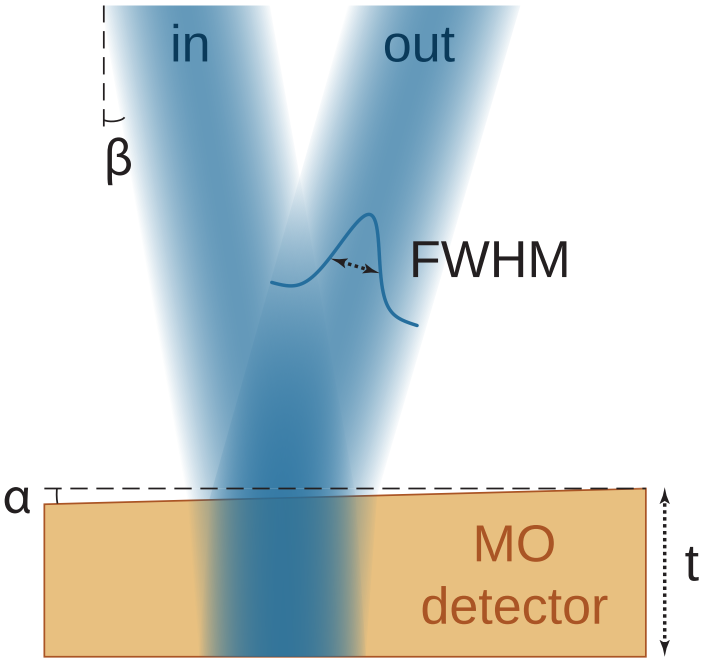

FIGURE 4.1: The figure shows the critical angles and dimensions to define the spatial resolution of optical magnetometry. The blue shaded area represents the incoming ("in") and outgoing ("out") probe beams, which have a Gaussian beam profile (solid blue line).

Figure 4.1 shows the path of the probe in our experiments, summarizing the details crucial to understanding the spatial resolution of the technique: $\alpha \sim 1.5\,\text{deg}$ is the wedge angle discussed in Figure 3.4, $\beta < 10\,\text{deg}$ (exactly 10 deg in the figure for clarity) is the incidence angle of the incoming beam measured from the normal to the back surface of the detector (z direction), $t \sim 70\,\mu\text{m}$ is the thickness of the detector, and $FWHM \sim 50\,\mu\text{m}$ is the full width at half maximum of the Gaussian probe beam.

Given the finite incidence angle $\beta - \alpha$ at the first surface of the detector, the region of the material traversed by the probe is increased by an angle β', determined by Snell law, as $1/\cos(\beta')$. With $\alpha = 1.5\,\text{deg}$, $\beta = 10\,\text{deg}$, and the refractive index of GaP $n = 3.19$ at $800\,\text{nm}$ [44], the angle of the probe beam propagating inside the magneto-optic detector, measured from z, is $\beta' {\sim} 4.2\,\text{deg}$. The correction given by such a slight angle is negligible[1] and we consider the transversal size of the probe beam

---

[1] The configuration discussed here, in which the wedge of the magneto-optic detector is parallel to the incidence plane of the probe, is the most unfavorable and yields the most significant values of β'. Usually, in the experiment, we make sure that the wedge is orthogonal to the probe's incidence plane.

unaffected by it. Moreover, due to the small size of β', we still assume the Poynting vector of the probe beam to be perpendicular to z and to be measuring the component B_z of the magnetic field integrated through the detector size.

We achieve this $FWHM$ at the detector position after focusing the 800 nm probe beam with a lens having a relatively long focal length (17.5 cm). The reflected beam is then picked up by another lens and propagates, collimated, to the polarization analysis setup represented in Figure 3.5. There are multiple reasons for using a lens with a long focal length. Placing the focusing and pick-up lenses sufficiently far from the sample and close to each other allows to keep a slight incidence angle and assume basically normal incidence, important to keep the phase shift between s and p polarized light reflected by the magnetic detector limited. Moreover, a long lens is associated with a long Rayleigh length in the focus (∼1 mm in our case) and a small convergence angle of the beam after the lens. These two factors allow for keeping a well-defined direction of the polarization of the probe beam, which is crucial to measuring polarization rotation. These advantages come at the expense of a less tight focus spot size, which deteriorates the spatial resolution when the thickness of the magneto-optic detector is much smaller than the probe FWHM. This is the case when we use a thin ferrimagnetic magneto-optic detector (see Subsection 4.2.2). For GaP, the factor limiting the spatial resolution is anyways the thickness of the magneto-optic crystal and not the probe spot size.

To summarize, when using optical magnetometry as a probing technique, we are measuring the near-field magnetic distribution generated by a sample, and therefore, spatial resolution is important to capture the details of this pattern and extract important physical properties of the sample. In superconductors, spatially resolved optical magnetometry at equilibrium was crucial to measure the intermediate state of type I superconductor [45], vortex lattices [29] and the London penetration depth [46] yielding physical insights about the properties of this exotic phenomenon.

4.2 Measurements of $YBa_2Cu_3O_7$ thin films[2]

Figure 4.2 shows a micrograph of the 1 mm diameter superconducting $YBa_2Cu_3O_7$ disk and sketches of the sample-detector arrangement with a diamagnetic GaP crystal and a thin ferrimagnetic detector. The superconducting disk shape with a well-defined edge was prepared using optical lithography, starting from an $a - b$ plane 150 nm-thick film of superconducting $YBa_2Cu_3O_7$ grown on Al_2O_3 (see Appendices A and B). The measurement device was assembled by stacking each wedge-shaped magneto-optic detector on top of the superconducting device with spacers to achieve the configuration of angles shown in Figure 3.4.

The superconducting sample and the detectors were subjected to a 2 mT uniform magnetic field applied orthogonal to the planes of the film (z direction) using a

---

This justifies, even more, neglecting the finite propagation angle of the probe inside the magneto-optic detector.

[2] The topics and the data discussed in this section are mostly taken from reference [47]

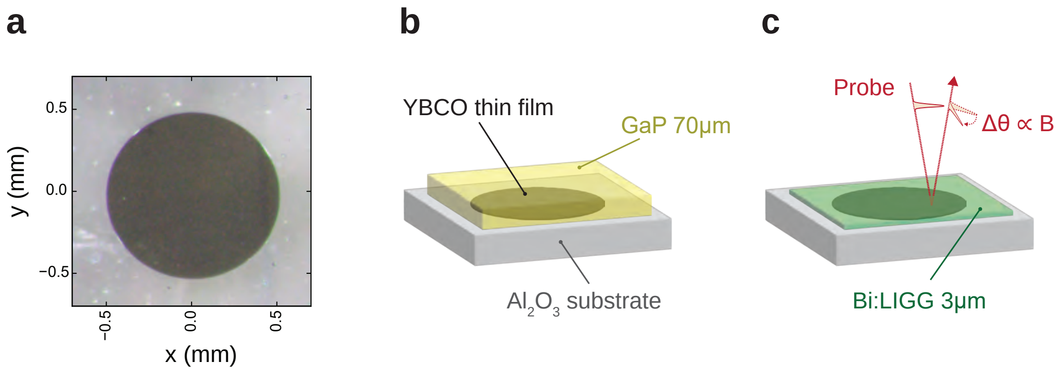

FIGURE 4.2: Micrograph of the lithographically defined $YBa_2Cu_3O_7$ film (**a**) and schematic picture of the sample detector stack with GaP (**b**) and the ferrimagnetic $Lu_2Bi_1Fe_4Ga_1O_{12}$ (**c**). Adapted from [47].

Helmholtz coil pair. The external applied magnetic field H_{app} is sinusoidally modulated in time, synchronously to the laser probe pulse train. The signals acquired with $-H_{app}$ were subtracted from those acquired with $+H_{app}$ to isolate contributions to the polarization rotation having magnetic origin and suppressed potential non-magnetic contributions, as discussed in Section 3.3. Because H_{app} varies in time while the superconducting film is held in its superconducting state, the magnetic response of the sample originates from the exclusion of a time-varying magnetic field rather than the expulsion of a static magnetic field as in the Meissner effect (see Sections 2.1 and 2.2). This protocol is advantageous compared to the use of static magnetic fields because it minimizes the effect of trapped flux and leads to the largest possible magnetic field steps (see Appendix F). The magneto-optic detectors used were GaP and $Lu_2Bi_1Fe_4Ga_1O_{12}$ (or Bi:LIGG for short), a ferrimagnetic material (see Appendix A for more information about the latter) having a different thickness and Verdet constant. To achieve a precise conversion factor between the measured polarization rotation and the local value of the magnetic field at the sample, we opted for a practical approach instead of calculating it using literature values for the Verdet constant and the nominal thickness of the detectors. In fact, their sensitivity was calibrated before each measurement in the exact experimental conditions of the measurement. We measured the amount of angular polarization rotation in a GaP or Bi:LIGG position far from the sample, where the magnetic field was equal to the uniform externally applied magnetic field. In this way, we could extract a calibration factor specific to our experimental conditions. This is mostly important for the Bi:LIGG detector, given the significant temperature dependence of its Verdet constant. Finally, to accurately calibrate the actual value of the magnetic field, the current-to-magnetic field constant of the Helmholtz coil pair was independently calibrated in situ using a Gaussmeter. Using these calibration measurements and accounting for the magneto-optic crystal thickness, we extracted a Verdet constant $V{\sim}120\,\mathrm{rad T^{-1} m^{-1}}$ for GaP, in agreement with reported literature values [35], and $V{\sim}0.5\times10^5\,\mathrm{rad T^{-1} m^{-1}}$ for $Lu_2Bi_1Fe_4Ga_1O_{12}$, in agreement with the values specified by the company producing the devices (see Appendix A).

4.2.1 Superconducting transition versus temperature

The temperature was varied between 40 K and 120 K to track the evolution of the magnetic field above the center of the $YBa_2Cu_3O_7$ disk with the diamagnetic GaP detector (see the central panel of Figure 4.2). As the temperature was swept across $T_c \sim 85\,\mathrm{K}$, a sharp change in magnetic field was observed, indicating the critical superconducting temperature.

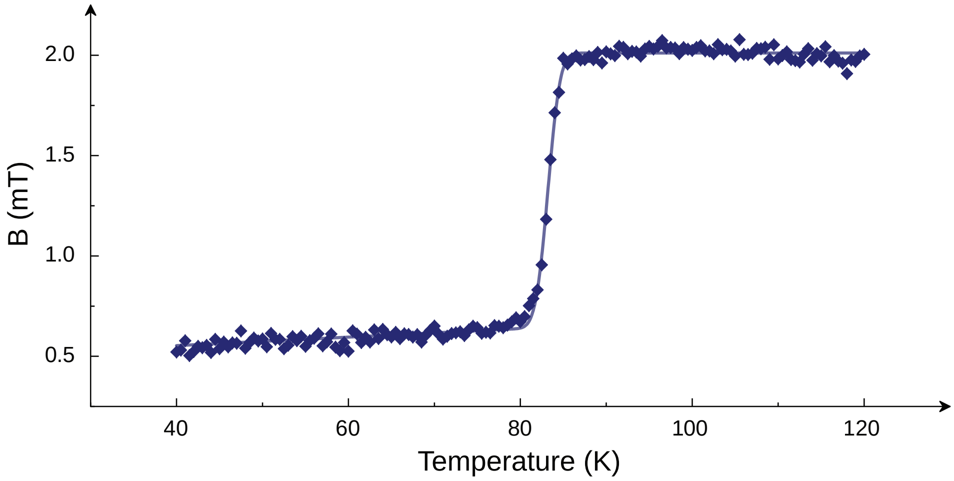

FIGURE 4.3: Magnetic field temperature dependance measured above a $YBa_2Cu_3O_7$ film with a GaP detector. The error bars denote the standard error of the mean. Adapted from [47].

The measured field exclusion is not complete due to the finite thickness of the GaP detector that leads to averaging in the z-direction (see Section 4.1), and the lowest value achieved is $\sim 0.5\,\mathrm{mT}$. Measuring the same sample above its center with a thin magneto-optic detector, like Bi:LIGG, yields a value of the measured magnetic field close to zero (see Subection 4.2.2). This measurement confirms the capability of our technique to measure magnetic fields in a wide range of temperatures and that the superconducting transition of the $YBa_2Cu_3O_7$ film remains sharp and does not shift in temperature after the sample preparation process, including wet etching (see Appendix B).

4.2.2 Spatially resolved measurements

The left panel of Figure 4.4 shows a two-dimensional map of the z-component of the local magnetic field, measured as a function of x and y, the relative position sample-probe, at a constant temperature $T = 30\,\mathrm{K} < T_c$ with the thick GaP magnetic detector. The measured data qualitatively agree with the schematic picture given in Figure 2.2 and with the simulations shown in Figure 2.3: the magnetic field increases

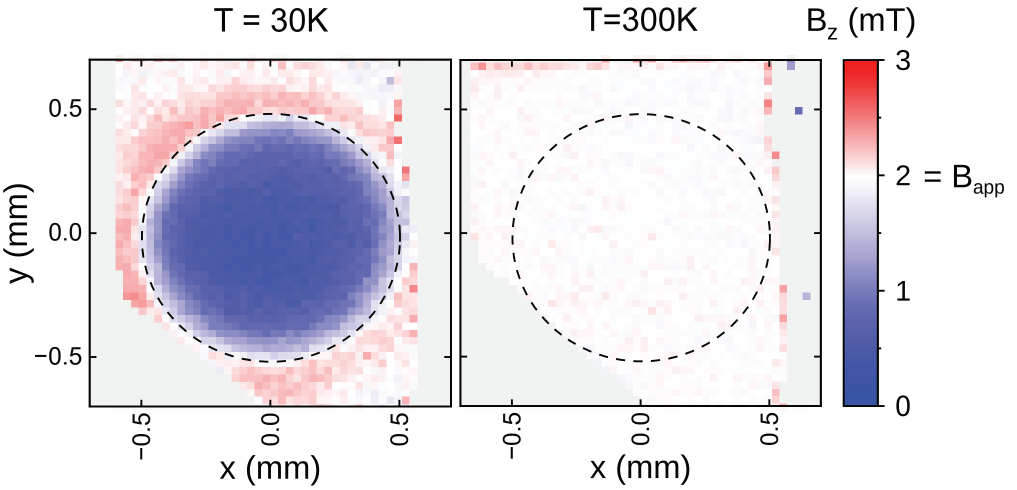

FIGURE 4.4: Bidimensional space map of a $YBa_2Cu_3O_7$ thin film measured with GaP as a magneto-optic detector below and above T_c. Adapted from [47].

near the sample edge (red) and is reduced above its center (blue). The dashed black line indicates the outline of the superconducting disk. The right panel shows the same measurement carried out at a temperature $T = 300\,\mathrm{K} < T_c$. In this case, no spatial dependence is observed throughout the field of view as expected, given the small magnetic susceptibility of the sample above T_c at the frequency of the externally applied magnetic field. The data in both measurements is shown after taking into account the wedge in the GaP detector and correcting for the spatially dependent sensitivity of the measurement due to the change in the thickness of GaP. Like the temperature-dependent measurement, the amplitude of the measured changes is also determined by the geometry of the experiment and the detection crystal thickness. Nonetheless, these data show the capability of our technique of resolving spatially varying magnetic fields. To confirm more quantitatively the factors involved in determining the spatial resolution of our technique, we compare the measured data with a finite element simulation of the superconducting shielding performed with COMSOL. We simulate the magnetic field exclusion in $YBa_2Cu_3O_7$ by modeling the sample as a medium with virtually infinite conductivity and by employing Maxwell's equations to calculate the magnetization it develops when a time-dependent external magnetic field is applied (see Appendix E).

The data points in left and right panels of Figure 4.5 show respectively the z-component of the magnetic field measured in the GaP and in the Bi:LIGG detectors as a function of the distance from the center of the $YBa_2Cu_3O_7$ disk, which is kept well below T_c at 30 K. The Bi:LIGG detector measures a much larger enhancement of the magnetic field at the edge of the superconductor than the GaP because it is thinner and closer to the superconductor than the GaP. We simulate the measured spatially dependent shielding of the sample by first calculating the equilibrium magnetic field

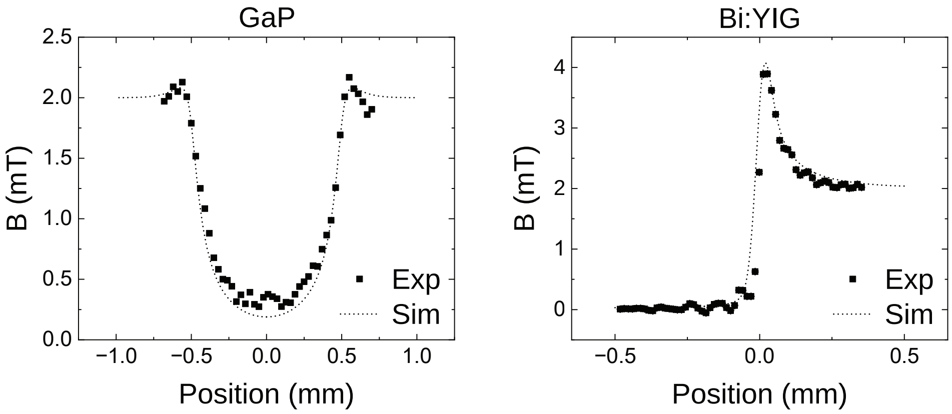

FIGURE 4.5: Measured (data points) and simulated (dotted lines) z-component of the magnetic field obtained while scanning the position of the probe beam across the $YBa_2Cu_3O_7$ disk with the GaP and the Bi:LIGG detectors. Adapted from [47].

distribution in space generated by the $YBa_2Cu_3O_7$ sample and then convoluting the averaged magnetic field across the thickness of each detector with a Gaussian profile (50 µm FWHM) representing the probe beam. To reproduce the geometry of each experiment, we set in the simulations the distance detector-superconductor to 45 µm for the GaP and to 5 µm for the Bi:LIGG. The dotted curves in the Figure show the results of these simulations, which agree with the experimental data. By comparing the measured data and the simulations, we conclude that the spatial resolution of the GaP detector is limited by its thickness (∼75 µm). In contrast, for the Bi:LIGG detector, the probe size (50 µm FWHM) is the defining factor. These results agree with what was discussed in Section 4.1. Moreover, we can confirm the qualitative arguments given in that section by repeating the calculations assuming a point-like probe beam (FWHM ∼1 µm): in doing so, we see that for the GaP detector, the agreement between data and simulations is basically unchanged while for the Bi:LIGG detector the spatial features simulated are sharper than the ones measured. Besides corroborating our interpretation of the spatial resolution of our technique, the measurements taken with the Bi:LIGG detector, due to their higher spatial sensitivity, are useful to set an upper limit to the region of the sample where the critical current is reached: the magnetic field can penetrate the volume of the superconductor in the area where a critical current flows [48, 49]. From the right panel of Figure 4.5, we can see that ∼100 µm away from the edge of the sample, the externally applied magnetic field is completely shielded. This justifies the approximated model, which does not consider the effect of critical currents, employed here and discussed in more detail in Appendix E, to simulate the superconducting shielding.

4.3 Equilibrium properties of $YBa_2Cu_3O_{6.48}$[3]

This section shows measurements performed with optical magnetometry on a $YBa_2Cu_3O_{6.48}$ single crystal. These measurements demonstrate that our technique is suitable for measuring bulk superconductors and helps characterize the equilibrium magnetic properties of the sample. In particular, we will compare these data to the measurements shown in Chapter 6 and highlight the differences and similarities between equilibrium and transient superconductivity.

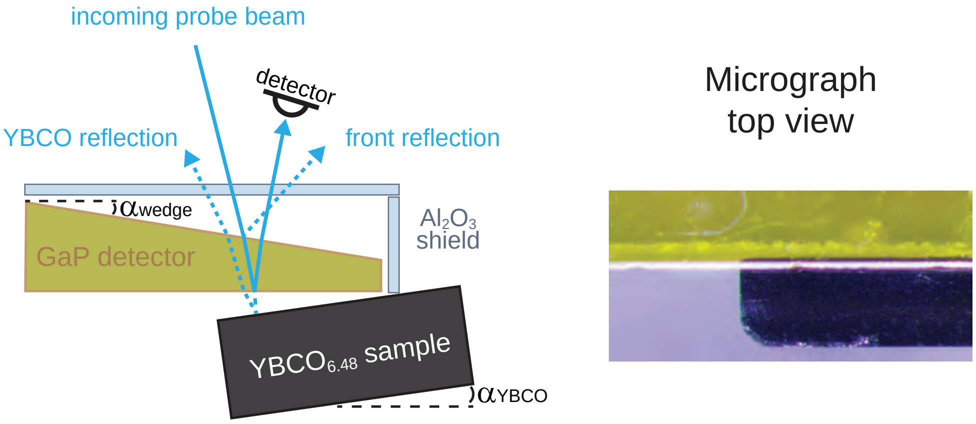

FIGURE 4.6: Experimental configuration for the measurement of $YBa_2Cu_3O_{6.48}$. The dashed lines represent the rejected reflections of the probe beam. The GaP detector is wedged to separate the front and back reflections (α_{wedge}~1.5 deg). The front surface of the sample is mounted at an angle to the GaP back surface to separate the respective reflections (α_{YBCO}~1 deg). The distance between the 30 µm-thick Al_2O_3 shield and the GaP detector is exaggerated for clarity. Adapted from [17].

For the equilibrium measurements shown in this section, we used GaP as a detector to make a meaningful comparison with the ultrafast magnetic field transient measured with the same crystal after photo-excitation above T_c. Indeed, these two measurements have been performed in the same configuration geometry shown in Figure 4.6. As already shown in Figure 1.5, the diamagnetic detector is covered by a thin sapphire slab. This protection layer does not influence the sample's magnetic properties due to the minute magnetic susceptibility of Al_2O_3 [17]. Moreover, the sample-detector stack is mounted to achieve the angle configuration described in Figure 3.4 and select the reflection carrying the magnetic polarization rotation while having the GaP crystal as close as possible, but not touching the cuprate sample. The external magnetic field (B_{app}) is applied orthogonal to the sample a-c plane and the plane of the GaP detector along the beam propagation direction.

---

[3] The topics and the data discussed in this section are mostly taken from reference [17]

The $YBa_2Cu_3O_{6.48}$ sample is a single crystal measuring ∼2 mm × 2 mm in the a-b plane and ∼0.5 mm along the c-axis (see Appendix A for more details about the sample). The sample is mounted, exposing its c-axis so that the polarization of the mid-infrared pump pulse can be aligned along this direction (see Chapter 6).

4.3.1 Temperature dependence

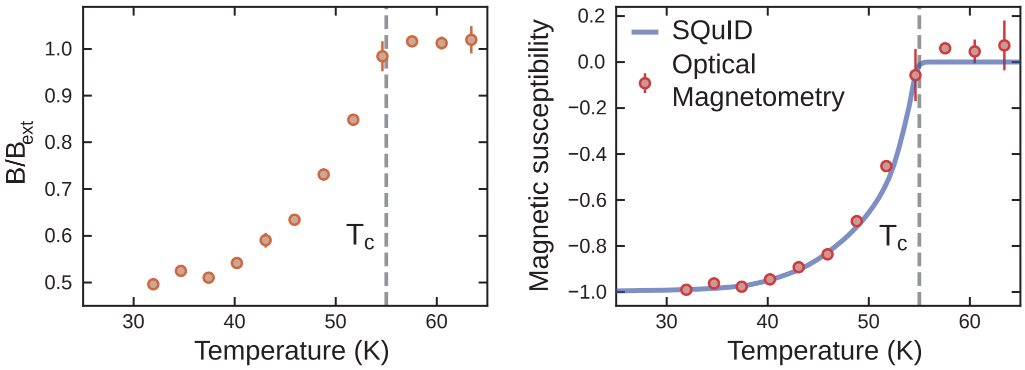

FIGURE 4.7: The left panel shows the magnetic field temperature dependence measured above the $YBa_2Cu_3O_{6.48}$ sample with a GaP detector. The right panel the magnetic susceptibility extracted from the measured data (red data points) and the susceptibility measured with a SQuID magnetometer. The error bars denote the standard error of the mean. Adapted from [17].

The left panel of Figure 4.7 shows the temperature dependence of the measured magnetic on top of the sample. The data are normalized to the externally applied field of 1 mT. Although we do not measure a reduction to zero of the magnetic field due to the finite size of the magneto-optic detector and its distance from the sample, the curve clearly shows a significant drop in the magnetic field at the critical temperature of the sample T_c∼55 K. This result confirms that the device preparation procedure did not influence the quality of the sample.

We then performed a simulation to extract the intrinsic magnetic susceptibility of the sample from the measured data. We used COMSOL to calculate the spatially dependent magnetic shielding[4] of a diamagnetic object with the dimension of the sample and characterized by a uniform diamagnetic susceptibility. We constrained the magnetic field to the value of the externally applied field at the boundaries of the simulation domain, sufficiently far from the sample. We integrated the value of the magnetic field generated by the magnetized object in a region of space coinciding with the region of the GaP detector traversed by the Gaussian probe beam. Finally, we fitted each datapoint measured at a different temperature by modifying the value of the

---

[4] In this experiment, the external applied magnetic field was cycled periodically in time. Therefore, the magnetic field is *excluded* and not expelled from the sample (see Appendix F). That also explains the perfect diamagnetic susceptibility of the sample, which we would not expect from a field-cooled diamagnetic response of the a-c planes of $YBa2Cu3O_{6.48}$.

intrinsic susceptibility of the material to get a calculated value matching the measured value. The result of this fitting procedure is shown by the red data points displayed in the right panel of Figure 4.7 (for more details about the simulation and the conversion into a magnetic susceptibility, see the supplementary material of reference [17]).

In the right panel of Figure 4.7, we also show the magnetic susceptibility of the sample measured with a commercial SQuID magnetometer (blue solid line). The agreement between the two data sets is excellent, validating the capabilities of our measurement technique.

4.3.2 Spatial dependence

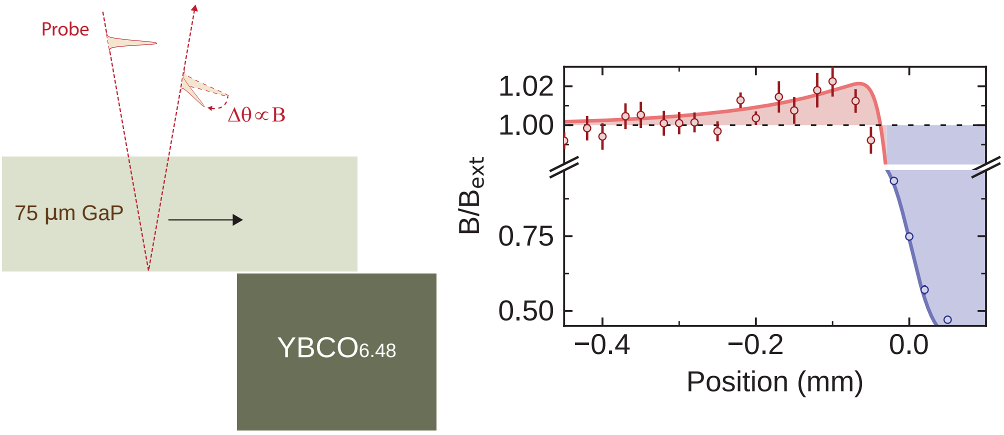

FIGURE 4.8: The left panel represents schematically the experimental configuration, and the right panel the normalized magnetic field measured with a GaP detector. The error bars denote the standard error of the mean. Material from [17].

Figure 4.8 shows the normalized value of the magnetic field measured across the edge of the YBa2Cu3O$_{6.48}$ sample at a fixed temperature $T = 25\,\mathrm{K} < T_c$. The bulk sample qualitatively shows the same behavior of the thin film discussed in Subsection 4.2.2: the magnetic is strongly reduced on top of the superconductor and enhanced at its edges. The small value of the enhancement compared to the reduction is due to the loss of spatial resolution due to the finite thickness of the GaP crystal. Nonetheless, this measurement demonstrates that the technique has enough spatial resolution to measure the increase of the magnetic field at the edge of the superconductor, at least in equilibrium. This feature is crucial for probing magnetic field expulsion in the photo-excited state given the experimental geometry discussed in Chapter 6.

4.3.3 Applied magnetic field dependence

The final measurement discussed here is the dependence of the magnetization of the sample versus the externally applied magnetic field, displayed in Figure 4.9. ΔB

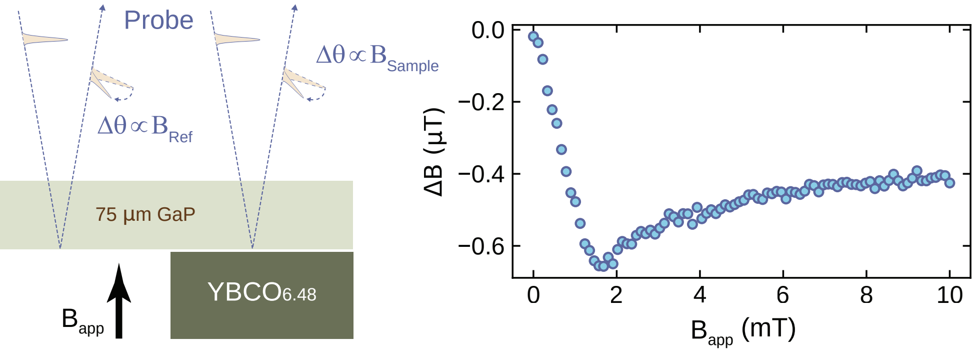

FIGURE 4.9: The left panel represents schematically the experimental configuration. The right panel shows the sample's magnetization while changing the value of the applied field.

represents the difference between the magnetic field value measured on top of the sample and at a reference position far from it (see the left panel of Figure 4.9). Subtraction allows for the correction of experimental systematic errors. Moreover, this difference indicates the behavior of the sample magnetization.

In the low-magnetic-field regime, the superconductor perfectly shields the applied field, as denoted by the absolute value of the magnetization increasing linearly. When the applied field reaches ∼2 mT (in this geometry, the internal field does not deviate significantly from the applied field due to its small demagnetizing factor), the magnetization of the sample saturates, implying that the first critical field H_{c1} of the sample has been reached (see Section 2.7). From this point on, the sample does not screen any further increase of the magnetic field, and the magnetic flux is allowed into the sample volume in the form of magnetic vortices. We shall see in Chapter 6 that this result does not match the magnetic-field dependence of the *expulsion* associated with the photo-excited state.

Chapter 5

Ultrafast disruption of superconductivity

This chapter discusses the time resolution of ultrafast optical magnetometry. First, we consider briefly the main factor determining the time resolution. Then, we present experimental data showing ultrafast magnetic field transients measured with our technique. This result demonstrates the suitability of this experimental method to search for a magnetic field expulsion in photo-excited superconductors (see Chapter 6).

5.1 Temporal resolution

Assuming the dynamics of the change in the magnetic field is instantaneous, the first aspect limiting the measured Faraday rotation is the temporal response of the magneto-optic detector. As discussed in Section 3.1, the Faraday effect is connected to the response of materials to applied magnetic fields. Fundamentally, different reaction time scales characterize different classes of material.

In ferro/ferrimagnetic samples, the Faraday polarization rotation is almost completely determined by the magnetization and its direction relative to the Poynting light vector. Therefore, the time sensitivity of the Faraday probe is linked to the magnetization response time of some fractions of picoseconds, limited by the low-frequency magnetic excitations in this class of materials. For instance, in Chapter 7, we shall see that the reaction of a ferrimagnetic $\mathrm{Lu_2Bi_1Fe_4Ga_1O_{12}}$ sample to a much faster magnetic transient happens in hundreds of picoseconds. Similarly, the magnetization dynamics of other ferrimagnetic materials, with potential as Faraday detectors, is limited to the low-GHz regime [50, 51] or at best to ∼100 GHz [52], when the net magnetization, and therefore, the sensitivity, of the sample is strongly reduced via doping. In general, slow spin-lattice relaxation processes determine the capability of the magnetization to follow the magnetic field we want to measure via the Faraday effect [40].

The situation is similar for paramagnetic detectors, such as Terbium Gallium Garnet, $\mathrm{Cd_{1-x}Mn_xSe}$ or $\mathrm{Cd_{1-x}Mn_xTe}$ (CMT). These detectors have a lower sensitivity due to their diluted density of magnetic moments. Moreover, these magnetic ions do not interact with each other, and their response time is much shorter. For instance, CMT samples in a certain doping range are expected to show a magnetic response within $1-10\,\mathrm{ps}$ [53]. Experimental results seem to confirm a $\sim$1 ps time resolution of these detectors to applied magnetic fields [54]. However, from the data, it is unclear whether the magnetic or the electric part of the magnetic pulse used to characterize the detector was measured.

Diamagnetic detectors have the fastest response times. In particular, GaP has been suggested to have a time resolution to changes in the magnetic field as fast as 1 ps [33, 34], making it a good candidate for our experiment. Given our need to measure ultrafast magnetic transients 1.2, we cannot compromise on temporal resolution. Therefore, we chose a diamagnetic GaP sample as a detector, sacrificing magnetic field sensitivity to achieve a response time that is fast enough. The other detector types would act as a low pass filter and blur the temporal evolution of a possible magnetic field expulsion in the short-lived photo-induced superconducting state, strongly limiting the physical insight of our measurement.

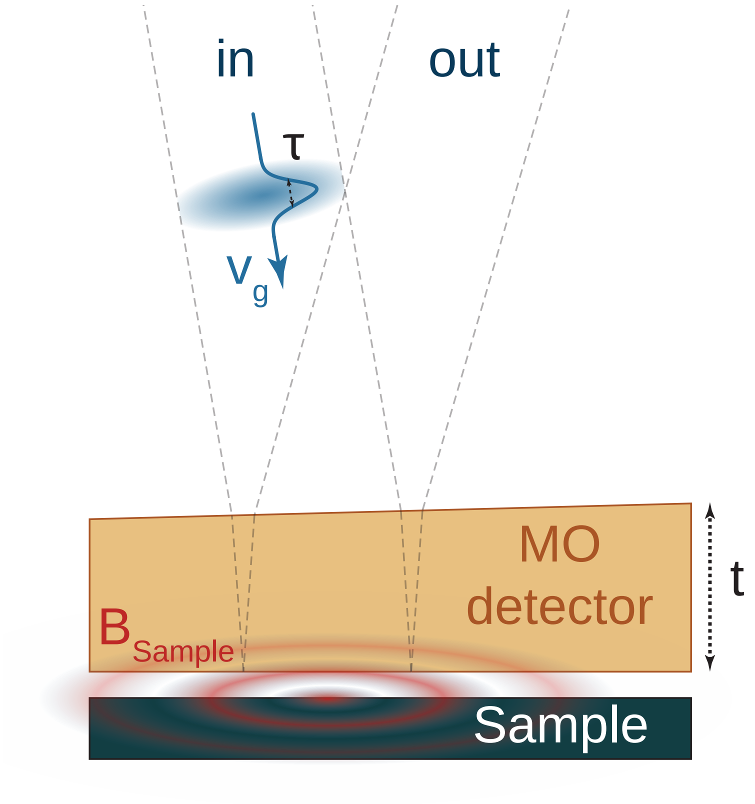

FIGURE 5.1: The figure shows the field emitted from the sample ($\mathrm{B_{Sample}}$) and the ultrafast probe pulse of duration τ traveling with velocity (v_g) and interacting in the magneto-optic (MO) detector.

Another intrinsic limitation to our technique's overall time resolution is the interaction of the probe pulse with the time-dependent magnetic signal generated by the sample inside the magneto-optic detector. Figure 5.1 schematically represents the experimental situation: a short probe pulse of duration $\tau<100\,\mathrm{fs}$ traveling at speed v_g, the group velocity of the pulse traverses the magneto-optic detector twice. A magnetic field generated by the sample (red wave in the figure) radiates into the detector. By varying the relative delay between the probe pulse and the magnetic transient produced by the sample, we can characterize the latter with a probe pulse having a much shorter duration. That is the situation we expect in our experiment, where the lifetime of the photo-excited state is set to ~1 ps by the duration of the mid-infrared pump pulse, and the probe pulse is at least an order of magnitude shorter. At negative time delays, the probe pulse reaches the back surface of the magneto-optic detector before the field radiated by the sample, and there is no interaction between the two.

Conversely, we have two contributions to the polarization rotation in this reflection geometry at positive time delays. The probe interacts with the signal during the first pass as the two *counter-propagate* in the diamagnetic detector. The interaction time in this situation is negligible, given the opposite velocities of the two, and so is the polarization rotation acquired by the probe. Then, after the probe beam is reflected, it *co-propagates* with the emitted magnetic field wave from the sample. In this case, assuming that the two propagate with the same velocity in the detector, the time resolution of the Faraday signal is given by the duration of the probe beam. However, if the propagation velocities differ, the time resolution is worsened proportionally to the mismatch between group velocity of the probe beam and phase velocity of the magnetic signal at THz frequencies: $v_{co} = v_g - V_p$[1]. Assuming a Gaussian temporal profile for the probe beam with time duration τ (we set $\sigma = \tau$ in the Gaussian function), then the effective increase of the temporal resolution of the pulse is given by:

$$\tau^2 \to \tau^2 + \left(\frac{t v_{co}}{v_g V_p}\right)^2 \tag{5.1}$$

We estimate the additional contribution inserting into the second term of the equation the parameters of our experiment: $t = 75\,\mu\text{m}$, $v_g = \frac{c}{n_g}$ with c indicating the speed of light and $n_g \approx 3.517$ [56] for 800 nm light, and $V_p = \frac{c}{n_p}$ with $n_p \approx 3.34$ [35] for radiation at 1 THz. This rough estimate shows that τ is increased by ~10 fs. Although this result suggests that the time resolution is not significantly worsened by the velocity mismatch in the detection crystal, it is still a valuable exercise to validate the time resolution of our experiment experimentally. In order to factor in all the elements discussed in this section and the uncertainties connected to them, it seems preferable to have a measurement validating the time resolution of our technique rather than relying purely on theoretical considerations. In the following sections, we discuss our experiments to achieve this goal.

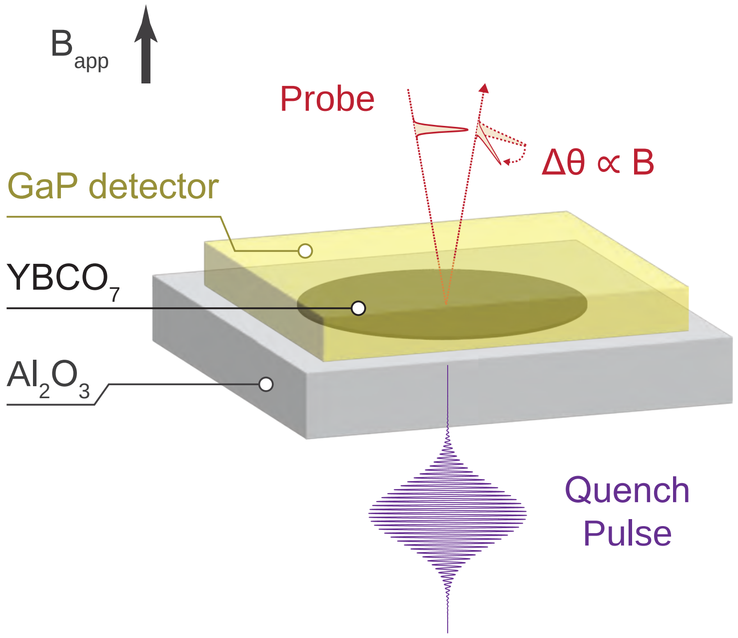

FIGURE 5.2: The figure displays the experimental configuration used to measure the ultrafast disruption of superconductivity. This is entirely analogous to the geometry used for the equilibrium measurements on thin films (see Picture 4.2), with the only addition of an optical pulse to quench superconductivity. Material from [47].

5.2 Magnetic dynamics of a quenched superconductor

Figure 5.2 outlines our approach to generate ultrafast magnetic transients to test our technique[2]. A thin $YBa_2Cu_3O_7$ film c-axis oriented and grown on a 0.5 mm thick Al_2O_3 substrate is shaped into a 1 mm diameter disk using a laser lithography process (see Appendix B for more details about the sample preparation process). The disk is kept below T_c at a temperature of 55 K in a uniform applied magnetic field of 2 mT. The polarity of the magnetic field is switched periodically between positive and negative values, as shown in Figure 3.4. The superconductor magnetizes to shield the time change of the magnetic flux through its volume (see Appendix F). The GaP detector is placed on top of the film in close contact to track the magnetic field generated by the sample and its dynamics. In this configuration, the magnetic field inside the detector is approximately equal to the one in the superconductor. The field is mostly oriented orthogonally to the sample and the detector, and the normal component of B is conserved across interfaces. An ultrafast optical pulse irradiates the sample traversing the transparent substrate to break the Cooper pairs in the superconductor [57, 58, 59, 60, 61, 62]. Consequently, the superconducting shielding currents sustaining

---

[1] In analogy to electro-optic sampling of THz pulses, since the duration of the probe beam is typically much shorter than the magnetic signal, we use the group velocity v_g for the former and the phase velocity V_p for the latter, at the respective carrier frequencies (see for example [55], Section 2.12)

[2] We will see in Chapter 7 that this idea can become useful for more than a test.

the magnetic screening are quenched, allowing the external magnetic field to penetrate inside the sample on time scales likely determined by the L/R time constant of the resistive disk (L is the total inductance of the disk and R, the resistance in the photoexcited state, see Chapter 7 for more details). The result of this experiment is shown in Figure 5.3: the probe position is set above the center of the superconducting disk, and the magnetic field change versus pump-probe time delay shows an increase from a low value to a high value as the magnetic field flux penetrates back into the sample. The optical quench chosen to disrupt superconductivity is a 400 nm center wavelength, ~100 fs duration optical pulse with a fluence of ~0.3 mJ/cm^2.

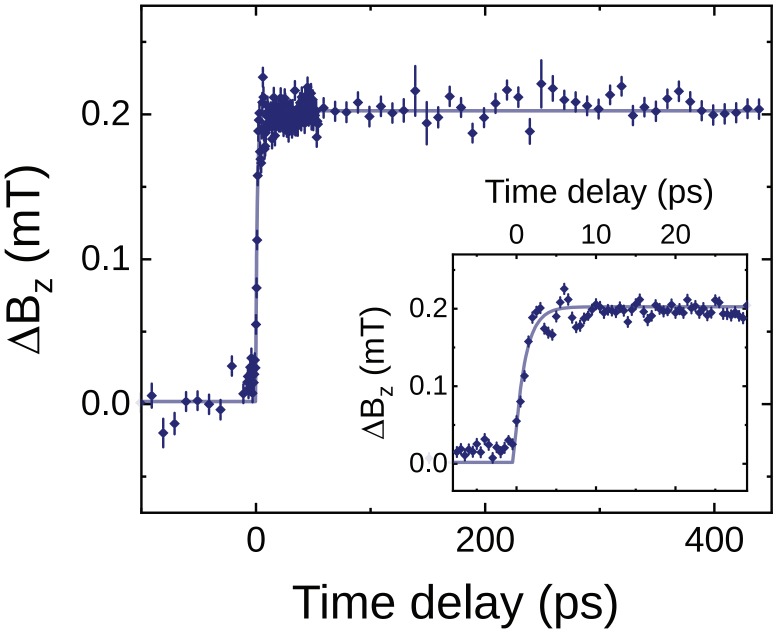

FIGURE 5.3: Ultrafast disruption of superconductivity measured with optical magnetometry. The error bars denote the standard error of the mean. Material from [47].

The dynamics measured show a fast transient that an exponential decay can fit to yield a time constant of ~1.3 ps. Therefore, this measurement confirms the sub-picosecond time resolution of our technique. Note that the resolution can be potentially faster if the physics of the phenomenon is the factor limiting the speed of the transient measured. For this experiment, we chose the thickness of the film to be comparable with the penetration depth of the optical quench pulse in the material to achieve an almost uniform excitation throughout the whole volume of the superconductor and quench superconductivity uniformly in the sample. This precaution is taken to avoid screening from deeper layers, which would completely offset the disruption of superconductivity close to the illuminated surface.

Given that the amplitude of the magnetic field change ~0.2 mT is one order of magnitude smaller than the amplitude of the applied field 2 mT, the fluence of the quench beam used for this measurement is likely not destroying the entire volume of the thin superconducting disk. However, partial shielding is still present from the deeper layers of the sample. In Chapter 7, we discuss this observation more thoroughly and show a fluence dependence of the magnetic transient versus fluence. Here, we show only the change of the magnetic field and not its absolute value. The reason is that the value of the absolute field at negative time delays varies depending on the fluence of the quench beam due to the long-lasting thermal effects induced by the quench beam. We do not discuss this issue here since it does not influence the goal of the measurement, which is validating the time resolution of our technique. We defer to Appendix G for a more detailed treatment of this topic.

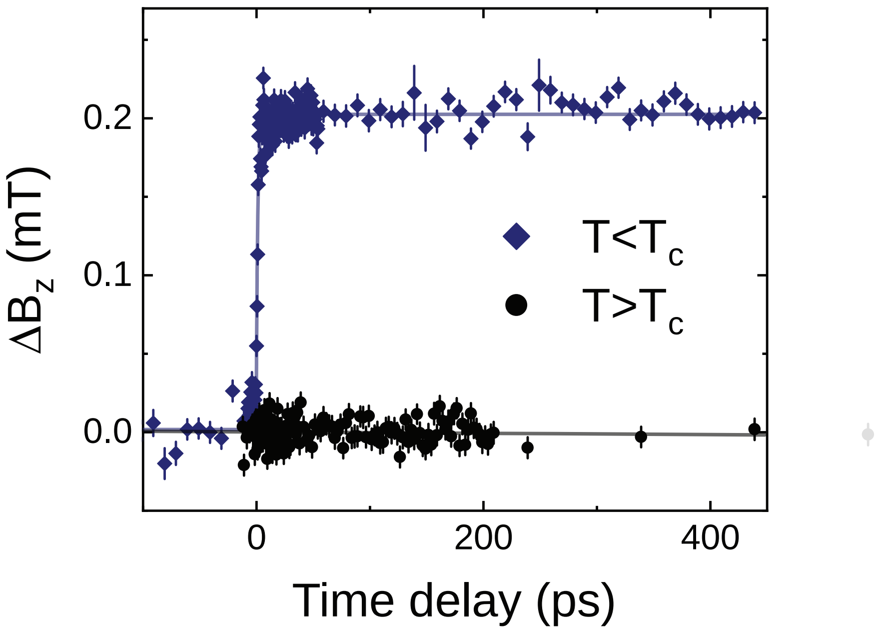

FIGURE 5.4: Test measurement showing the absence of a signal above T_c. The error bars denote the standard error of the mean. Material from [47].

Finally, we want to examine the precautions taken when performing this measurement. We opted for a configuration in which the quench beam hits the sample without propagating through the GaP detector. The sample is opaque to the pump pulse and prevents the radiation from penetrating the magneto-optic detector. Additionally, we use a *4f* imaging system to image the shadow of a disk mask matching the size of the superconducting disk onto the sample. In this way, only the region where the absorbing film is present is illuminated, not the GaP detector directly. As already outlined in Section 3.4, these preventive measures are essential to minimize the risk of possible artifacts, limiting the amount of the pump light scattered into the magnetic detector as much as possible. Moreover, we are switching the polarity of the externally applied field to get a differential signal only sensitive to magnetic contributions (see Section 3.3).

The fact that the measured magnetic field changes persist for time scales, which are much longer than the duration of the quench pulse, is reassuring and hints at the fact that the experimental expedients taken to reject noise and spurious contributions have worked. Nonetheless, to further confirm the magnetic nature of our signal and prove that the measured transient is connected to the ultrafast quench of the magnetization of the superconducting sample, we experimented with the same conditions described above, only setting the temperature to 100 K, higher than T_c. Figure 5.4 shows the result of this experiment (in black) compared to the measurement performed below T_c (in blue). The signal is absent when the sample is not superconducting and does not shield the applied magnetic field. We can, therefore, reject the hypothesis of a non-linear coupling between the pump radiation and the probe beam in the GaP detector, leading to that fast transient.

5.3 Spatio-temporal disruption of superconductivity

The fast magnetic transient shown in the previous section can change drastically depending on the probe's position relative to the sample. We demonstrated it in another experiment similar to the one described above, in which we patterned a 400 µm diameter half-disk shape out of a 150 nm-thick $YBa_2Cu_3O_7$ thin film. The superconducting sample kept below T_c, was irradiated with an optical quench beam to destroy superconductivity with the repetition rate shown in Figure 5.5. The goal of this experiment is to mimic as closely as possible a situation precisely opposite to the one expected when driving with mid-infrared light $YBa_2Cu_3O_{6.48}$ above T_c: the shape of the thin film reproduces the shape of the mid-infrared pump pulse, and we apply a similar doubly differential pump-probe scheme by switching the applied field and chopping the pump as done in the measurement performed above T_c (Chapter 6). The difference is that, in the first experiment, we disrupt equilibrium superconducting *shielding* (see Appendix G for more details about this measurement). In the second case, we optically induce a transient superconductor which should *expel* the applied field only during its lifetime. Nonetheless, this is the perfect setting to test the capabilities of our technique and check which superconducting transient we should expect when measuring in different positions relative to the photo-excited sample, above or below T_c.

The upper panel of Figure 5.5 summarizes the measurement details described above. A magnetostatic simulation shows the spatially dependent z component of the magnetic field generated at equilibrium by the $YBa_2Cu_3O_7$ thin film. At the edge, we see an enhancement of the magnetic field while on top of the center of the sample, a reduction. The lower panel displays the magnetic dynamics measured with GaP above the edge and the film's center upon disrupting superconductivity. When measuring above the center, we see an evolution analogous to the one displayed in Figure 5.3.

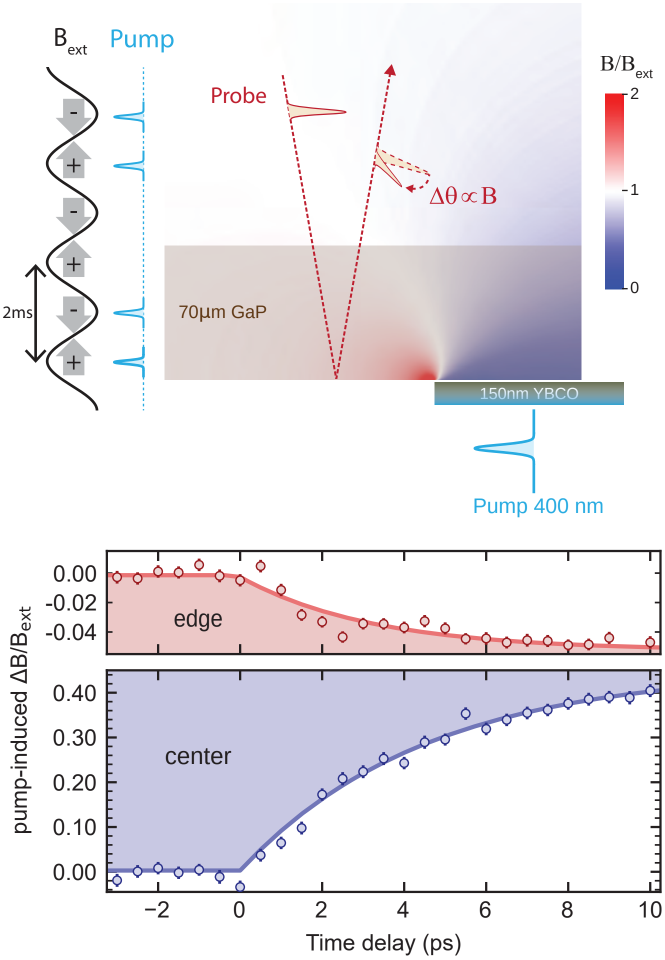

FIGURE 5.5: Disruption of superconductivity above the edge and center of an optimally doped $YBa_2Cu_3O_7$ thin film. The error bars denote the standard error of the mean. Material from [17].

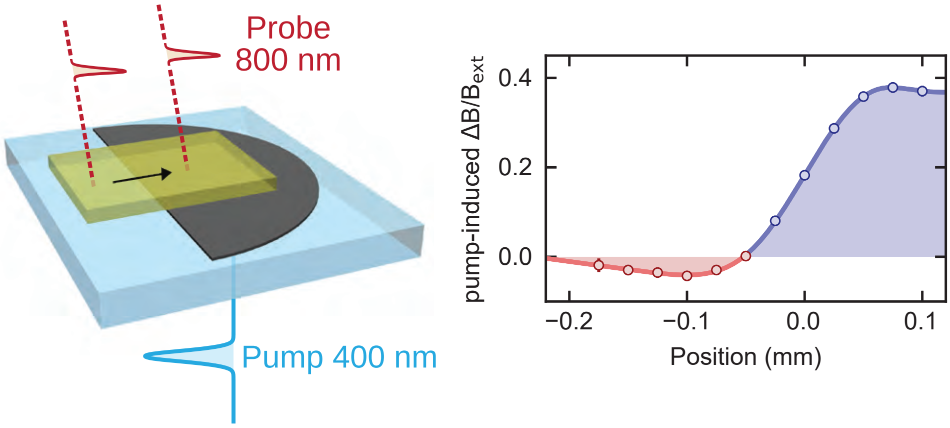

FIGURE 5.6: Spatio-temporal disruption of superconductivity in an optimally doped $YBa_2Cu_3O_7$ thin film. The error bars denote the standard error of the mean. Material from [17].

Conversely, when measuring above the half-disk's edge, the magnetic field's transient change possesses an opposite sign. The reason for this is that the higher density of magnetic field lines, which accumulate at the edges of the sample at equilibrium, relaxes when the shielding currents are quenched. Analogously, we expect to measure a transient increase of the magnetic field amplitude at the edge of the photo-excited region above T_c if the driven state expels a magnetic field from its volume.

Finally, we show in Figure 5.6 the difference between the magnetic field measured at 10 ps positive time delays and at negative delays as a function of the distance from the straight edge of the half-disk. This map highlights the spatially dependent sign change of the differential signal at a position slightly shifted from the edge of the film due to the averaging effect of the thick GaP detector. It also conveys valuable information for the experiment presented in the next chapter by defining a range for the spatial extent of the region in which we expect a magnetic field enhancement from the edge of the photo-excited region.

To summarize, with this set of measurements, we demonstrated that the spatio-temporal resolution of the technique is enough to measure magnetic transients generated by photo-excited superconductors. This is a promising starting point for searching for a Meissner-like magnetic field expulsion in driven $YBa_2Cu_3O_{6.48}$.

Chapter 6

Magnetic field expulsion in optically driven $YBa_2Cu_3O_{6.48}$

This chapter presents the most important experimental results shown in this thesis. The measurements discussed below characterize the magnetic response of a driven superconductor for the first time and its dependence on external parameters. For this experiment, we keep the material above T_c in its normal state and replicate the driving conditions, which lead to transient THz optical features suggestive of light-induced superconducting-like transport.

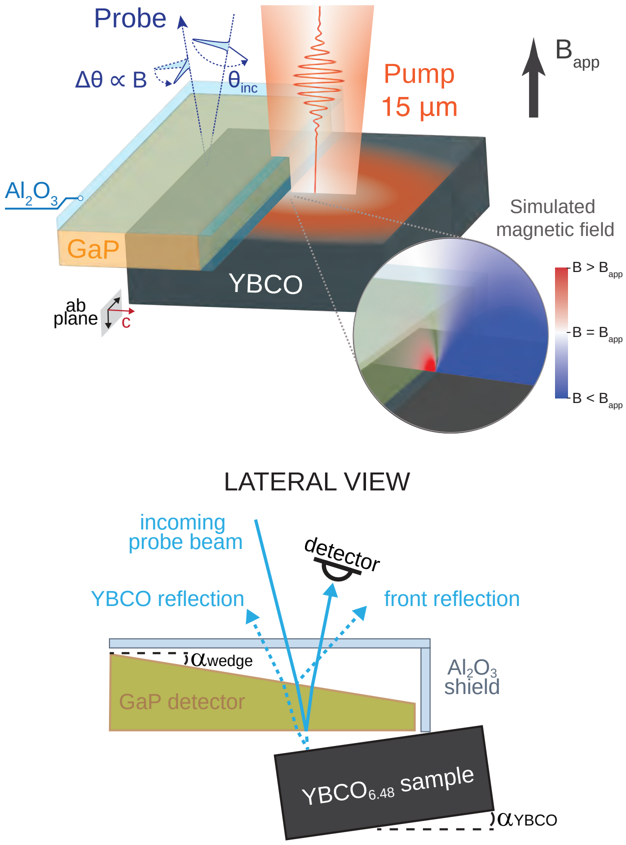

FIGURE 6.1: Experimental geometry for measuring magnetic expulsion in driven $YBa_2Cu_3O_{6.48}$. Adapted from [17].

Therefore, we use a 1 ps-long, 15 µm wavelength pump pulse, polarized along the c-axis of the sample and resonant with the apical-oxygen phonon modes responsible for the transient superconducting-like state [12]. The $YBa_2Cu_3O_{6.48}$ sample was prepared for the measurement as shown in Figure 6.1. This is the same configuration used for the equilibrium characterization measurements discussed in Section 4.3. The main reason for such a configuration is that, as of today, it is not possible to grow untwinned $YBa_2Cu_3O_{7-\delta}$ thin films exposing the c-axis, which in our experiments needs to be optically accessible. The thickness of the bulk sample used instead is ∼2 mm, much bigger than the spatial extension of the measurable magnetic field change generated by the photo-excited superconductor, even considering an optimistic scenario in which the magnetic field expulsion of the light-induced state is assumed to be as strong as the equilibrium shielding of the thin film discussed in Chapter 4. Therefore, a configuration like the one used in Chapter 5 to avoid pump-probe artifacts, where the probing crystal is placed on the side of the sample opposite to the incoming pump pulse like in Figure 6.2, is impossible.

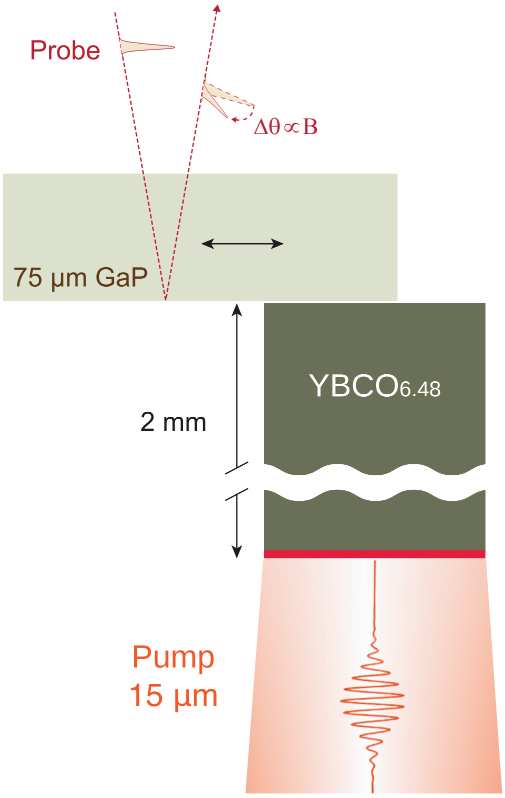

FIGURE 6.2: Possible setup for measuring expulsion in driven $YBa_2Cu_3O_{6.48}$. This solution is not viable given the great distance between the photo-excited region (thin domain in red) and the magneto-optic detector that would further reduce the size of the signal.

Another more creative approach can be envisioned to maintain spatially close the photo-excited region and the magneto-optic detector, at the price of a more complicated sample preparation process[1]. The pump and the probe beam come at a different angle from the same side of the sample. One edge of the magneto-optic detector is placed in the center of the pump beam, the top and the side covered with a thin (30 µm) slab of sapphire (see Figure 6.1). The 15 µm pump, falling in the Reststrahlen band of sapphire, is completely reflected by the shield and creates a half-disk-shaped photo-excited region on the $YBa_2Cu_3O_{6.48}$ surface, with a sharp edge close to the GaP detector. Conversely, the 800 nm probe can propagate to the magneto-optic detector unaffected by the shield. An additional level of complexity associated with this sample preparation procedure is that there needs to be a well-defined angle between the sample and the detector to avoid collecting reflections coming directly from the sample that could induce some additional birefringence due to its anisotropic crystalline structure (see the lower panel of Figure 6.1).

The most direct consequence of this experimental configuration is that it does not allow measuring directly on top of the sample's pumped region but only on its side. Therefore, a magnetic field exclusion from the photo-excited area of the sample will manifest itself as an increase in the magnetic flux at its edge. This concept is displayed in the inset of Figure 6.1), which shows a static simulation of the z-component of the magnetic field at the edge of a diamagnetic domain having the same dimensions of the photo-excited region: the red color indicates an increase of the magnetic field compared to the applied field at the position of the GaP detector. The sapphire shield creates a sharp edge for the pumped region, which strongly increases the magnetic field enhancement compared to the gradual edge given by a Gaussian pump beam profile.

The results of this measurement at the "edge" are presented in Figure 6.3. The left panel shows an increased magnetic field for ∼1 ps, measured 50 µm away from the photo-excited region with an externally applied field of 10 mT. The state lacks intrinsic rigidity since its duration approximately coincides with that of the pump pulse (shown above the pump-probe traces), in analogy to what was reported in previous THz reflectivity measurements (see, for instance, [9]). The inset on the left side of the figure shows the peak of the pump-probe response measured at different angles of the probe beam's polarization θ_{inc} (see Figure 6.1 for reference). The signal does not depend on this variable. This result strongly indicates the magnetic origin of the signal measured since this is the symmetry expected for the Faraday effect. For instance, if the origin of the polarization rotation were an electric field via the Pockels effect, the signal would have shown a four-lobed dependence on the incident polarization angle [17]. The magnetic field expulsion is observed up to 300 K with reduced amplitude, similar to what is reported in THz reflectivity measurements. The right side of Figure 6.3 shows the results of a magnetostatic simulation that we performed to understand the meaning of the measured signal better. Even though the phenomenon discussed here is intrinsically dynamic, a static simulation can be useful as a zeroth-order approach to gain some physical insight. We associated a

---

[1] Nothing that the precise hands of a careful experimentalist like Dr. Fava could not brilliantly solve.

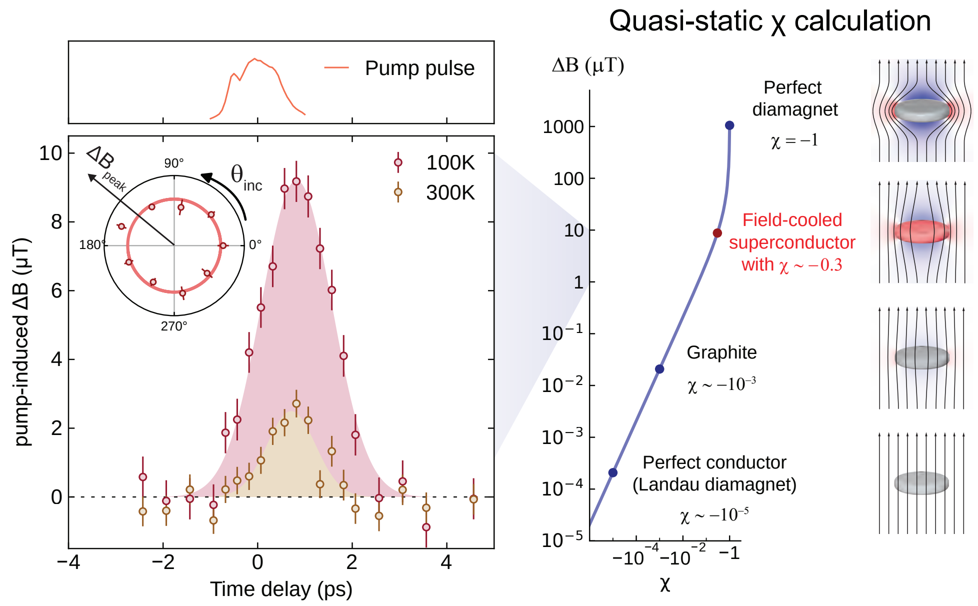

FIGURE 6.3: The figure shows a transient enhancement of the magnetic field close to the edge of the sample, compatible with a magnetic field expulsion from the photo-excited $YBa_2Cu_3O_{6.48}$ region. The time profile of the pump pulse is obtained by measuring the cross-correlation of the pump and probe due to the non-linear Kerr effect in a portion of GaP not shielded by sapphire. The error bars denote the standard error of the mean. Material from [17].

uniform diamagnetic susceptibility to a volume with the same dimensions of the sample region photo-excited by the mid-infrared pump and calculated the magnetic field increase at the edge of this diamagnetic domain, spatially averaged to take into account the finite size of the magneto-optic crystal traversed by the probe beam. A diamagnetic susceptibility of 0.3 is required to achieve the enhancement of ∼10 µT measured at the peak of the 100 K pump-probe response. Such a value is orders of magnitude higher than the typical diamagnetic susceptibilities of standard metals. For instance, the diamagnetic susceptibility of graphite, the metallic material with the highest equilibrium diamagnetic response known, is only $\sim 10^{-3}$. The diamagnetic properties of the driven $YBa_2Cu_3O_{6.48}$ sample are similar to those of field-cooled type II superconductors in their mixed state (see Section 2.7). This outcome proves that this transient state is *qualitatively* different from a mere metallic state with enhanced mobility, lifting the ambiguity left by the THz reflectivity data.

Another source of debate in the interpretation of THz reflectivity measurements is how to estimate the thickness of the transient superconducting region and the impact of this assumption on the superconducting nature of this state [13, 63]. Figure 6.4 addresses this issue by showing the calculated magnetic enhancement versus diamagnetic susceptibility curves for three different thicknesses of the photo-excited region. In all the three cases shown, corresponding to different assumptions in the model used to calculate the thickness of the light-induced superconducting region (see

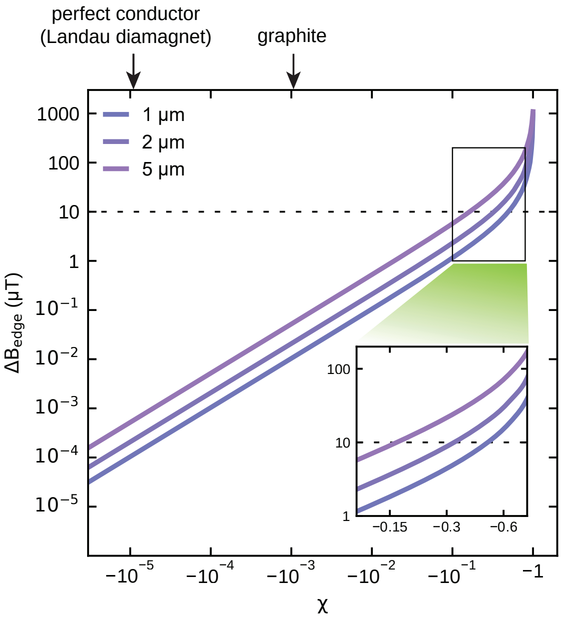

FIGURE 6.4: Simulated magnetic field enhancement versus thickness of the transient superconducting region. The simulation with thickness 2 µm is the one shown in Figure 6.3. Material from [17].

reference [17] for more details), the diamagnetic response necessary to fit the measured magnetic signal is not compatible with that of a metal.

6.1 Dynamical magnetic field propagation

The transient magnetic field expulsion in driven $YBa_2Cu_3O_{6.48}$ is dynamic in nature. In this section, we discuss some experimental results that characterize the dynamics of this state.

We can imagine that the pump causes a sudden change in the diamagnetic susceptibility of the sample, which magnetizes in the uniform externally applied field [17]. This sudden magnetization represents a source term in Maxwell's equation (finite $\partial \mathbf{B}/\partial t$ in Faraday's law) and produces the emission of a wave. The duration of the pump producing this magnetic state is 1 ps, so we would expect the emitted wave to have significant spectral weight at ~1 THz. In this picture, the pump-probe data shown in Figure 6.3 is due to this emitted wave measured at a specific distance from the edge of the photo-excited region.

Figure 6.5 shows a detailed characterization of the propagating magnetic wave launched by the sample. The middle panel of the figure shows pump-probe traces measured at different distances of the probe beam from the magneto-optic detector's edge (50 µm, 110 µm and 170 µm respectively from top to bottom). It is evident that the peak of the magnetic response is delayed in time and reduced in amplitude as the distance increases. The right panel of the figure shows the arrival time of the peak of

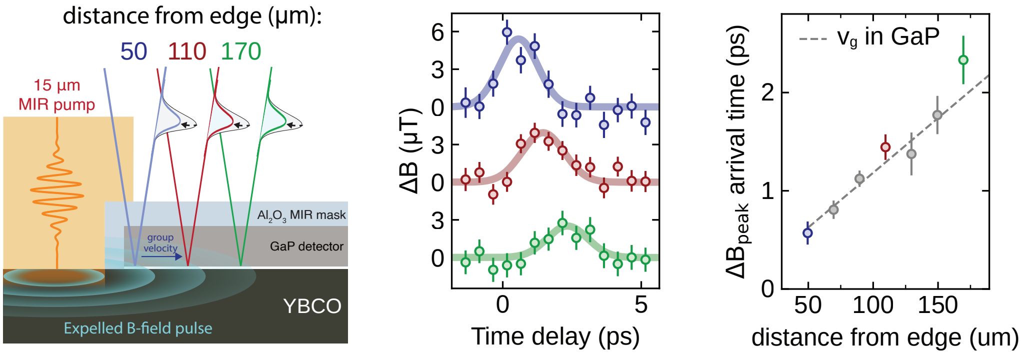

FIGURE 6.5: Characterization of the propagation of the transient magnetic field expulsion by changing the probe's distance from the edge of the magneto-optic detector. The error bars denote the standard error of the mean. Material from [17].

the pump-probe response versus the distance from the edge. From this last dataset, we can extract the propagation speed of the magnetic expulsion signal in the magnetic detector, which closely matches the group velocity of light at 1 THz in GaP (grey dashed line).

The unipolar pump-probe response measured might, at first sight, appear difficult to reconcile with the propagating wave picture given above. An important detail to remember that could explain this contradiction is that we are measuring deep in the near-field regime. The wavelength of a 1 THz wave in GaP is ∼100 µm [35]. In our experiments, we measure at a distance below this limit, and the requirement of propagating waves being bipolar, strictly true in the far field, breaks down [64].

6.2 Parameter dependencies

To further characterize this photo-excited state's properties, we systematically varied the most important experimental parameters. Figure 6.6 summarizes the dependence of the peak of the pump-probe magnetic response versus temperature, externally applied magnetic field, and fluence of the pump pulse.

The temperature dependence of the magnetic signal in the range between 100 K and 300 K (red data points in the left panel) matches that extracted from THz reflectivity data (dashed blue line). In both cases, the signal diminishes as the temperature increases in a way that appears connected to a pseudogap regime above T_c. Moreover, their similar temperature scaling convincingly confirms that these two experiments are characterizing, with different observables, the *same* physical phenomenon induced by resonant phonon driving. The figure's central panel shows the effect's dependence on the externally applied magnetic field. Curiously, the signal scales linearly with the applied field up to the highest magnetic field applied of 12.5 mT, and we do not see any non-linearity. This is unexpected if we compare this data with the equilibrium measurements done on the same sample, which show clear features of a first critical

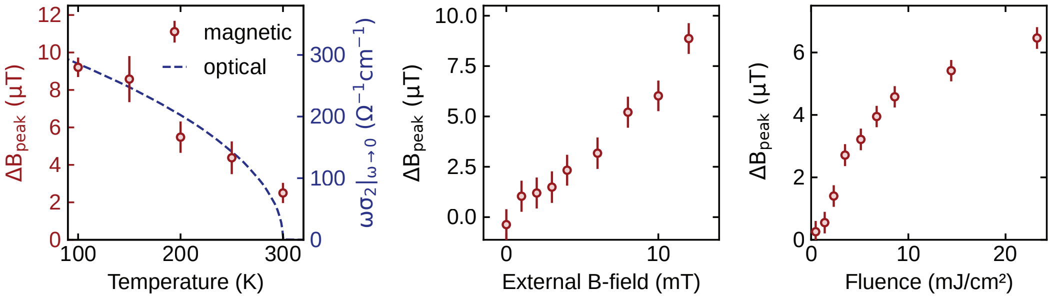

FIGURE 6.6: Parameter dependence of the peak of the transient magnetic field expulsion response. The optical data (dashed blue line in the left panel) is taken from [12]. The error bars denote the standard error of the mean. Material from [17].

field already at $\sim$2 mT (see Figure 4.9). This observation entails that the drive does not simply generate a state equivalent to an equilibrium superconductor for the duration of the pump pulse. Conversely, this measurement suggests that the pump produces a transient state in YBa$_2$Cu$_3$O$_{6.48}$ characterized by a greater stiffness than its equilibrium counterpart, in agreement with the observation that light-induced superconductivity persists up to room-temperature. Importantly, we also want to point out that the magnetic enhancement is zero when no external field is applied. This observation further corroborates the magnetic nature of the measured signal. It also excludes the hypothesis of trivial non-linear coupling between the pump and probe as the origin of the effect. We then varied the fluence of the 1 ps, 15 µm mid-infrared pump pulse from the optimal value of $\sim$14 mJ/cm^{-2} used for all the other measurements. The right panel shows the results of this experiment, in which the sample was kept at 100 K with an externally applied field of 10 mT. The measured curve appears to scale sub-linearly with the fluence of the incident pump pulse, indicating that either the effect does not scale linearly with the amplitude of the driven phonon or that the phonon amplitude deviates from the linear behavior at high fluences. Moreover, the sublinear dependence of the effect with pump intensity rules out a pump-induced electro-optic Kerr effect as the origin of the signal (which should be linear with pump intensity) and possibly suggests a saturation regime of the effect.

Finally, figure 6.7 shows the measured signal when the position of the pump and probe was scanned across the sample edge (position 0.0 mm in the right panel), keeping the relative distance between pump and probe unchanged. For this experiment, the base temperature was 100 K and the applied field 10 mT. It is evident that the magnetic signal disappears as the pump and probe move past the edge of the sample, further excluding the possibility of a cross-talk between the pump and the probe in the magneto-optic detector.

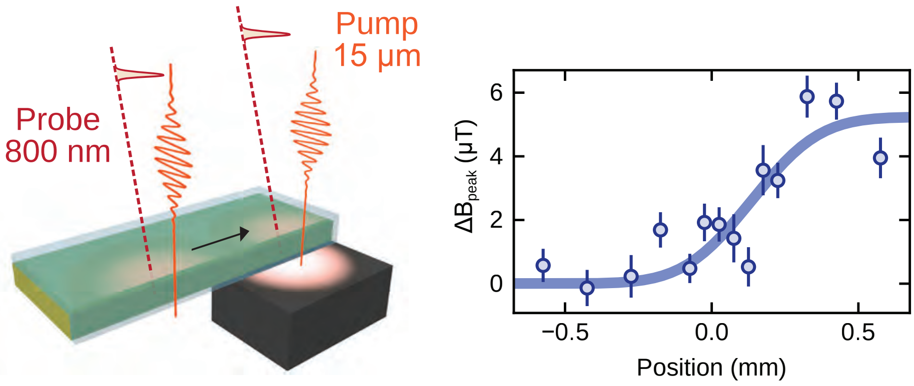

FIGURE 6.7: Spatial dependence of the peak of the transient magnetic field expulsion response. The error bars denote the standard error of the mean. Material from [17].

6.3 Discussion

In the previous part of the chapter, we already discussed a possible picture describing the observed magnetic response, assuming the pumped region acquires a diamagnetic susceptibility of ~ -0.3. This explanation implies the presence of a transient superconducting phase induced by the pump. Another alternative model compatible with our results presumes the presence of pre-existing diamagnetic currents in the pseudogap phase [17]. The role of the drive is to synchronize and amplify those diamagnetic currents, similarly to the amplification mechanism discussed in reference [65] for Josephson plasma polaritons. This second point of view involves the presence of pre-formed Cooper pairs and local superconducting coherence at equilibrium above T_c.

Both these scenarios hint at some form of light-induced superconductivity. The first suggests a quench into a true superconducting state. The second implies a dynamical form of synchronization following the optical drive, which is evocative of Floquet physics. Both these scenarios, which are not substantiated by a rigorous theoretical treatment, underscore the highly unconventional nature of this phenomenon and the role of the coherent electromagnetic field in engineering new exotic out-of-equilibrium phases without an obvious equilibrium counterpart.

Furthermore, this class of experiments offers the unique opportunity to follow the non-thermal dynamics of the Meissner effect [66]. The ultrafast quench into the Meissner state induced by the pump allows us to study its formation beyond thermodynamics and to track the intrinsic time scales needed for the Meissner effect to set in. Further variations of the experiment described here might be beneficial to deepen our understanding of this stimulating effect.

Chapter 7

Ultrafast magnetic steps for coherent control[1]

In Chapter 5 we discussed the dynamics ensuing optical disruption of magnetic shielding in an equilibrium superconductor. Figure 5.3 (reported again in this chapter for convenience as Figure 7.1) showed a sudden unipolar magnetic field change happening in picosecond time scales having an ultrafast step-like temporal evolution. Ultrafast magnetic field steps are unipolar, time-varying magnetic field pulses with short rise times and long decay times. This transient type possesses peculiar characteristics that could make it a useful tool for controlling and investigating material properties. In this chapter, we review potential applications of magnetic steps, study their characteristics, and demonstrate their properties with a test experiment. We then conclude by discussing further improvements and areas of relevance for this technique.

7.1 Why are ultrafast magnetic steps useful?

As discussed in Section 1.3, a step-like magnetic transient is a valuable tool for studying the conductivity of equilibrium and transient states of superconductors and metallic systems in general. Biasing such systems with a strong unipolar $\partial \mathbf{B}/\partial t$ would launch shielding currents in the sample as prescribed by Faraday's law. Studying the decay time of these currents by measuring the magnetic field they generate yields important information about the characteristics of electric transport in the systems studied.

Another area where the kind of excitation discussed here might be appealing is ultrafast magnetism. A long-standing challenge in ultrafast magnetism and in functional materials research, in general, has been the generation of a universal, ultrafast stimulus able to switch between stable magnetic states [67, 68, 69, 70, 71, 72]. Solving this problem would open up many new opportunities for fundamental studies, potentially impacting future data storage technologies. Ideally, step-like magnetic field transients with infinitely fast rise time would serve this purpose. Of particular interest for magnetic storage technologies is the possibility of controlling the magnetic order in antiferromagnetic materials due to their high-frequency response and robustness

---

[1] Parts of this chapter have been taken verbatim or adapted from the Main Text and Supplementary Information of the related publication [47]

to external perturbations. Some theoretical proposals show how fast time variations of an external magnetic field are an effective driving force for the order parameter of these materials [73]. Ultrafast magnetic field steps with a fast enough rise time and with a sufficiently big amplitude could be a promising tool to toggle the state of an antiferromagnet and, more straightforwardly, the magnetization of a ferromagnet between stable bit states.

The ultrafast magnetic field steps we can generate, based on an ultrafast quench of the supercurrents in a superconductor, have millitesla amplitude, picosecond rise times, and slew rates of hundreds of MT/s. For comparison, micro coils have been used to generate magnetic field steps having amplitudes of tens of mT and rise times of hundreds of ps or longer [74, 75, 76]. While the amplitude of these transients is remarkable and suitable to an extensive range of use cases, their low speed limits their applicability to a wide range of problems.

Auston switches can generate faster steps and are used to produce magnetic pulses with picosecond rise times [77, 78]. However, these generated magnetic field transients have an amplitude limited by Joule heating in the resistive coplanar waveguides carrying the pulse, and their spatial profile is generally confined to micron-sized regions (tens of μm) with strong spatial gradients. Moreover, they are characterized by sub-nanosecond decay times, which limit the low-frequency content of the magnetic excitation. In fact, in realizations of magnetic field steps, based on Auston switches or free space THz pulses, the low-frequency cutoff is generally limited to tens [77, 78, 79] and hundreds [80, 51, 81, 82, 52, 83] of GHz respectively.

Our new approach can potentially overcome the shortcomings of the methods discussed above, generating magnetic field steps that retain the fastest rise times, long decay times, and sizeable amplitudes while offering new opportunities for tailoring spatial and temporal profiles of the induced magnetic fields. By reducing the lateral dimensions of the thin superconductor used for the device, we can achieve faster transients (see the simulation in Section 7.2.3) and higher amplitudes of the generated step at the price of a less uniform spatial distribution of the magnetic field. Conversely, a larger device would yield a more uniformly spread magnetic field profile in space. Another key feature of our technique is the possibility of patterning an arbitrary geometry in the $YBa_2Cu_3O_7$ thin film. This capability could generate magnetic transients with arbitrary spatial and temporal magnetic field profiles. For instance, a horse-shoe-shaped device might behave similarly to a split ring resonator. Finally, the lowest frequency achievable with our technique is well below 1 GHz, limited only by the time dependence of the externally applied magnetic field (see Appendix G for more information). Such a broad spectral content makes these magnetic field steps a valuable tool for investigating materials' conductivity and magnetic properties from DC to THz frequency (see Section 7.4 for more details).

7.2 Properties of the ultrafast magnetic steps

As elaborated in Chapter 5, the physical principle that enables the generation of magnetic steps with picosecond rise times and “on” times far over a nanosecond (and potentially all the way to milliseconds) is based on a superconducting material with large diamagnetism, quenched with an ultrafast optical pulse. In a zero-field cooled superconductor, the application of a magnetic field generates persistent currents [7, 84] to exclude the magnetic flux from the sample volume. Sub-picosecond optical pulses are used to disrupt superconductivity [57, 58, 59, 60, 61, 62], and a sudden change in the magnetic field surrounding the material generates near field, ultrafast magnetic steps. These pulses are extremely broadband, with frequency content spanning several octaves, from sub-GHz to THz frequencies.

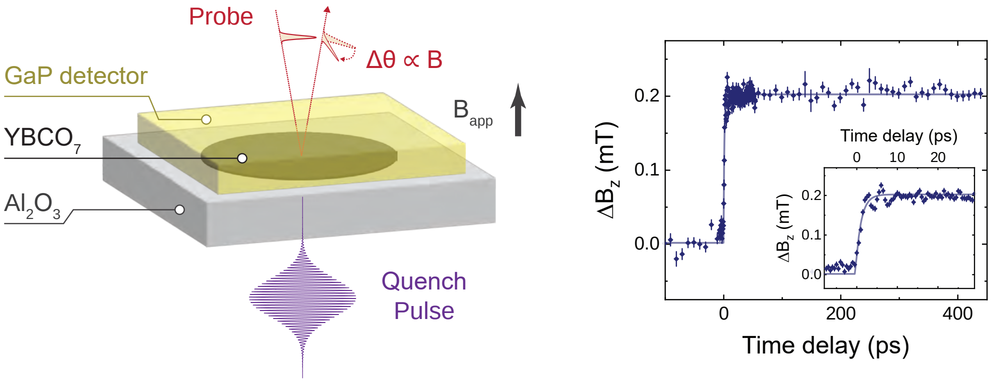

FIGURE 7.1: Experimental configuration for generating a magnetic step and relative experimental results. The error bars denote the standard error of the mean. Material from [47].

Figure 7.1 recalls the experimental geometry and the data already shown in Section 5.2 displaying the thin film of optimally doped $YBa_2Cu_3O_7$, cooled below T_c at 55 K and excited with a 100 fs long, 400 nm wavelength optical quench pulse, which disrupts superconductivity. The evolution of the magnetic field surrounding the superconductor after optical excitation is tracked exploiting the Faraday effect in a diamagnetic GaP (100) crystal ∼70 µm thick, placed above the superconductor, probed with a 800 nm time delayed optical pulse with ∼50 µm FWHM.

The measurement shown in the right panel of Figure 7.1 displays the time dependence of the changes in the local magnetic field induced by the quench pulse and measured above the center of the $YBa_2Cu_3O_7$ film. As shown in Figure 4.3, the $YBa_2Cu_3O_7$ shields the applied magnetic field effectively at this temperature. As the quench pulse hits the sample, an increase in the magnetic field is detected. This produced an ultrafast magnetic field step of ∼0.2 mT amplitude with a rise time of ∼1 ps (see the inset of the figure and the fitting procedure described in Subsection 7.2.2), corresponding to a slew rate of $\sim 200\,\mathrm{MTs}^{-1}$.

7.2.1 Fluence dependence

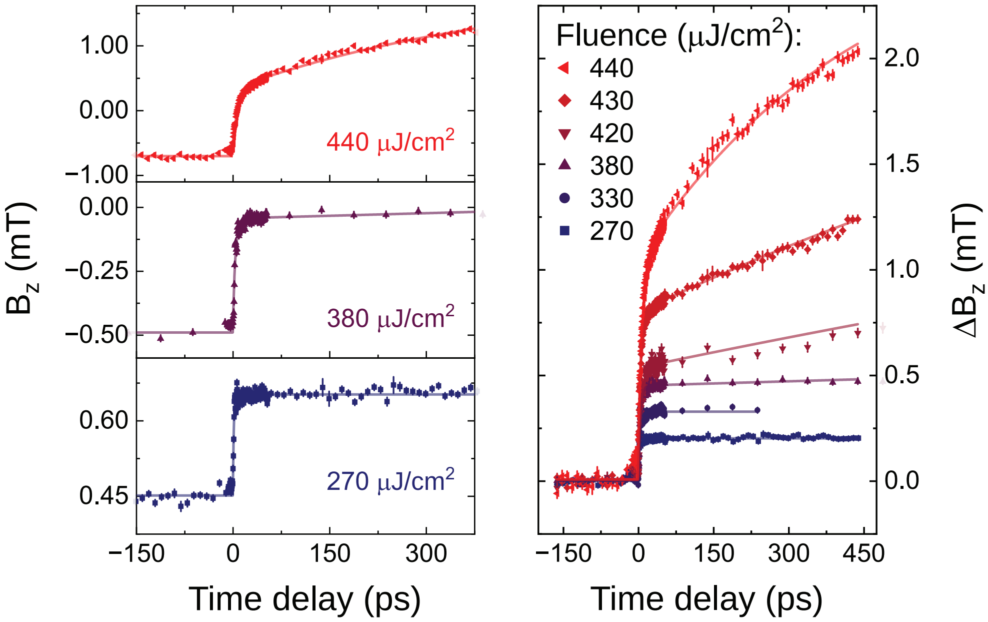

FIGURE 7.2: Experimental data showing the measured magnetic field for three selected fluences of the quench beam (left panel) and the changes of the magnetic field for six different quench fluences (right panel) versus pump-probe delay. These data have been measured using a GaP magneto-optic detector. The error bars denote the standard error of the mean. Material from [47].

Figure 7.2 shows the measured magnetic steps for different incident quench beam fluence values. The curve measured at the lowest fluence (270 µJcm^{-2}) is the same as shown in the right panel of Figure 7.1. As we progressively increase the fluence of the optical quench pulse, the amplitude of the ultrafast magnetic step also increases. At a fluence of 400 µJcm^{-2}, the step suddenly changes its behavior, and an additional, slower time scale appears. The curves taken at higher fluence show the presence of trapped flux with opposite polarity at negative time delays. This is visible in the negative pump-probe time delay region of the first two graphs in the left-hand-side panel of the figure, plotting the z-component of the *absolute* value of the magnetic field measured at a fluence of 440 µJcm^{-2} and 380 µJcm^{-2}. We think the reason for this fluence-dependent magnetic field value at negative time delays is a slow thermal dynamic of the device that determines the amount of magnetic flux trapped in the sample before the optical pump disrupts superconductivity. These dynamics happen on time scales of hundreds of microseconds in our measurement protocol and do not seem to influence the fast transient of the magnetic field step. We give a possible explanation of this phenomenon in Appendix G.

7.2.2 Modeling the ultrafast magnetic steps

To gain deeper insight into these ultrafast magnetic field steps, we assumed that the essential physics of this phenomenon is captured by a simple circuit model characterized by an inductor (with inductance L) and a resistor (with resistance R). The data shown in the right panel of Figure 7.1 is well-fitted by the single exponential decay function reported below, which represents the typical response to a voltage step of an L/R circuit:

$$y(t) = \begin{cases} y_0 & t < t_0 \\ y_0 + A\left(1 - e^{-\frac{t-t_0}{\tau}}\right) & t \geq t_0 \end{cases} . \tag{7.1}$$

In this formula, t is the independent variable representing the time delay, y_0 is the baseline at negative time delays accounting for the magnetic flux trapped at $t < t_0$, A is the amplitude of the magnetic step, t_0 is the arrival time of the quench beam and τ is the characteristic rise time of the magnetic step. The pump-probe differential change ΔB_z shown in Figures 7.2 and 7.1 is achieved by subtracting the fitted value of y_0 from the measured magnetic field. By fitting the data in Figure 7.1, we extract a value $\tau{\sim}1.3\,\mathrm{ps}$. The inverse of this value can be seen as a proxy of the high-frequency cutoff of the spectral content in our magnetic steps (see Section 7.4). In this equivalent circuit picture, the quench pulse creates a sudden increase in the resistivity of the superconducting disk, which causes a reduction of its shielding currents on time scales dictated by the inductance and resistance of the suddenly produced photo-excited state. We proceed by estimating the L/R time constant of our device to more quantitatively validate this simple circuit model. We used *COMSOL Multiphysics®* to extract the resistance and the inductance of a thin disk with a conductivity of $1\,\mathrm{MSm^{-1}}$, a value similar to the normal state in-plane conductivity of optimally doped $YBa_2Cu_3O_{7-\delta}$ at 100 K [85]. We account for the current mainly flowing at the edges of the disk [48] by modeling our sample as a ring with an internal radius equal to 70% of the external radius and biasing it with a uniform current distribution to extract L and R.

Figure 7.3 shows the linear dependence of the system's time constant $\tau = L/R$ as a function of the external radius r of the ring. When r is set to 500 µm to match the size of the superconducting disk in our experiment, the time constant extracted is 9.2 ps. This value is roughly 7 times bigger than what was measured in the experiment (~1.3 ps). The dynamics of the process would be well described by this equivalent L-R circuit when assuming a conductivity of the excited state of $0.1\,\mathrm{MSm^{-1}}$. Albeit lower than the *equilibrium* normal state conductivity of $YBa_2Cu_3O_7$ [85, 86] such value can still be compatible with the conductivity of the photo-excited state. Notwithstanding its incompleteness, our toy model seems to capture the main features of the physical phenomenon we are measuring. Being so simple, it can easily be used to make zero-order predictions about the parameter dependencies of this effect. For instance, Figure 7.3 highlights the linear dependence between the time constant and the radius of the device, hinting at reducing the diameter of the superconducting disk as a possible path

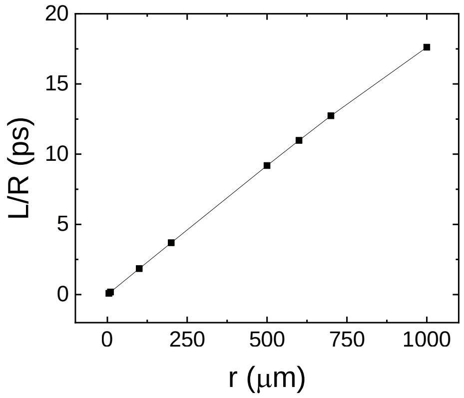

FIGURE 7.3: The simulated time constant (L/R) of a resistive ring with conductivity 1 MSm^{-1}, thickness 150 nm, and ratio internal to external radius fixed to 0.7 versus the size of the external radius (r). Material from [47].

forward to achieve faster switching times. A better estimate of the value used for the conductivity of the photo-excited state and a more accurate current distribution in the sample (beyond the uniform current density that we used for these simulations) could resolve the discrepancy between experiment and simulations, bringing the results of this model closer to the measured signal.

7.2.3 Simulating the dynamics of the ultrafast magnetic steps

To further understand the magnetic dynamics of the magnetic step, we performed a time-dependent finite element calculation using *COMSOL Multiphysics®*. The superconducting $YBa_2Cu_3O_7$ sample was modeled as a disk with a radius of 5 µm and a thickness of 150 nm, characterized by a high conductivity (10^{11} Sm^{-1}). We had to simulate a sample with a smaller lateral dimension than the one in our experiment due to the high computational cost of the 3D simulation configured. Zero-field-cooled magnetic shielding was modeled by ramping up a uniform applied magnetic field from 0 to 1 mT in 1 ns along the z direction, perpendicular to the plane of the disk. We mimicked the effect of the optical pump by quenching the conductivity of the thin disk to 10^6 Sm^{-1}, which is the conductivity of the sample in the normal state at 100 K [85]. This assumption is analogous to stating that the pump pulse turns all the superconducting carriers into normal carriers.

Figure 7.4 shows the results we achieved. The left panel of the figure displays the equilibrium distribution of the magnetic field before the conductivity quench. The calculated result is similar to what reported in the left panel of Figure 4.4, with the difference that the simulated spatial features are sharper because we are not taking into account the loss of resolution due to the integration across the thickness of the GaP detector. The right panel shows the dynamics of the magnetic field in the center of the disc after the conductivity quench. The shielding disappears on ultrafast time

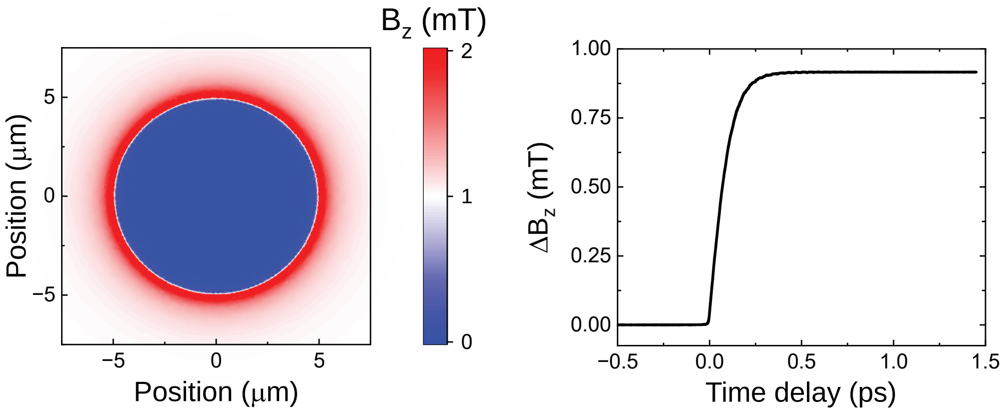

Figure 7.4: The left panel shows the simulated z-component of the magnetic field (B_z) above the center of the superconductor at negative time delays. The right panel shows the calculated change of B_z in time after the conductivity quench. Material from [47].

scale: after ~0.3 ps the magnetic field reaches the value of the external magnetic field. Like the experimental data, this curve can be fitted by a single exponential decay in time (see Equation 7.1). This fit yields a time constant $\tau \sim 0.08$ ps, which is in excellent agreement with the L/R time constant of 0.088 ps calculated when setting r to 5 µm in the model described in Subsection 7.2.2. This result further validates the simple circuit model we used above and its predictive value.

7.3 Control of the magnetization in a ferrimagnet

The broad frequency content of the ultrafast magnetic field steps shown above makes them suitable for controlling magnetization in a wide variety of magnetic materials that feature magnons and spin-lattice relaxation rates in the sub-GHz to THz frequency range. As a proof of principle, we apply these magnetic field steps to control the orientation of the magnetization in a ferrimagnetic $Lu_{3-x}Bi_xFe_{5-y}Ga_yO_{12}$ garnet [87] (Bi:LIGG in the following). A commercial Bi:LIGG sample with bismuth substitution $x \sim 1$ and gallium substitution $y \sim 1$ (see Appendix A) was used in place of the GaP detector.

The geometry of the experiment is shown in the left panel of Figure 7.5. The in-plane magnetized Bi:LIGG film is ~3 µm thick and grown on a $Gd_3Ga_5O_{12}$ substrate not shown in the sketch (see Appendices A and B for more details). Instead of using a GaP magneto-optic detector, in this experiment, we measure the Faraday rotation accumulated by a linearly polarized 800 nm probe pulse traversing the Bi:LIGG layer. Therefore, the polarization rotation becomes a highly sensitive probe of the magnetization dynamics triggered in the Bi:LIGG [52, 88, 50] (see also the discussion of Subsection 3.1.3). As for the experiment shown in Figure 7.1, a 400 nm quench pulse is used to disrupt superconductivity in the $YBa_2Cu_3O_7$ disk and trigger a magnetic field step that excites the Bi:LIGG sample.

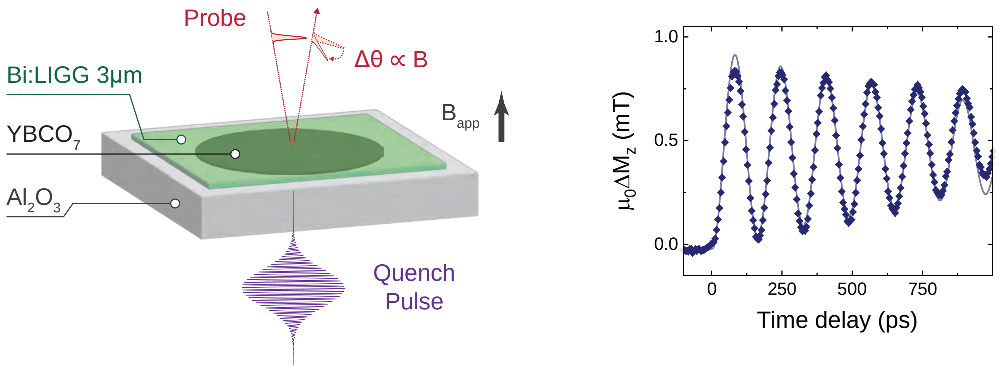

Figure 7.5: Experimental configuration to expose a magnetic sample to a magnetic step and measure the magnetization dynamics inside of it. The right panel shows the result of this measurement. Material from [47].

The right panel of Figure 7.5 shows the time-dependent changes in the magnetization's z-component triggered by the magnetic field step, measured in correspondence with the center of the disk, with the same pump fluence used for the experiment shown in Figure 7.1 (i.e., ~0.3 mJcm^{-2}). As the magnetic field step excited the Bi:LIGG sample, we observed a pronounced, damped oscillation superimposed with a sudden change in the magnetization direction. The data fits well with a phenomenological model including a step and a damped oscillatory term (see Subsection 7.3.2). The frequency of the oscillations extracted from the fits is ~6 GHz, in good agreement with the ferromagnetic resonance frequency of similar Bi-substituted rare-earth iron garnets [50, 88].

7.3.1 Absence of pump-induced magnetization dynamics above T_c

In the spirit of excluding possible erroneous conclusions, we run an experiment in the same conditions reported above, only changing the base temperature of the sample to 100 K, higher than T_c of the $YBa_2Cu_3O_7$ device. Figure 7.6 shows the result of this experiment (in black) compared to the measurement performed below T_c (in blue). The signal is absent when the device is not superconducting, and no magnetic field step is generated (see Figure 5.4). We can, therefore, consider less plausible the hypothesis that the magnetic oscillations measured are caused by possible spurious couplings between the quench beam and the sample magnetization rather than by the ultrafast magnetic transient ensuing after the disruption of shielding currents.

Additionally, we want to stress that we use a *4f* imaging system like the one described in Section 5.2 to image the shadow of a disk mask matching the size of the $YBa_2Cu_3O_7$ disk onto the superconductor. Using this precaution, we make sure that only the region where the absorbing film is present is illuminated, reducing to a minimum the radiation hitting directly the $Lu_2Bi_1Fe_4Ga_1O_{12}$ sample.

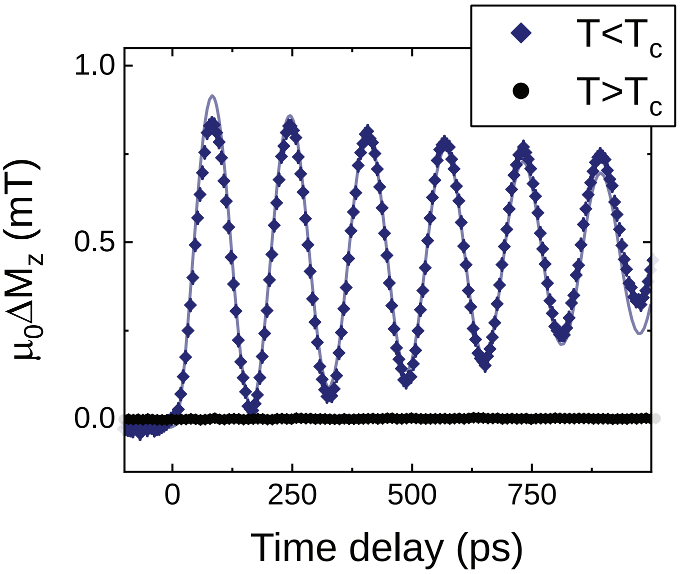

FIGURE 7.6: Measured magnetic field above the center of the superconducting disc below T_c at 55 K (blue diamonds) and above T_c at 100 K (black circles) in Bi:LIGG. The error bars denote the standard error of the mean. Material from [47].

7.3.2 A minimal model for the magnetization oscillations

The left panel of Figure 7.7 schematically shows the time dependence of the magnetic field applied to the Bi:LIGG sample. H_{step} is the local field generated by the superconducting thin film. At negative time delays, it is antiparallel to the externally applied field H_{app} due to the presence of magnetic flux trapped in the superconductor (see Appendix G). After the quench pulse hits the $YBa_2Cu_3O_7$, it promptly becomes parallel to H_{app}. H_A lies in the plane of the Bi:LIGG film to account for shape anisotropy. Due to a demagnetizing factor close to unity in our geometry [40], we set H_A equal to the saturation magnetization ∼175 kAm^{-1} (see below). While H_{step} varies in time, the anisotropy field H_A is constant. The combination of H_A and H_{step} gives rise to an overall effective magnetic field H_{eff} along which the magnetization points in equilibrium conditions and whose changes determine the dynamics of the magnetization (note that the angles in the figure are exaggerated for clarity).

The right-hand-side panel of Figure 7.7 describes the dynamics of the net magnetization in Bi:LIGG. At negative pump-probe time delays, the system is in equilibrium, and the magnetization is parallel to the effective field H_{eff}. When H_{step} suddenly changes after the disruption of superconductivity in $YBa_2Cu_3O_7$, the magnetization starts precessing around the new direction given by H_{eff}. The z-component of the magnetization oscillates in time at a frequency given by [40, 50]: $\omega = \gamma(H_{step} - H_A)$. Neglecting H_{step} (which is much smaller than the anisotropy field) and taking $\frac{\gamma}{2\pi} = 28\,\mathrm{GHzT}^{-1}$ [89], we extract a saturation magnetization of 175 kAm^{-1} for the measured oscillation frequency of ∼6 GHz (see Figure 7.5 or 5.4). This value agrees with literature data for

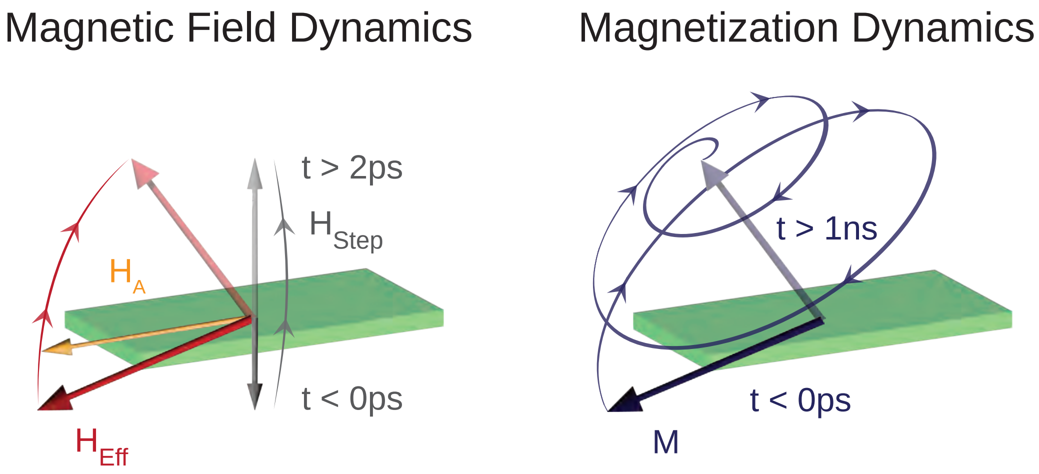

FIGURE 7.7: Left panel: schematic representation of the dynamics of the effective magnetic field (H_{eff}) inside the Bi:LIGG sample. Right panel: schematic representation of the magnetization (M) dynamics in Bi:LIGG. Material from [47].

similar Bi-substituted rare-earth iron garnets and justifies the assumptions made above [88]. In light of the simple model discussed above, we fitted the magnetic oscillations shown in Figures 7.5 and 5.4 with the following heuristic function:

$$y(t) = y_0 + A \cdot (1 + \sin(2\pi f(t - t_0) + \phi)) \cdot e^{-\frac{t-t_0}{\tau}} \cdot \left(1 + \mathrm{erf}\left(\frac{t - t_0}{\sigma}\right)\right)/2 \qquad (7.2)$$

This equation captures the damped magnetic oscillations observed in the data and is compatible with the magnetic precession discussed above. Here t is the independent variable representing the time delay, y_0 is the baseline at negative time delays accounting for the magnetic flux trapped at $t < t_0$, A is the amplitude of the magnetic step and the magnetic oscillations, f is the frequency of the magnetic oscillations measured, t_0 is the arrival time of the quench beam, ϕ is a phase term added to account for the initial phase of the oscillations, τ is the characteristic damping time of the oscillations and σ is the width of the error function necessary to kill the exponential divergence of the fitting function at negative times while ensuring a smooth fit around time $t = t_0$ (with $\sigma \sim 0.1\,\mathrm{ps}$). The value of ΔM shown in Figures 7.5 and 5.4 is achieved by subtracting to the magnetization measured the fitted value of $y_0 = -1.375\,\mathrm{mT}$, different from zero due to the presence of negative trapped flux before the pump pulse hits the sample. The values of f and of τ extracted from the fit are 6.17 GHz and 1.23 ns respectively.

7.3.3 Simulating the dynamics of the magnetization oscillations

For comparison with the model discussed in the previous subsection, Figure 7.8 displays the result of a macro-spin model calculation of the magnetization dynamics following the ultrafast magnetic field step.

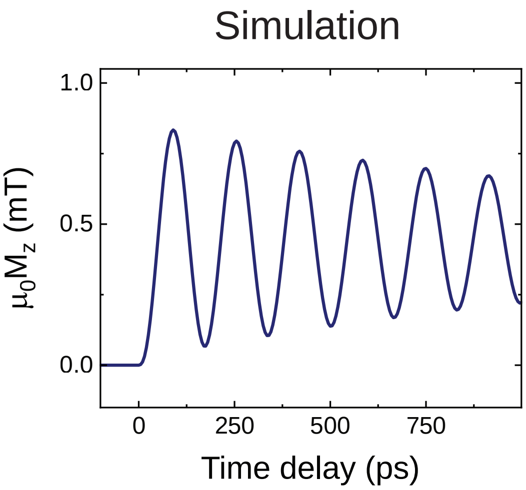

FIGURE 7.8: Micromagnetic calculations in the macrospin approximation. The simulation setup reproduces the experimental conditions and uses as input magnetic bias the magnetic field step. Material from [47].

We used the COMSOL Micromagnetics Module developed by Dr. Weichao Yu (Institute for Nanoelectronic Devices and Quantum Computing, Fudan University) to perform these simulations. This package uses a finite element method to solve the Landau-Lifshitz-Gilbert (LLG) equation. We set the value of the saturation magnetization (M_s) of our sample to 175 kAm^{-1}, as discussed above, and we adjust the value of the Gilbert damping to 0.017 to fit our data. We simplified the calculation by modeling our sample as a magnetized cubic monodomain with lateral size 10 nm to avoid the high computational costs associated with reproducing the geometry of the sample in our experiment. Following this assumption, we are effectively treating the magnetization of the ferrimagnet as a single macro-spin. To factor in the shape anisotropy of our experiment, we artificially inserted an effective magnetic field orthogonal to the applied magnetic field, having amplitude M_s. This choice is because the demagnetizing factor of the Bi:LIGG thin film sample along the z-direction orthogonal to the plane is ~ 1 [40, 22].

The z-direction is thus a hard axis for the magnetization that can be described by an energy term equal to $E_{shape} = \frac{1}{2}\mu_0 M^2 \ \cos^2(\theta)$, where θ is the angle between the film normal and the magnetization vector M (see for instance Chapter 6 paragraph 7.2 of reference [22]). When no magnetic field is applied, the magnetization lies naturally in the plane of the film, while a perpendicular field cants the magnetization to the out-of-plane direction. For small out-of-plane rotations of the magnetization (i.e., $\theta \sim \frac{\pi}{2} + \epsilon$, with $|\epsilon| \ll 1$) the energy term E_{shape} can be modeled by introducing an effective magnetic field lying in the plane of the film and pointing along the direction of the equilibrium magnetization with a modulus equal to the magnetization itself, corresponding to an energy term: $E_{eff} = -M \cdot H_{eff} = -\mu_0 M^2 \ \cos(\frac{\pi}{2} - \theta)$. We substitute $\theta \sim \frac{\pi}{2} + \epsilon$ into $E_{eff} = -\mu_0 M^2 \cos(\epsilon) \sim -\mu_0 M^2 + \frac{1}{2}\mu_0 M^2 \epsilon^2$ and into $E_{shape} = \frac{1}{2}\mu_0 M^2 \cos^2(\frac{\pi}{2} + \epsilon) = \frac{1}{2}\mu_0 M^2 \sin^2(\epsilon) \sim \frac{1}{2}\mu_0 M^2 \epsilon^2$ and see that, modulo a renormalization of the energy independent on the angle, the two energy terms have the same functional form. Therefore, they yield the same force on the sample magnetization in the LLG equation.

Finally, the small angle approximation invoked above is justified in our case since the amplitude of the perpendicular magnetic field applied (i.e., the ultrafast magnetic step) is at most $3\,\mathrm{mT}$ while $M_s = 175\,\mathrm{kAm}^{-1} \sim 220\,\mathrm{mT}$. The angular deviation from the plane is thus $< 1\,\mathrm{deg}$. In this way, we demonstrated that modeling shape anisotropy with a static effective magnetic field in the plane is justified.

We then applied a perpendicular magnetic field with the same temporal profile of the magnetic step measured in GaP and we tracked the time evolution of the z-component of the magnetization of the macro-spin representing the Bi:LIGG sample. Figure 7.8 shows the results of this simulation when the magnetization dynamics are triggered by a magnetic step similar to the one reported in Figure 7.1. This simulation matches the experimental results in Figures 7.5 and 5.4.

7.4 Applications of the magnetic steps

As discussed in the previous sections, the disruption of superconductivity in the $YBa_2Cu_3O_7$ disk with ultraviolet laser pulses can be used to perturb the magnetic field profile surrounding them, enabling the generation of magnetic field steps with ultrafast rise times and super-nanosecond long decay times.

As shown in Section 7.3, ultrafast magnetic field steps open up a new path toward efficient magnetization switching. With the unique properties of our magnetic transient, one could switch the magnetization of a magnetic material with a coercive magnetic field of a mT or less. The size of our device, and therefore the region in which the ultrafast magnetic step is applied, is tailorable. For instance, faster rise times could be achieved by reducing the size of the superconducting disk down to the micrometer scale, reducing the geometrical inductance of the superconducting disk (see Subsection 7.2.3).

We also foresee possible applications of our technique as a probing tool for quantum materials. For example, a step function with long decay times represents a suitable tool to study persistent currents in (photo-excited) superconductors. Due to its perfect conductivity, a superconductor responds to a step-like magnetic field excitation by creating superconducting currents shielding the magnetic transient for infinitely long time scales. Because our magnetic field can be switched on at timescales shorter than the lifetime of the transient state, inducing magnetic shielding currents, this time domain technique could be used to study transient superconductors [1, 2, 4, 6, 3] as anticipated in Section 1.3.

Furthermore, our technique can be applied as a complementary tool to THz time-domain spectroscopy to study low-lying excitations in a large variety of quantum

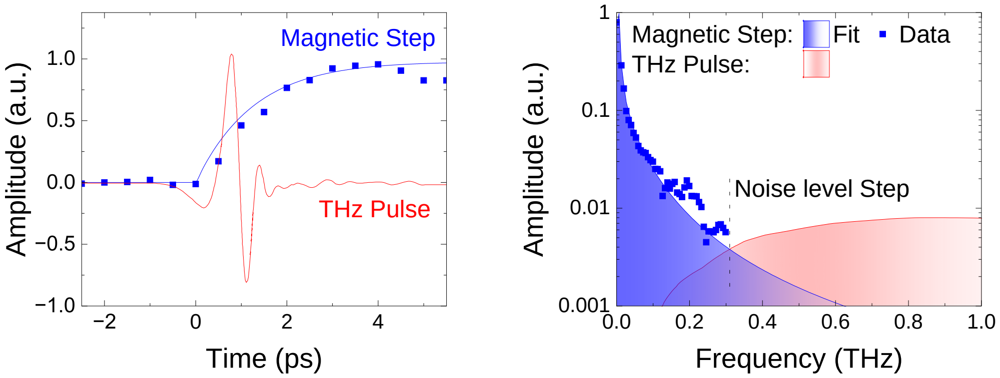

FIGURE 7.9: The left panel shows experimental data (blue squares) and a fit to the data (blue solid line) for a magnetic step and the amplitude of the measured electric field of a single cycle THz Pulse from reference [83] (red solid line). The two signals are normalized to have the same peak value. The right panel shows the Fast Fourier Transform of the time domain traces on the left. Material from [47].

materials given its broadband frequency content, ranging from sub-GHz to the sub-THz regime. Figure 7.9 shows how the THz spectroscopy and the ultrafast magnetic steps examined in this chapter establish a complete set of tools for low-frequency magnetic spectroscopy. The left panel of the figure shows experimental data (blue squares) and their fit (blue solid line) for a magnetic step generated with our technique and the amplitude (red solid line) of the measured electric field of a single cycle THz Pulse from reference [83] (the two signals are normalized to have the same peak value). The right panel of the figure shows the Fast Fourier Transform of the time domain traces in the left panel. The experimental data relative to the magnetic step (blue squares) is shown up to 0.3 THz, the frequency above which the signal falls below the noise threshold.

Moreover, because the generated fields are in the near field, our technique may be particularly suitable for studying samples with lateral dimensions significantly smaller than the wavelength associated with sub-THz radiation. This is, for example, the case of novel two-dimensional (anti)ferromagnetic materials, which are available only in micrometer-scale sizes [90].

Finally, with suitable improvements, these magnetic steps can be made both larger and faster, leading to new applications that range from quenches across phase transitions to complete switching of magnetic order parameters. Two possible ways of attaining such improvements are modifying the geometry or using other materials as active devices. For instance, the amplitude of these magnetic field steps could be made larger using ultrafast demagnetization in ferromagnetic materials [91].

Chapter 8

Conclusions and outlook

The results discussed in this thesis highlight the capabilities of a "rediscovered" technique as a critical tool enabling the investigation of a new field: the ultrafast magnetic dynamics of photo-excited superconductors. On one side, in this final chapter, we would like to underscore the most significant implications of the measurements presented and elaborate on possible further directions in which they could be expanded. On the other, we give a broader outlook on problems in which measuring the magnetic field distribution with temporal and spatial resolution is crucial. The technique we developed could be fruitfully employed for this class of experiments to answer important questions. Finally, we generally examine the potential of ultrafast magnetometry as a platform to uncover new physical phenomena.

8.1 Magneto-Dynamics of photo-excited superconductors

In this thesis, we used ultrafast light pulses to initiate ultrafast non-thermal dynamics in superconductors and studied the magnetic transient ensuing from this ultrafast stimulus. We measured the magnetic transient following the disruption of the magnetic shielding currents in an equilibrium superconductor immersed in an externally applied magnetic field. The significance of this measurement is two-fold: first, it demonstrated the time resolution of our technique. Second, given its peculiar characteristics, it inspired us to exploit this physical phenomenon as a probing tool for studying quantum materials. Next, and more importantly, we showed measurements revealing the Meissner-like magnetic dynamics of a superconductor above T_c under resonant phonon driving. The significance of these measurements is very high because they allow us to draw another evocative parallelism between light-induced and equilibrium superconductivity. The magnetic transient measured on the edge of the photo-excited region is compatible with the transient expulsion of the static magnetic field applied, which is reminiscent of the equilibrium Meissner effect. Therefore, not only does the conductivity develop superconducting-like features, as demonstrated by THz reflectivity data, but the magnetic response also entails some superconducting-like order. Admittedly, the conclusions that can be drawn from transient optical conductivity measurements are, albeit very striking, still partial. The reasons are that the scattering time measured is intrinsically limited to the lifetime of the state (see Section 1.2) and that the quantitative predictions made suffer from the reconstruction model chosen [63, 13]. In summary, THz conductivity measurements are compatible with (and very suggestive of) dissipationless transport but not conclusive. Conversely, the expulsion of magnetic fields measured here provides evidence that the state arising after mid-infrared excitation is not only characterized by an enhancement in conductivity but shows properties that *cannot* be explained assuming a state without superconducting-like quantum coherence. Moreover, the results obtained are robust against the assumptions made to model the thickness of the superconducting-like region, which, instead, impact the THz reflectivity data. As shown in Figure 6.4, within all reasonable scenarios, the expulsion measured falls in the universality class of superconductors.

Thus, measuring ultrafast magnetic field expulsion is an excellent approach for characterizing photo-excited superconductors. A natural way forward is to conduct similar measurements on other samples of $\mathrm{YBa_2Cu_3O_{7-\delta}}$ showing light-induced superconductivity at different doping or other materials. Another possibility is to improve the technique and use an approach similar to the one used for the disruption measurements below T_c (see Figure 5.4), also for the enhancement of superconductivity above T_c. This would be possible by thinning down the bulk $\mathrm{YBa_2Cu_3O_{6.48}}$ sample, exposing the c-axis to a few microns thickness. This way, the magneto-optic detector would be close enough to the photo-excited region even when pumping the opaque sample from the opposite side. The advantages of this approach are a much simpler and flexible device preparation, not relying on a sapphire shield fortuitously shielding 15 µm radiation, and the possibility to characterize more quantitatively the magnetic expulsion of the photo-excited state without relying on complex simulation models. Focused ion beam machining represents the technology enabling us to produce a lamella from a bulk sample, which is thin enough to comply with our requirements [92].

8.1.1 Flux quantization in a photo-excited superconductor

Another exciting direction in the field of photo-excited superconductivity is measuring the dynamics of the quantized magnetic field flux, or, to be more precise, the fluxoid quantization. Inspired by experiments done on equilibrium superconductors (see, for instance, [93]), we could shape our $\mathrm{YBa_2Cu_3O_{7-\delta}}$ sample like a ring. Upon photo-excitation above T_c, we would expect the sample to expel an externally applied magnetic field from its volume and the field to accumulate in the center of the ring as an integer number of flux quanta. Suppose the inner diameter of the ring is 10 µm wide, we would then expect a field to be quantized in steps of ∼26 µT, corresponding to a single flux quantum. Such a value is easily measurable with the sensitivity of our technique (see, for instance, Figure 6.3 for comparison) and a thin enough magneto-optic detector.

However, what would it mean to see such a quantization take place? Following the discussion made in reference [7], the deepest definition of superconductivity is: a state characterized by a many-particle condensate wavefunction with amplitude and phase and maintaining phase coherence over macroscopic distances. The existence of a phase that is single-valued implies that it must rewind onto itself, modulo 2π, after evolving along a closed loop. If we take any loop around the hole of a ring, this requirement still holds and leads to quantization of the fluxoid Φ' threading the loop:

$$\Phi' = \Phi + \frac{m^* c}{e^{*2}} \oint \frac{\mathbf{J_s} \cdot d\mathbf{s}}{|\psi|^2} \tag{8.1}$$

Therefore, fluxoid quantization is a physical process directly connected to the most stringent definition of superconductor and a meaningful next benchmark for light-induced superconductivity.

Before we rush to execute this experiment, we need a further comment: strictly speaking, only the fluxoid Φ' is quantized and not the magnetic flux Φ threading the loop. In most practical cases, the two quantities coincide, given that the thickness of the ring is usually more extensive than the magnetic field penetration depth, which is the region where the superconducting current $\mathbf{J_s}$ flows. Therefore, we can always choose a contour loop sufficiently deep into the sample volume such that the integral term in Equation 8.1 vanishes, leading the fluxoid to coincide with the magnetic flux quantum. In the case of a photo-excited superconductor with a very extreme aspect ratio, the penetration depth is renormalized to a more considerable value, i.e., the Pearl length (see Section 2.5). This correction could mean that the critical superconducting currents do not vanish at the edge of the photo-excited region's outer diameter, giving a finite integral contribution in Equation 8.1. That would amount to the fact that the magnetic flux quantization is not required, even if the general condition that the fluxoid needs to be quantized still holds, making the experimental evidence more unclear.

8.2 Other future perspectives

In this final section, we focus on the intrinsic capabilities of the technique and elaborate on other potential directions in which they could be productively employed. In general, the ability to measure changes in the magnetic field with sub-picosecond time resolution and micrometer spatial resolution is a technical achievement that could unlock many experimental paths. In the following, we report three examples in which ultrafast optical magnetometry could lead to significant insights.

8.2.1 Investigating the effective magnetic field of circular phonons

As demonstrated initially by Nova et al. [94], intense circularly polarized mid-infrared pulses tuned to resonance with specific doubly degenerate phonon modes in the material generate an effective magnetic field that can be measured via Faraday polarization rotation in the material. After that initial account, other experiments have reported an electric-field-driven magnetization upon mid-infrared or terahertz light excitation [42, 95]. It is still debated whether the magnetization thus generated in the material corresponds to a classical type of magnetization (analogous to the one appearing in Maxwell's equations) or whether the polarization rotation is given by a non-linear coupling between the pump and the probe [41]. There are doubts because the measured polarization rotation is usually associated with a magnetization much larger than what is theoretically expected from the circular motion of driven phonons [42]. Our technique is valuable for distinguishing the two possible scenarios anticipated above. If the magnetization induced by the pump is a conventional Maxwellian field, it will radiate a magnetic field outside the sample, respecting the boundary conditions imposed by Maxwell's equations. Conversely, if the source for polarization rotation is a non-linear coupling between pump and probe or an electron-phonon coupling mechanism, having the exact same symmetry as the Faraday effect, then we would not expect to measure a magnetic field outside the sample. Our strategy combines measurements of the polarization rotation directly inside the sample with measurements of the magnetic field outside it using a spectator magneto-optic detector placed close to the photo-excited region and not interacting with the pump. The former approach is helpful for experimentally estimating the magnetization value that would give rise to such a rotation via the Verdet constant of the material. The latter experiment is suitable for checking whether the expected magnetic field associated with this magnetization is present near the sample.

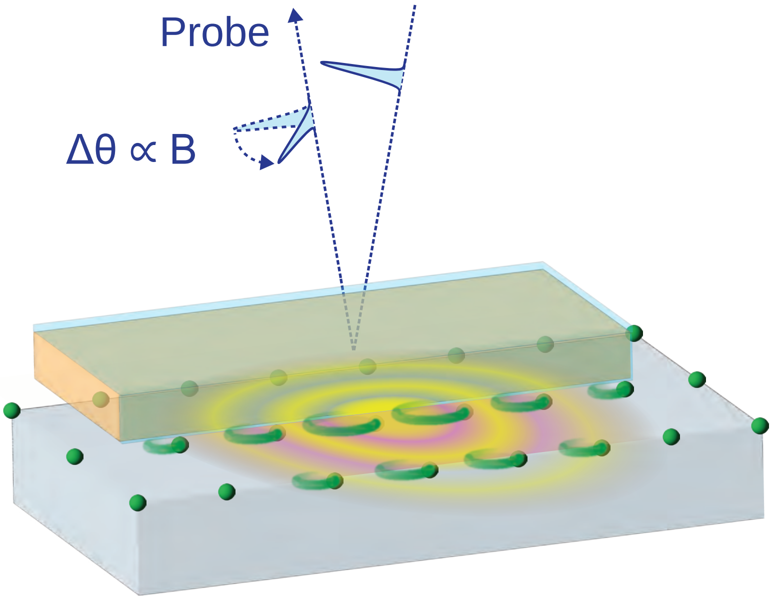

FIGURE 8.1: The SiC sample is depicted in grey. A magneto-optic detector (GaP) is placed on top of it and is shielded from the pump beam (not shown) by a mid-infrared frequency filter that allows the probe to pass and rejects the pump. A magnetic wave (yellow) radiates from the motion of the circular phonons excide in the sample.

The sample we could choose for such an experiment is silicon carbide (SiC). The feasibility of this measurement can be estimated using a finite element method to extract the magnetic field that is generated near the edge of a thin photo-excited volume of SiC after photoexcitation of the 30 THz doubly degenerate mode (see Figure 8.1). This simulation is performed under the assumption that driving induces a homogeneous magnetization of $0.15\,\mu$B/u.c. (as calculated in reference [96]). Considering a 30 µm thick Faraday detector placed 45 µm away from the photoexcited area the sensed magnetic field values are expected to be ∼130 µT, well above the sensitivity of our technique (see, for instance, Figure 6.3).

8.2.2 Investigating ultrafast demagnetization

A similar approach could add a piece to another exciting puzzle in ultrafast physics: ultrafast demagnetization discovered by Beaurepaire et al. in nickel [91]. This phenomenon offers opportunities for ultrafast magnetic data storage and has, therefore, very appealing application prospects. While this phenomenon has been observed in many other systems, it is still not fully understood. For example, it was only recently recognized that the missing angular momentum ensuing from the ultrafast demagnetization process is transferred to a long-lasting, non-equilibrium population of high-frequency circularly polarized phonons absorbing the angular momentum of the spin system before macroscopic sample rotation [97]. An interesting experiment in this context would be again placing a spectator magneto-optic detector to measure the magnetic field dynamics following the ultrafast quench of the magnetization of the sample. Our technique appears to be suitable for such a measurement, with sufficient time resolution to follow this ultrafast process happening in sub-picoseconds time scales. Depending on the result of this experiment, ultrafast demagnetization could also be exploited as a tool to create magnetic steps retaining the same speed demonstrated in Chapter 7 but having a much bigger amplitude given the considerable magnetic field generated by the magnetization of ferromagnetic materials. A sufficiently strong ultrafast magnetic field transient is an exciting tool, as it could unlock access to new states of matter accessible through ultrafast magnetic field quenches as discussed in the next subsection.

8.2.3 A platform for ultrafast magnetic quenches

Manipulating material properties to achieve novel phases with new functionalities is a major drive for technological progress. Therefore, searching for new tools to control material properties is a high priority in condensed matter physics. Many different tuning knobs are already available, and among them, magnetic fields possess fascinating capabilities. The quantum Hall effect [98] and the promotion of a fully developed 3D charge order in an unconventional superconductor [99] are examples of magnetic fields producing new equilibrium phases. Similarly, a platform generating strong magnetic transients to study the effect of magnetic fields on quantum material beyond equilibrium is a new and exciting pathway to uncover new out-of-equilibrium phases of matter. We could use ultrafast laser pulses as a promising candidate to generate magnetic transients flexibly. As discussed in Subsection 8.2.1, exciting certain materials with circularly polarized light coupling to their phonons (see Figure 8.2) can induce transient magnetic fields with amplitudes up to a few teslas [95]. If these magnetic transients are associated with real magnetic fields and not with a synthetic field caused by light-matter coupling, these could be used to excite other samples magnetically.

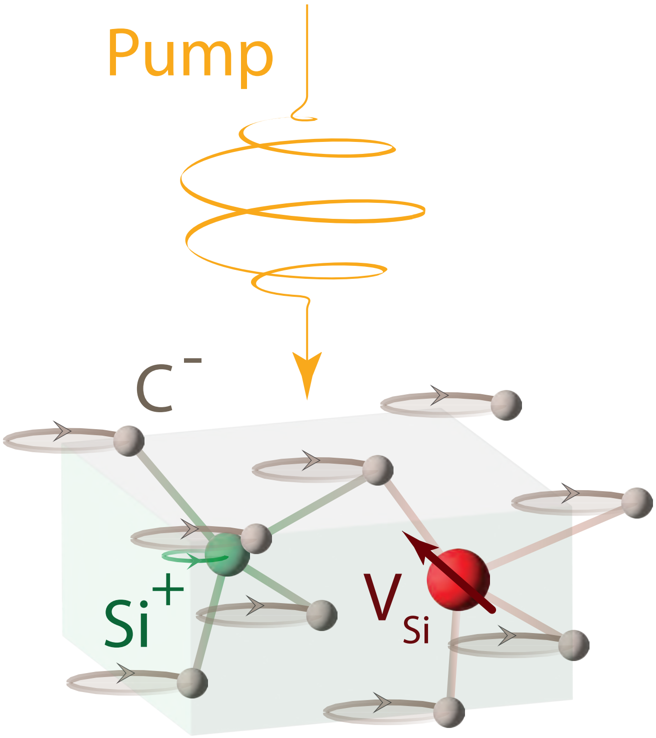

FIGURE 8.2: Photoexcited circular phonons in SiC with silicon vacancies for sensing

We could also think about an alternative approach to the one discussed in Subsection 8.2.1 to investigate the nature of these light-induced magnetic transients. As a probing mechanism exclusively sensitive to magnetic fields, we propose magnetic sensing with color centers here. Ultrafast time resolution for color centers has not yet been demonstrated, but ideas are present on extending their probing potential to the ultrafast regime [100]. A good material candidate for this experiment is again silicon carbide (SiC). As discussed above (see Subsection 8.2.1), this compound has been predicted to possess a high susceptibility to magnetize under resonant phonon photoexcitation. Moreover, it hosts silicon vacancies known as qubit systems for sensing magnetic fields [101]. Thus, we could generate and detect magnetic fields at once (see Figure 8.2). A thin sample transferred close to the photo-exited layer would be then exposed to a strong magnetic transient. Its dynamic magnetic response is directly accessible to the silicon vacancies in SiC. At the same time, other probes could be used to measure how its other physical properties change versus pump-probe delay.

Appendix A

Sample characterization[1]

The optimally doped $YBa_2Cu_3O_7$ thin films were obtained through a commercial supplier (Ceraco GmbH) and grown on r-cut Al_2O_3 substrates. We chose the S-Type films, with a thickness of approximately 150 nm, critical current density greater than $2\,\mathrm{MAcm}^{-2}$ and specified T_c of 86 K. The superconducting transition temperature of the device after lithography (see Appendix B) was 85 K (see Figure 4.3). The slight copper excess used by the manufacturer to optimize the superconducting properties of the sample results in small copper-oxide precipitates on the surface of the YBCO film. These defects impact the sample's magnetic properties as discussed in Chapter 2.

The Bi-substituted lutetium iron gallium garnet sample ($Lu_2Bi_1Fe_4Ga_1O_{12}$, for short in the following Bi:LIGG) was ∼3 µm thick, obtained through a commercial supplier and grown by Liquid-Phase Epitaxy on a (100)-oriented, 500 µm thick crystal of $Gd_3Ga_5O_{12}$ (GGG). The composition of the Bi:LIGG sample was measured using energy-dispersive X-ray spectroscopy (EDX), yielding the following percentage composition of elements: O 58.98%, Fe 19.43%, Ga 5.99%, Lu 10.28%, Bi 5.32%. This result is in good agreement with the chemical formula reported above.

The $YBa_2Cu_3O_{6.48}$ single crystals had typical dimensions of approximately $2\,\mathrm{mm} \times 2\,\mathrm{mm} \times 0.5\,\mathrm{mm}$, where the thin dimension corresponds to the c-axis, and were grown in yttrium-stabilized zirconium crucibles. The hole doping of the $Cu - O_2$ planes was adjusted by controlling the oxygen content of the Cu-O chain layer by annealing in flowing O_2 and subsequent rapid quenching. A superconducting transition at $T_c = 55\,\mathrm{K}$ was determined by SQuID DC magnetization measurements [17].

---

[1] Part of this and the following Appendices have been taken verbatim or adapted from the Supplementary Information of the related publication [47]

Appendix B

Sample preparation

A 150 nm thick $YBa_2Cu_3O_7$ film grown on a two-side polished Al_2O_3 substrate was patterned into a disc shape using a laser lithography process based on an AZ1512 photoresist mask. After exposure and development, the sample was wet etched using a 1% H_3PO_4 solution. After etching, the residual photoresist was removed using acetone and isopropanol. Figure 4.2 shows a micrograph of the $YBa_2Cu_3O_7$ film after patterning. The thin film and GaP (100) detector were then mounted onto an Al_2O_3 plate that could be fixed directly to the cold finger of the cryostat. Al_2O_3 is an electrical insulator and minimizes the shielding of magnetic fields due to eddy currents while ensuring a good cooling power. A ∼75 µm thick GaP (100) crystal (SurfaceNet GmbH) was used as a detector and put in close contact with the sample (see Figure 4.2). The detector was polished with a wedge angle of ∼1.5 deg to spatially separate the reflections from the front and back surfaces. This allowed us to detect exclusively the reflection from the back surface, which accumulated the Faraday polarization rotation signal as the probe beam propagated across the detector thickness. Additionally, the GaP back surface and the sample were not coplanar to avoid interference between the reflections from these two surfaces (see Figure 3.4). The gap between detector and the $YBa_2Cu_3O_7$ disk was ∼25 µm.

Appendix C

Experimental Setups and Data Acquisition[1]

The measurements done on $YBa_2Cu_3O_7$ were performed using the experimental setup sketched in Figure C.1. Ultrashort (100 fs) 800 nm laser pulses were produced starting from a commercial $Ti:Al_2O_3$ oscillator/amplifier chain that produced pulses with energies up to 2 mJ at a repetition rate of 900 Hz. These pulses were split using a beamsplitter into two branches. The lowest intensity branch was used after attenuation for probing the polarization rotation in the GaP (100) magneto-optic detector. To minimize the noise sources in the measurement, the polarization of the beam was set using a nanoparticle high-extinction ratio linear polarizer.

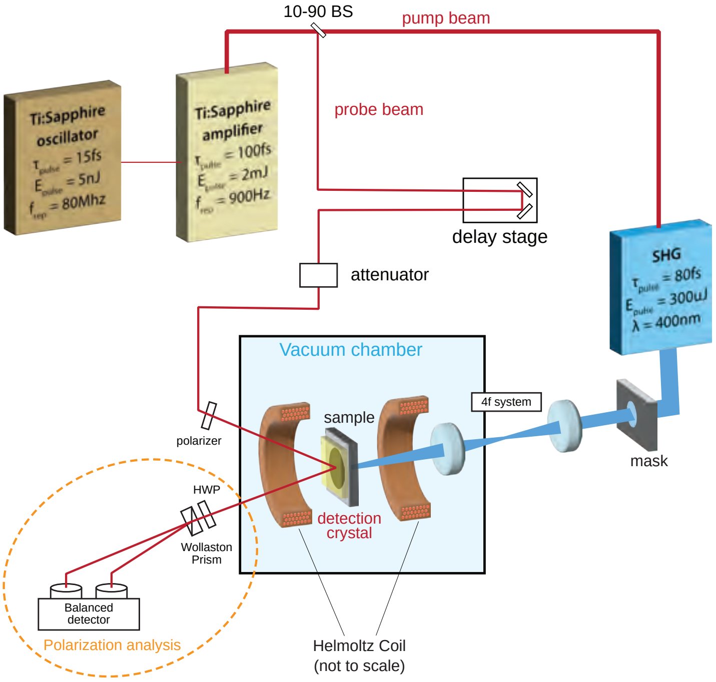

FIGURE C.1: Experimental setup used for the equilibrium and disruption measurements on $YBa_2Cu_3O_7$. Material from [47].

---

[1] Parts of this appendix, given the highly technical nature of the content, have been taken verbatim or adapted from the Supplementary Information S2 of reference [17]

As non-normal incidence reflections introduce a phase delay between s and p polarization, incidence angle fluctuations can give rise to polarization noise. To minimize this, only reflections close to normal incidence were used in the setup and a commercial system using active feedback was used stabilize the laser beam pointing. After traversing and being reflected from the second surface of the Faraday detector, the polarization state of light was analyzed using a half-waveplate, Wollaston prism and balanced photo-diode setup that allowed us to quantify the Faraday effect in the magneto-optic detection crystal. The higher intensity branch was frequency doubled to obtain 400 nm pulses using a $\beta - \mathrm{BaB_2O_4}$ (BBO) crystal that were used to photo-excite the $\mathrm{YBa_2Cu_3O_7}$ thin film samples. A mask, illuminated by these ultraviolet pulses, was imaged onto the back surface of the sample to create a flat-top circular beam whose edges matched those of the disk shaped $\mathrm{YBa_2Cu_3O_7}$ sample. This precaution, together with the superconducting film being opaque to 400 nm radiation ensured that the GaP detector was not exposed to the pump pulses.

The $\mathrm{YBa_2Cu_3O_7}$ thin film samples were embedded in the detector assembly (see Appendix B and Figure 3.4) and mounted on the cold finger of a liquid helium cryostat to allow for temperature control. The cryostat was directly placed in a high vacuum chamber. A pair of coils in a Helmholtz configuration generated a magnetic field at the sample position whose polarity could be reversed at a frequency of 450 Hz. Switching the polarity of the magnetic field helped rejecting possible spurious contributions (see Appendix D) arising from unwanted sources of bi-refringence (e.g. residual strain in the detector crystals or vacuum windows). The highest achievable magnetic field was limited by heat dissipation and was ~3 mT. The sample position was changed using computer controlled linear translation stages that made it possible to reproducibly move the cryostat and the sample inside the vacuum chamber with ~10 µm repeatability.

The measurements done on $\mathrm{YBa_2Cu_3O_{6.48}}$ were carried out with a different experimental setup sketched in Figure C.2. Here, 800 nm pulses were generated using a pair of commercial $\mathrm{Ti:Al_2O_3}$ amplifiers seeded by the same oscillator to achieve femtosecond synchronization. One amplifier produced 35 fs long, ~2 mJ pulses at 2 kHz repetition rate and was used for the probe beam. The second amplifier produced ~60 fs long, ~5 mJ pulses at 1 kHz repetition rate and was used to pump a home built three stage OPA that generated ~2 mJ total energy signal and idler pulses. These pulses were mixed in a 0.4 mm thick GaSe crystal to obtain ~150 fs long, ~20 µJ energy pulses centered at ~20 THz, close to resonance with the B_{1u} apical oxygen phonon modes of $\mathrm{YBa_2Cu_3O_{6.48}}$. These pulses were then chirped using a 10 mm NaCl rod to a duration of ~1 ps, in order to match the optimum pulse length for inducing superconducting-like optical properties in $\mathrm{YBa_2Cu_3O_{6.48}}$ [9]. While the sample stages and cryostat are similar between the two setups, in this case the polarization analysis setup is fully "in-line", i.e., the beam travels directly from the polarizer to the Wollaston analyzer without being reflected by additional mirrors other than the detector. Moreover, the optical elements used for setting the polarization before the sample and for analyzing after reflecting from the magneto-optic detector were directly

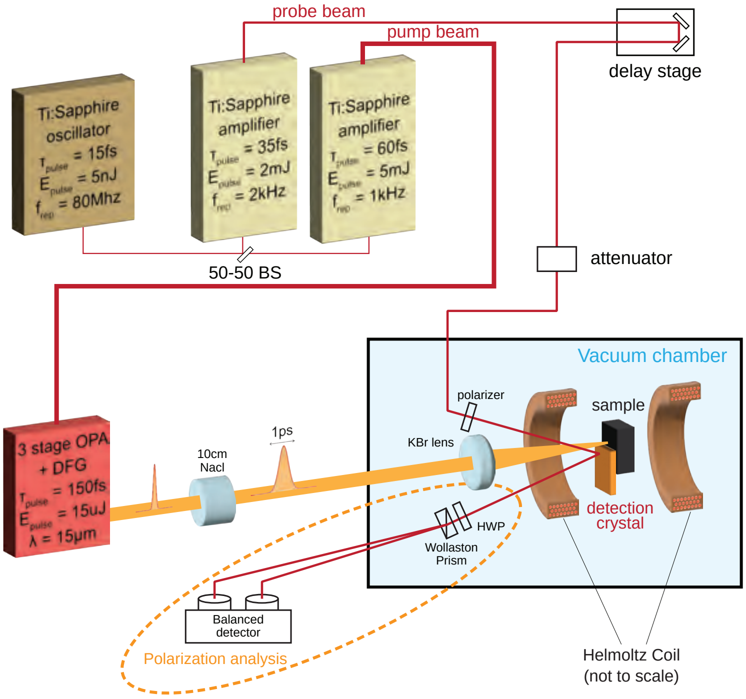

Figure C.2: Experimental setup used for the equilibrium and mid-infrared pump-probe measurements on $YBa_2Cu_3O_{6.48}$. Material from [17].

placed in the high vacuum chamber. This allowed us to avoid spurious contributions arising from vacuum windows and contributed to further reduce spurious sources of polarization noise coming from mirror reflections. A magnetic field was applied at the sample position using a pair of Helmholtz coils whose polarity was switched at $\sim$10 Hz frequency and could reach a maximum amplitude of 12.5 mT. In both experimental setups the polarity of the magnetic field is cycled periodically at a sub-harmonic of the pump and probe repetition rates.

To obtain differential magnetic field measurements the electrical pulses from the balanced photodetector were digitized using a commercial 8 channel 40 MSs^{-1} data acquisition card, triggered at the lowest frequency used in the experiment. These pulses, acquired in the time-domain, were then integrated applying a boxcar function to yield the signals from the sum and difference channels of the balanced photodetector for each probe laser pulse. Since the acquisition of a full pulse sequence required the acquisition of many cycles of the applied magnetic field, the sample clock signal of the data acquisition card was derived using direct digital synthesis from the oscillator repetition rate. In this way drifts in the cavity length and repetition rates of the system did not affect the relative timing of the boxcar functions with respect to the arrival time of the electrical trigger pulse.

Appendix D

Data reduction and analysis

D.1 Scheme for the measurements on $YBa_2Cu_3O_7$

As mentioned in Section 3.3, the polarity of the magnetic field was cycled periodically to yield differential measurements and isolate contributions to the polarization rotation that were only induced by the applied magnetic field. In other words, because the equilibrium and pump-induced magnetic field changes measured with applied field $-H_{app}$ were subtracted from those acquired with applied field $+H_{app}$, the sensitivity of the signal to strain in the magneto-optic detector or polarization noise in the setup was strongly reduced. Below, we discuss this approach in detail.

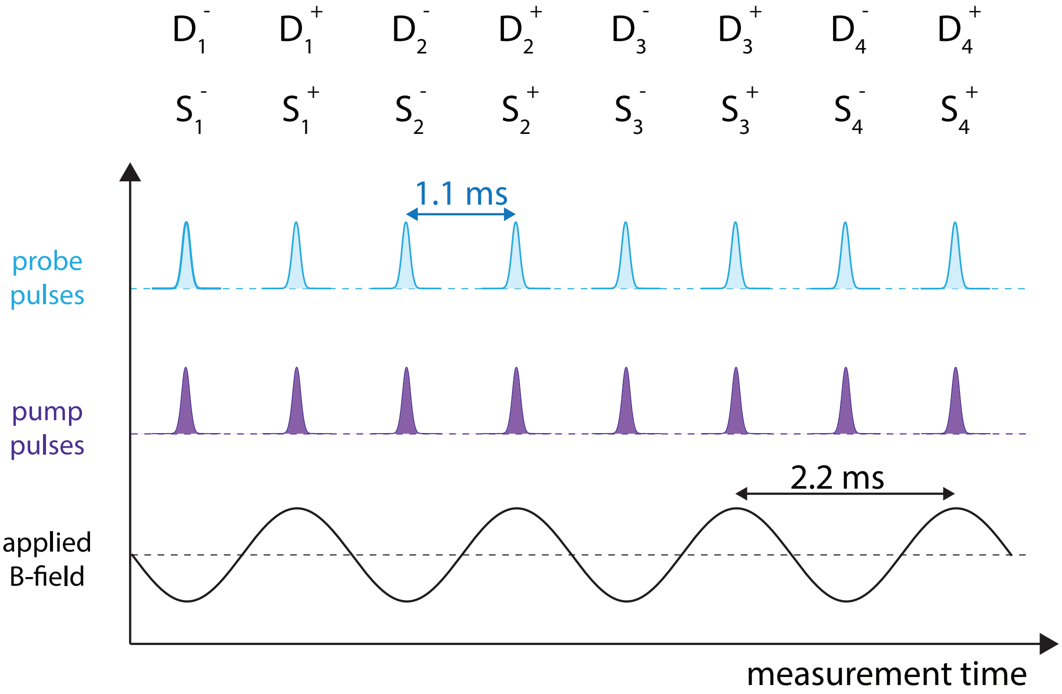

FIGURE D.1: Timing diagram of the acquisition scheme used for the measurements on $YBa_2Cu_3O_7$. We indicate the signals from the difference and sum channels of the photodetector with D and S, respectively. Material from [47].

The magnetic field polarity was cycled following a sinewave at 450 Hz frequency.

We chose the highest possible switching frequency to reject low-frequency 1/f noise effectively. Figure D.1 shows a timing diagram of the acquisition scheme. As mentioned in Appendix C, we triggered the data acquisition card at a sub-harmonic frequency of the probe repetition rate corresponding to traces comprising 88 pulses (a trace of 8 pulses is shown in Figure D.1 as an example). In the end, only 80 of these 88 pulses were acquired due to a fixed dead time for data processing.

We label signals from the difference and sum channels of the photodetector as $D_i^{\pm}$ and $S_i^{\pm}$ respectively, to indicate whether they were acquired with positive (+) or negative (−) polarities of the applied magnetic field. The subscript i runs over the 80 acquired pulses in the acquisition trace. The polarization rotation within a trace is calculated in the following way:

$$\Delta\theta = \frac{\sum_{i=1}^{80} D_i^{+}}{\sum_{i=1}^{80} S_i^{+}} - \frac{\sum_{i=1}^{80} D_i^{-}}{\sum_{i=1}^{80} S_i^{-}} \tag{D.1}$$

This quantity yielded the amplitude of the magnetic field after calibration of the Faraday effect in the GaP (100) detector and the Bi:LIGG sample (see Section 4.2). To limit computational dead times between acquisitions, we normalize after averaging as indicated in the formula above.

The sequential acquisition of multiple pulses (88) allowed us to minimize the impact of lost pulses during processing time while keeping the frequency of acquisition as high as possible to reject the effect of low-frequency noise when averaging the difference and sum channels within a trace before taking the ratio of the two quantities. To cancel out residual drifts due to possible asymmetries in the applied magnetic field, the phase of the sinusoidal applied magnetic field to the laser pulse train was periodically alternated between 0 and π.

For the pump-probe measurement protocol, we acquired each probe signal with the optical pump on (see Figure D.1). This was convenient for reducing asymmetries due to the long-lasting heating effect in the superconducting film (see Appendix G). The magnetic dynamics induced by the pump were therefore measured by changing the value of the probe arrival time compared to the pump.

D.2 Scheme for the measurements on $YBa_2Cu_3O_{6.48}$[1]

Similarly to what was discussed in the previous section, in the measurements done on $YBa_2Cu_3O_{6.48}$, the polarity of the magnetic field was cycled periodically to yield double differential pump-probe measurements and to isolate contribution to the polarization rotation associated with the applied magnetic field. This allowed us to filter out all contributions to the polarization rotation that would not invert with the externally applied magnetic field. Therefore, the signal is not sensitive to magnetic fields carried by the MIR pulse or due to the transient generation of fast electrons in the sample.

---

[1] Parts of this section, given the highly technical nature of the content, have been taken verbatim or adapted from the Supplementary Information S3 of reference [17]

The amplitude of the signal of the balanced photodetector difference channel is normalized by that of the sum channel in a pulse-by-pulse manner. For convenience, we label these signals as $U_i^{\pm}$ to indicate those acquired with the pump off for positive and negative polarities of the applied magnetic field and $P_i^{\pm}$ to indicate the same signals acquired with the pump on. The subscript i runs over the n repetitions in the acquisition. The following quantities are calculated as follows:

$$\Delta\theta_{pump-off,i} = U_i^+ - U_i^- \qquad \Delta\theta_{pump-on,i} = P_i^+ - P_i^- \tag{D.2}$$

$$\Delta\theta_{pp} = \Delta\theta_{pump-on} - \Delta\theta_{pump-off} \tag{D.3}$$

Where $\Delta\theta_{pump-on}$ and $\Delta\theta_{pump-off}$ (averaged over n repetitions) are the magnetic field induced polarization rotations measured with the pump respectively off and on, and $\Delta\theta_{pp}$ is the magnetic field induced change in polarization rotation due to the pump. These quantities yielded the amplitude of the magnetic field and its pump-induced changes after calibration of the Faraday effect in the GaP (100) detector. To cancel out residual drifts, the phase of the magnetic field, as well as that of the pump laser, compared to the probe laser, are periodically alternated between 0 and π.

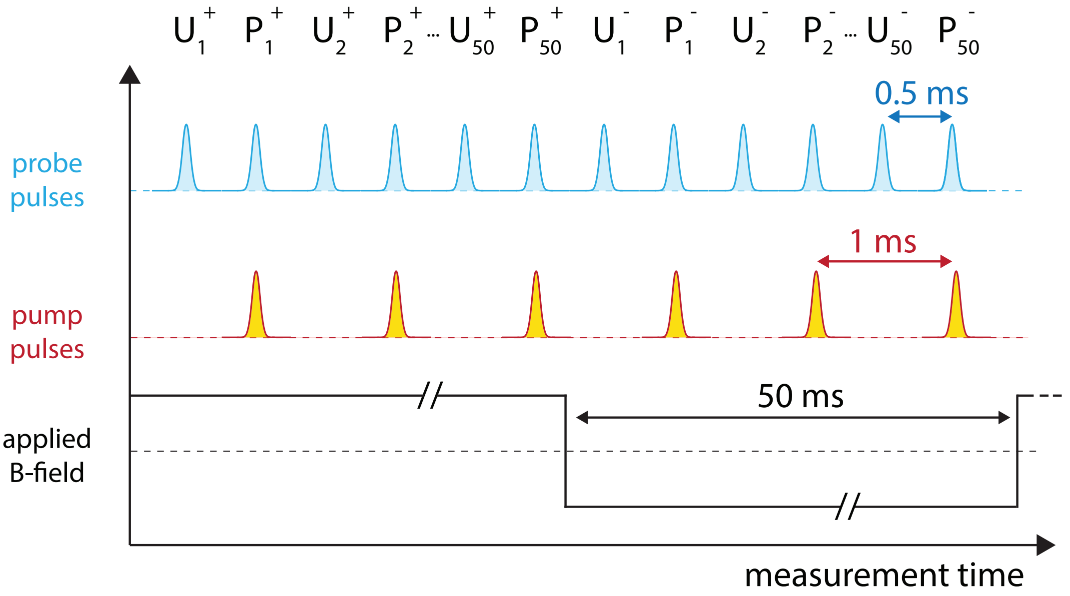

FIGURE D.2: Timing diagram of the acquisition scheme used for the mid-infrared pump, Faraday rotation probe measurements on $YBa_2Cu_3O_{6.48}$. Material from [17].

The $YBa_2Cu_3O_{6.48}$ measurements were acquired using a scheme to ensure the sample was excited in a constant magnetic field. Here, the probe repetition rate was 2 kHz, and the pump struck the sample every second probe pulse (i.e., at 1 kHz). At the same time, the magnetic field polarity was modulated following a square wave at a lower frequency of around ~10 Hz, as shown in Figure D.2. This ensured that the sample was photoexcited in a constant magnetic field. The quantities defined in the equations above were calculated, yielding double-differential pump-probe measurements that distilled only the contributions to the polarization rotation arising from pump-induced changes in the sample's magnetic properties.

Appendix E

Simulating magnetic properties of superconductors

E.1 Field cooling

When cooling a superconductor across T_c in a magnetic field, the Meissner effect occurs, and the sample expels the magnetic field from its volume. In the presence of non-superconducting defects, the field is trapped into these regions of the superconductor, leading to a reduced magnetization[102, 7] (see Figure 2.2). The $YBa_2Cu_3O_7$ thin film and the $YBa_2Cu_3O_{6.48}$ sample used have a relatively high concentration of defects (see Appendix A and Supplementary Information S1 of reference [17]). This leads to a significant difference between our samples' screening susceptibility (zero field cooled) and Meissner effect (field cooled) responses.

We used magnetostatic calculations in a 3D axially symmetric geometry to assess the effect of flux-trapping defects on the Meissner response in our experimental geometry. We focused on the optimally doped $YBa_2Cu_3O_7$ sample modeling the superconducting thin film as a uniform medium with a magnetic permittivity close to zero. The presence of defect was simulated by introducing concentric gaps (having a width of 150 nm) in the sample, spaced 10 µm from each other. The changes in the magnetic field surrounding the sample were calculated using COMSOL Multiphysics® to solve Maxwell's equations.

We calculated the measured magnetic signal in our geometry by integrating the z-component of the magnetic field in the volume of the GaP detector traversed by the probe. This has been done in two steps, first by integrating along the thickness (75 µm) of the detector and then by convoluting the result with a Gaussian envelope representing the probe spot size (50 µm FWHM). The results of this calculation are shown in Figure E.1. The presence of discontinuities, mimicking the effects of defects, strongly reduces the field-cooled magnetic response in our configuration. These defects are not spatially resolved due to the spatial average across the thickness of the GaP detector and to the smoothing effect from the finite size of the probe pulse (see Section 4.1).

Figure 2.3 shows simulations performed using a similar approach to the one described above. The sample is defined by a sizeable diamagnetic susceptibility and

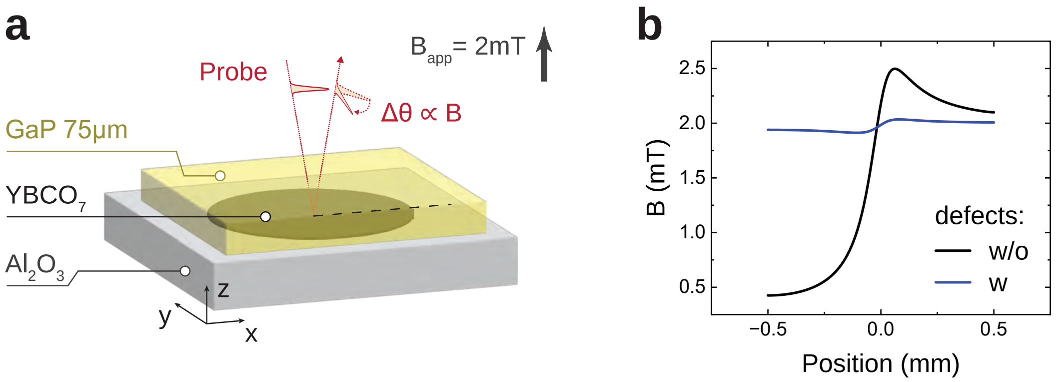

FIGURE E.1: **a**) The geometry of the experiment. The black dashed line represents the direction of the spatial scan shown in b. **b**) Simulated magnetic field spatial dependence across the edge of a perfectly diamagnetic thin disc with a radius of 500 µm in a 2 mT externally applied field, with ("w") and without ("w/o") spatial defects measured in GaP. Material from [47].

is free of defects to illustrate the effect of the demagnetizing field generated by the sample's magnetization.

E.2 Zero field cooling

This justifies our choice of resorting to a zero-field cooled protocol in our measurements (see Appendix F) to maximize the diamagnetic response of the superconductor and to decrease the impact coming from the presence of defects.

In zero-field cooled conditions, the magnetic field exclusion originates from screening currents counteracting the change of magnetic flux threading the sample when an external magnetic field is applied once the sample is cooled below T_c. We simulated this situation with finite element calculations using COMSOL Multiphysics® in a 3D geometry with axial symmetry.

The changes in the magnetic field surrounding the sample were calculated, taking into account the geometry of the experiment. The solution domain was defined as a cylindrical region with a radius and a height of 1 mm. The $YBa_2Cu_3O_7$ sample was modeled as a disk with a radius of 500 µm and a thickness of 150 nm with a high conductivity (10^{11} Sm^{-1}). The magnetic field shielding from the superconductor (discussed qualitatively in Appendix F) was modeled by ramping up a uniform applied magnetic field from 0 to 2 mT in 1 ns, along the direction perpendicular to the plane of the disk. The magnetically induced eddy currents in the simulation reproduced the effect of the superconducting screening currents measured in the experiment, having the same physical origin: Faraday law. On this short time scale, the decay of the eddy currents was negligible (due to the high conductivity of the sample), and the magnetic shielding was constant, as expected from superconducting persistent currents. Due to its much lower conductivity, the $YBa_2Cu_3O_7$ substrate was not included in the modeling. Furthermore, we did not include effects due to the finite critical current of the sample since the magnetic field applied in the experiment (2 mT) was consistently lower than the first critical field of YBCO (∼100 mT[103]). Even taking into account demagnetizing effects appropriate for our geometry, we expect to reach the critical current threshold only in a small region close to the edge of the disk [49, 104]. Therefore, our simulation matches our experimental conditions well and agrees with the experimental results (see Subsection 4.2.2). This method has also been used to perform the simulations reported in Subsection 7.2.3.

Appendix F

Shielding of time varying magnetic fields in superconductors

When cooling a superconductor below T_c in a magnetic field, two processes can take place depending on the temporal evolution of the applied field. First, if the applied field is static, we observe the Meissner effect: the expulsion of a static magnetic field from the volume of the superconductor. In a type II thin film superconductor [49, 104] with defects [102], like our $YBa_2Cu_3O_7$ sample, this effect can be relatively small due to the formation of vortices that trap magnetic flux within the sample volume and reduce its capability of expelling applied magnetic fields (see Section 2.2). Second, if the applied magnetic field varies in time, we observe a magnetic shielding due to the perfect conductivity of the $YBa_2Cu_3O_7$ sample (see, for instance, the left panel of Figure 7.4). This response is observed in a zero-field cooled experiment [102, 7]. In this second case, magnetically induced persistent shielding currents keep the magnetic flux constant in the superconductor, as prescribed by Faraday-Lenz law, and the magnetic field is wholly excluded from the sample volume, even if defects are present. Thus, this second process produces a much bigger magnetic response than the first one, and we chose to exploit this to our advantage in our measurement protocol.

Figure F.1 qualitatively explains the equilibrium field dynamics in our experiment, which is very similar to the zero-field cooled regime. The first row (a) shows the temperature evolution during a hypothetical experiment in which a sample is progressively cooled below T_c. The second row (b) shows the probe pulses used to sample the magnetic field at a specific point in time. When there is no sample, we expect to measure a value equal to the amplitude of the applied sinusoidal magnetic field (third row (c)). The temperature dependence of the GaP detector is weak, so we do not expect any change in the detector's sensitivity when cooling. As described in Section 3.3 and in Appendix D, the magnetic field is extracted as the difference between the polarization rotation measured when the polarity of the sinusoidal wave is positive minus the one measured when the polarity is negative. The fourth row (d) schematically shows the evolution of the magnetic field upon cooling our sample across T_c. Initially, when the sample is above T_c, the magnetic field measured is almost equal to the applied magnetic field due to the higher resistivity of the sample in the normal state. Upon cooling across T_c, the superconductor partially shields the

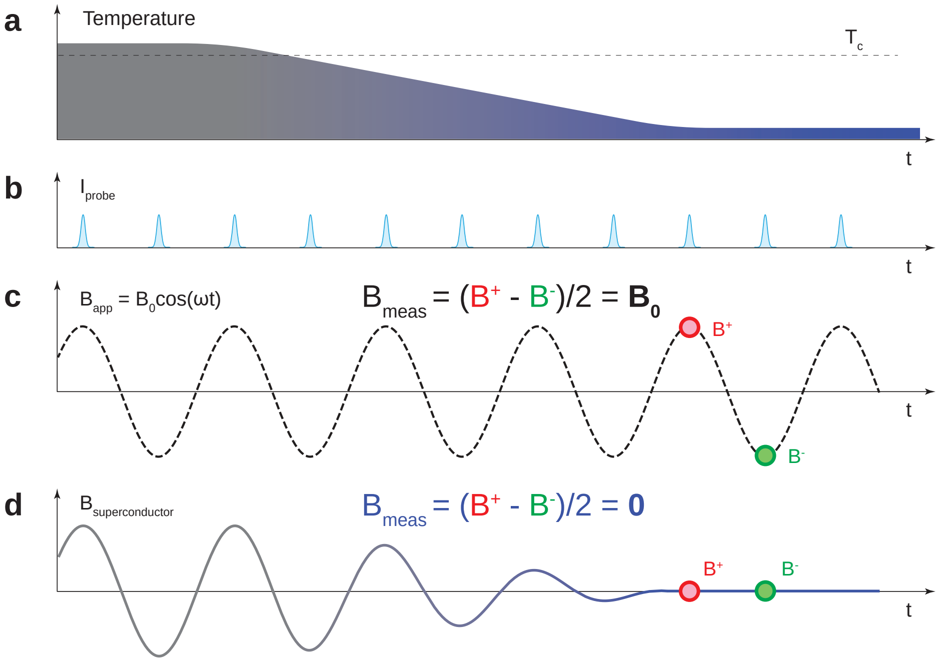

FIGURE F.1: **a**) Sketch of the temporal profile of the temperature when cooling the sample below T_c. **b**) Arrival time of the probe pulses sampling the magnetic field. **c**) Externally applied magnetic field with a sinusoidal time evolution. **d**) Magnetic shielding of the superconductor when cooling across T_c. Material from [47].

time-varying applied field. In this temperature regime close to T_c, the shielding is incomplete due to residual dissipation and the superconductor's low critical current density. Upon further cooling to lower temperatures, the shielding improves as the superfluid density increases and the superconductor behaves like a perfect metal in which the eddy currents induced by the applied field become persistent due to the absence of dissipation. In this regime of perfect screening, the field on top of the sample is constant, and our differential measurement yields a value of the magnetic field close to zero above the center of the superconductor as shown on the right panel of Figure 4.5.

Appendix G

Pump Induced Magnetic Field Dynamics at Long Time Scales

Figure 5.3 shows the ultrafast magnetic field changes induced by the quench pulse. Here, instead, we want to qualitatively discuss the evolution of the absolute value of the magnetic field, determined by long-lasting thermal effects induced by the optical quench pulse and by slow magnetic flux dynamics. We start discussing, in an ideal case, the evolution of the magnetic field in the superconductor, assuming that the quench beam has enough energy to disrupt entirely the superconductive shielding (Figure G.1). We then model the magnetic field dynamics when the quench beam disrupts superconductivity only partially and after factoring in the contributions due to our measurement geometry (Figures G.2 and G.3). This second case is relevant to the measurement shown in Figure 5.3 (which corresponds to the third shown in the left panel of Figure 7.2).

Before the first quench pulse arrives, the sample is kept below T_c. The magnetic field above the center of the superconductor is equal to zero as discussed in Appendix F (see the left panel of Figure G.1 showing that the magnetic field in the superconductor is zero before the first quench pulse arrives). When the first quench pulse hits the sample, the magnetic field above the center of the superconductor suddenly reaches the value of the external magnetic field, creating an ultrafast magnetic field step. The photo-excited sample will then thermalize and stay at a temperature higher than T_c until the heat is dissipated through the Al_2O_3 substrate. During this transient, the magnetic field is equal to the value of the externally applied magnetic field since no superconducting currents are available for the shielding above T_c. The superconductor then recovers in an applied magnetic field, which is trapped in the defects of the sample (as schematically indicated in the left panel of Figure 2.2). At this point, superconducting screening currents build up to shield any further change of the applied field and keep the value of the magnetic flux threading the sample constant (as prescribed by Faraday law) until the next pump pulse disrupts superconductivity again. At this point, the process described above repeats, and the magnetic field in the sample reaches the value of the externally applied field again on ultrafast timescales. Figure G.1 schematically depicts these dynamics and highlights the sign of the measured magnetic signal at negative (left panel) and positive (right panel) time delays. At negative delays, i.e., right before a quench pulse hits the sample, the trapped magnetic flux has a polarity opposite to the applied field's. This is why the measured magnetic field at negative pump-probe delays can be negative in our measurements, as the first two curves of the left panel of Figure 7.2 show. At positive time delays, the value of the magnetic field measured in the vicinity of the sample is positive and close to the value of the external applied field as observed at long pump-probe delays in the data taken at the highest fluence in Figure 7.2.

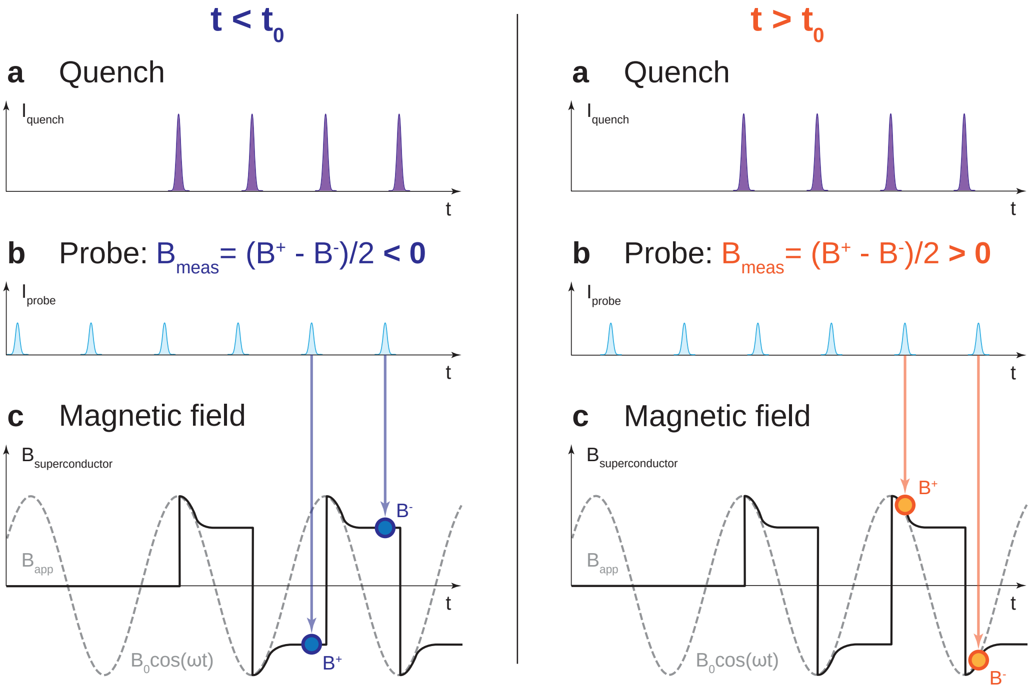

FIGURE G.1: Panel **a**) shows the arrival time of the quench pulses disrupting superconductivity in the sample (same in both the left and the right panels). **b**) Probe pulses sampling the magnetic field. In the left panel, the probe pulses arrive before the arrival time of the respective quench pulses (t_0), and the magnetic field measured is negative due to the presence of trapped flux with a polarity opposite to the externally applied field. In the right panel, the probe pulses arrive after the respective quench pulses ($t > t_0$), and the magnetic field measured is positive and close to the value of the external applied field. **c**) External applied magnetic field (dashed grey line) and magnetic field in the center of the superconductor (solid black curve). Material from [47].

We note that the presence of trapped magnetic flux with polarity opposite to the applied field, can also lead to a magnetic step having amplitude bigger (up to twice) than the amplitude of the external applied field (as hinted by the curves at highest fluence in Figure 7.2).

The data reported in Chapters 5 and 7 have been acquired in a condition in which the energy of the quench pulse is not sufficient to entirely disrupt the shielding currents in the superconductor. Moreover, to describe the signal, we also need to account for the finite distance from the superconducting sample at which the field is

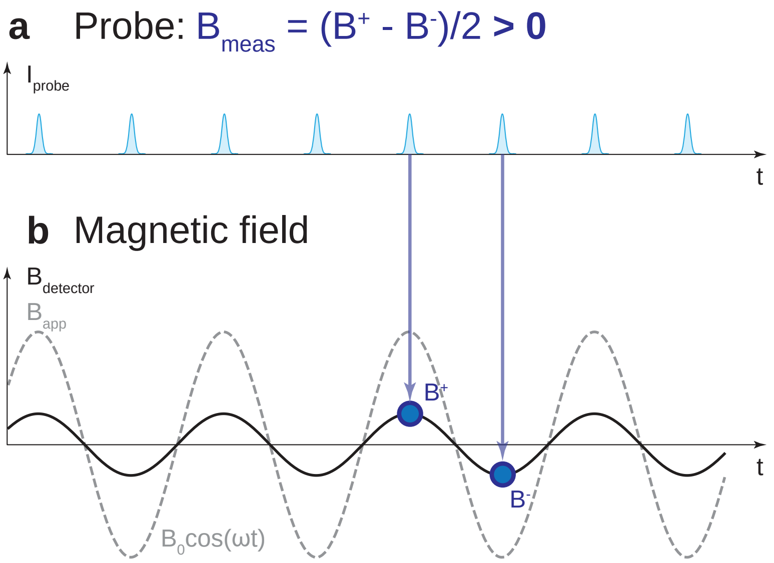

Figure G.2: **a**) Probe pulses sampling the magnetic field. The magnetic field measured in the detector is positive because the shielding is not perfect at finite distances from the superconductor. **b**) External applied magnetic field (dashed grey line) and magnetic field at the detector position above the center of the superconductor (solid black curve). Material from [47].

measured. In fact, the applied magnetic field at the detector is not completely shielded by the superconductor (see the left panel of Figure 4.5 and the relative discussion) as schematically depicted in Figure G.2. The combination of these two aspects gives rise to magnetic dynamics reported in Figure G.3. Here the magnetic field after the quench is not reaching the external field, giving rise to a magnetic step with lower amplitude, and the measured field at negative time delays has the same sign of the applied field because the trapped flux with negative polarity is offset by the applied field. This picture qualitatively describes the results shown in Figure 5.3 and in the third box of the left panel of Figure 7.2.

Finally, we present in Figure G.4 a possible alternative measurement protocol to avoid the presence of trapped flux at negative time delays. Here we assume that the quench pulses deposit enough energy on the sample to completely disrupt superconductivity and we apply a piecewise sinusoidal external magnetic field as shown by the dashed line in the last row of Figure G.4. In this way, we can use half of the quench pulses to "reset" the magnetic field of the superconductor to zero by quenching superconductivity in a zero applied magnetic field. The field is then measured with probe pulses arriving at half the repetition rate of the quench pulses (see the second row of Figure G.4). Thus, the field right above the superconductor at negative time delays is going to be zero.

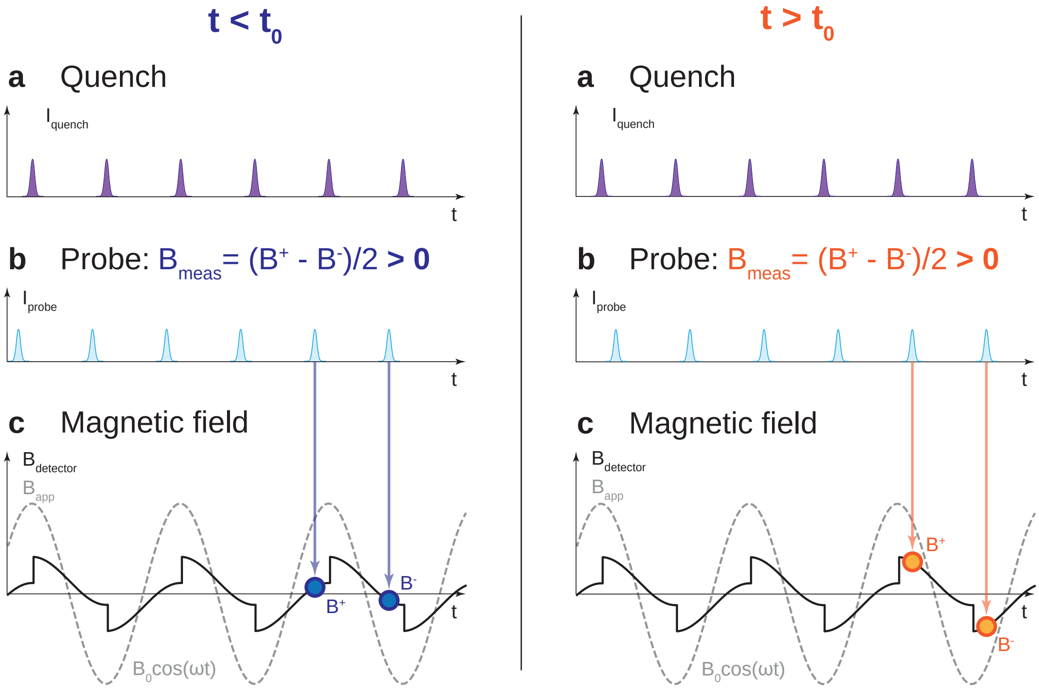

FIGURE G.3: **a**) Arrival time of the low fluence quench pulses disrupting superconductivity in the sample (same in both the left and the right panels). **b**) Probe pulses sampling the magnetic field. In the left panel the probe pulses arrive before the arrival time of the respective quench pulses (t0). At the specific fluence shown here the magnetic field measured is still positive as the trapped flux with opposite polarity is offset by the applied field. In the right panel the probe pulses arrive after the respective quench pulses (t>t0). The magnetic field measured is positive but not as big as the external field due to the only partial quench of superconductivity. **c**) Externally applied magnetic field (dashed grey line) and magnetic field at the detector position above the center of the superconductor (solid black curve). Material from [47].

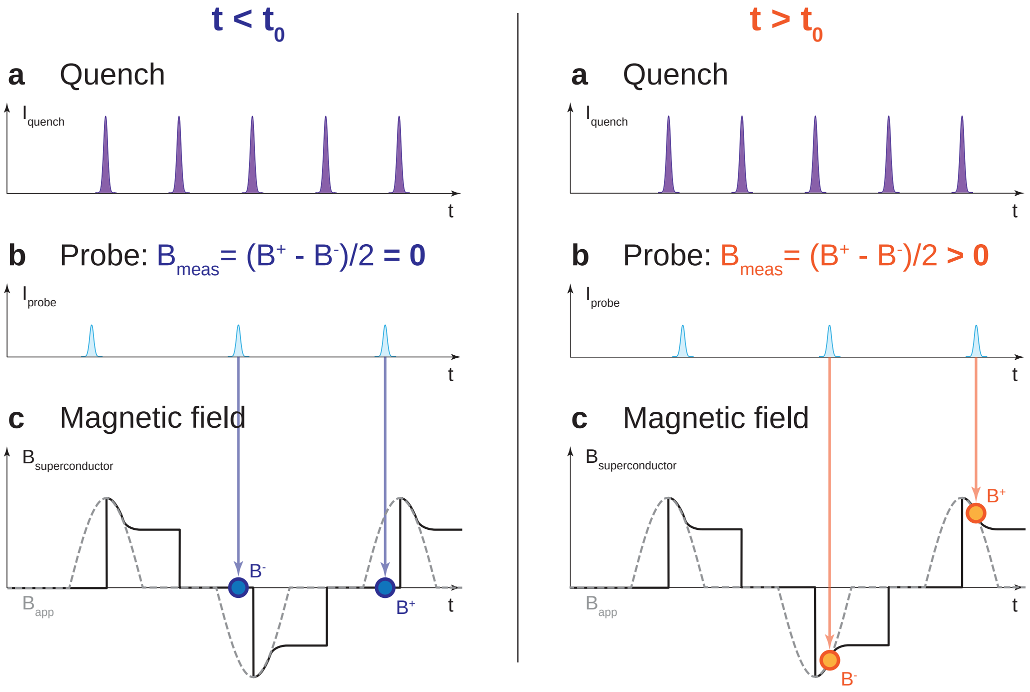

Figure G.4: **a**) Arrival time of the quench pulses disrupting superconductivity in the sample (same in both the left and the right panels). **b**) Probe pulses sampling the magnetic field at half the repetition rate of the quench pulse. In the left panel the probe pulses arrive before the arrival time of the respective quench pulses (t<t0) and the magnetic field at negative time delays is equal to zero with this experimental scheme. In the right panel the probe pulses arrive after the respective quench pulses (t>t0) and the magnetic field measured is positive and close to the value of the external applied field. **c**) External applied magnetic field (dashed grey line) and magnetic field in the center of the superconductor (solid black curve). Material from [47].

List of publications

This dissertation results from the author's work as a graduate student at the Max Planck Institute for the Structure and Dynamics of Matter, within the Quantum Condensed Matter Dynamics department in the group of Prof. Andrea Cavalleri and at the University of Hamburg. The scientific findings presented in this manuscript result in the following scientific publications[1]:

1. S. Fava*, G. De Vecchi*, G. Jotzu*, M. Buzzi*, T. Gebert, Y. Liu, B. Keimer, and A. Cavalleri, "Magnetic field expulsion in optically driven $YBa_2Cu_3O_{6.48}$". Nature 632, 75-80 (2024)
2. G. De Vecchi*, G. Jotzu*, M. Buzzi*, S. Fava*, T. Gebert, M. Fechner, A. Kimel, and A. Cavalleri, "Generation of Ultrafast Magnetic Steps for Coherent Control." arXiv:2408.05153 (2024)

Chapters 4, 5, 6, 7, and the Appendices are based on these publications.

---

[1] The symbol * indicates equal contributions

Acknowledgements

Now, I want to thank and acknowledge all the people without whom my PhD journey would not have been so unique and possible.

First, I want to thank Prof. Andrea Cavalleri. With open-mindedness and generosity, you gave me a second chance in science and the possibility to pursue a PhD in a world-class group like yours. I am very grateful for this. The opportunities and means you provide us are unmatched; I always had unlimited resources to do what I wanted, and my abilities or skills were the limiting factor. I admire your passion and curiosity for science, envy the perseverance with which you work towards your goals, and appreciate you helping me focus on essential aspects of my projects rather than getting lost in details. I am lucky to learn from you and the special people you chose for your group. After this challenging and fun process, I have improved intellectually and personally: this is what I wanted from my PhD, and I am satisfied with the results. I hope I contributed positively to the group and that you do not regret your choice of letting me work in your group.

Once again, I want to express my gratitude to Prof. Giacomo Ghiringhelli. Your passion for science made me decide to pursue a PhD (I still remember when you said during the celebration of Lucio's eightieth birthday that "the only real reason why we do science is that we like it"). You advised and helped me to join Andrea's group. I am glad I followed your advice.

A genuine thanks to Prof. Henning Moritz, my second PhD advisor. I really appreciate you taking your role in co-advising students seriously and making time for it. Your support and alternative point of view greatly influenced my steps and helped to put into perspective the downs during my PhD.

Next, I want to thank the people who worked closely with me and from whom I learned the most, retracing my journey in the group through the important acquaintances I made.

First, I met Thomas. You were why I started working on the Meissner effect in the K_3C_{60} project when you said you gave a group meeting talk "for me." I hate you a bit as well for dragging me into that project, but you were always fair and sincere with me, so I can only blame myself ;).

Then Gregor and I crossed paths, and I was impressed from the beginning. Working together on the same project was very stimulating; I learned much from you and found your motivation, ambition, and optimism commendable. I saw in you a "walking encyclopedia" for all my questions about the experiment or physics. The inevitable conflict of interest we had working together on a complex and stressful project will be forgotten, maybe in front of a beer. Still, the excellent work done together will stay.

Michele, you are the idealization of the experimental physicist. I am honored to have had the opportunity to work with and learn from you extensively. You should be proud and happy of your work and contribution to shaping the next generation of scientists; it makes a difference. You and Andrea complete each other and ultimately

are the perfect experimentalist team. I am looking forward to many more astonishing results to come.

Last but absolutely not least, Sebastian! You shared your results with me; I would not be writing my thesis now if it were not for that. I have always admired your lighthearted approach to life and the astonishing results you have achieved; I have much to learn from you! I wish you all the best with your adventure in Texas, and I want to keep our friendship alive so you can tell me about your following results and more...

Jack, hold high the honor of the magnetometry team together with Hangoo! I already know this wish is pointless. I do not doubt that you will do splendidly with your skills and dedication and achieve even more than you already have.

I also want to mention and thank Elena König, Toru Matsuyama, Boris Fiedler, and Guido Meier for all the technical support in the lab, for the help with simulations, and for the meaningful discussions and moments spent together. Your assistance and training made our research possible, I really appreciate that. I cannot forget Peter Licht, who is always ready to lend a helping hand with the necessary maintenance work behind experiments in the lab.

I also want to thank the group's scientists for helping on every occasion and teaching me so much. Michael Först, I hope we will perform a beamtime with positive results sooner or later. Michael Fechner, thanks for the insightful discussions about physics and bread baking. Daniele Nicoletti, having lunch together is always a fun experience. Eryin Wang, thank you for helping every time and for the kind discussions together.

Neda Lotfiomran, you are always on the side of the students, and you play a paramount role in our development. Your charismatic presence will be a crucial memory of my PhD, and the "threatening" reminders to submit our advisory panel documents on time, too.

Moreover, I appreciated working together with the entire team of the Quantum Condensed Matter Dynamics group; everybody here is, in his way, extraordinary. But I still want to mention some of them personally: Ankit, I really like your style in life and in doing experiments. I know you are already doing great in your new lab, but I still want to wish you all the best for the future. Kilian, I like how you carry yourself, your energy, and your curiosity about learning new things. I hope to have many more gym bro sessions together in the future. Danica, hang in there; results will come, and please keep your happy and kind (apart from the times we swore at each other at the kicker table) mood.

A big, big thank you, Renu, for what you are doing to keep the group happy and engaged. I really appreciate it, and it makes a big difference for everybody. It is not easy to make a group of scientists socialize, but your breakfasts, lunches, and cakes (!!!) have done it!

And now it's Albert's turn. My friendship with you will always be a defining part of my stay in Hamburg. The discussions about physics and life, the COVID Christmas dinner at CFEL, the legendary UFC Sunday breakfasts, and your "stylistic choices" about the gym dress code made my journey much more fun and fueled my energy. I hope we can go on holiday together if you do not ditch me for a third time ;).

Finally, I want to thank the people (and pets) who are dearest to me personally. My mother and my father, you always helped me and stayed close, making me feel at home even far from it and fueling me with good food when I came back. Laura, thank you so much for the moments together, the countless times I tried to explain what I do in my PhD you endured, the warming conversation at dinner, and your love. You made my life better and more fun (and sometimes more complicated, too ;)). We will continue our path and live many more adventures together. An honorable mention goes to the fluffy cats here in Hamburg, Fefe and Minka, waking us up at 4 a.m. for cuddles and food, respectively, and to our (spoiled) dog Uber back in Verona.

Bibliography

[1] D. Fausti et al. "Light-Induced Superconductivity in a Stripe-Ordered Cuprate". In: *Science* 331.6014 (Jan. 14, 2011).

[2] D. Nicoletti et al. "Optically Induced Superconductivity in Striped $La_{2-x}Ba_xCuO_4$ by Polarization-Selective Excitation in the near Infrared". In: *Physical Review B* 90.10 (Sept. 10, 2014).

[3] S. Kaiser et al. "Optically Induced Coherent Transport Far above T_c in Underdoped $YBa_2Cu_3O_{6+\delta}$". In: *Physical Review B* 89.18 (May 30, 2014).

[4] M. Mitrano et al. "Possible Light-Induced Superconductivity in K_3C_{60} at High Temperature". In: *Nature* 530.7591 (Feb. 2016).

[5] M. Buzzi et al. "Photomolecular High-Temperature Superconductivity". In: *Physical Review X* 10.3 (Aug. 6, 2020).

[6] Kazuki Isoyama et al. "Light-Induced Enhancement of Superconductivity in Iron-Based Superconductor $FeSe_{0.5}Te_{0.5}$". In: *Communications Physics* 4.1 (July 14, 2021).

[7] Michael Tinkham. *Introduction to Superconductivity*. Courier Corporation, Jan. 1, 2004. 482 pp.

[8] M. Budden et al. "Evidence for Metastable Photo-Induced Superconductivity in K_3C_{60}". In: *Nature Physics* 17.5 (May 2021).

[9] A. Ribak et al. "Two-Fluid Dynamics in Driven $YBa_2Cu_3O_{6.48}$". In: *Physical Review B* 107.10 (Mar. 13, 2023).

[10] E. Wang et al. "Superconducting Nonlinear Transport in Optically Driven High-Temperature K_3C_{60}". In: *Nature Communications* 14.1 (Nov. 9, 2023).

[11] Joseph D. Adelinia et al. *Probing Photo-Induced Granular Superconductivity in K_3C_{60} Thin Films with an Ultrafast on-Chip Voltmeter*. Dec. 11, 2023. arXiv: `2312.06421`. Pre-published.

[12] B. Liu et al. "Pump Frequency Resonances for Light-Induced Incipient Superconductivity in $YBa_2Cu_3O_{6.5}$". In: *Physical Review X* 10.1 (Mar. 3, 2020).

[13] J. Steven Dodge, Leya Lopez, and Derek G. Sahota. "Optical Saturation Produces Spurious Evidence for Photoinduced Superconductivity in K_3C_{60}". In: *Physical Review Letters* 130.14 (Apr. 3, 2023).

[14] B. Farnworth and T. Timusk. "Phonon Density of States of Superconducting Lead". In: *Physical Review B* 14.11 (Dec. 1, 1976).

[15] D. N. Basov et al. “C-Axis Response of $YBa_2Cu_4O_8$: A Pseudogap and Possibility of Josephson Coupling of CuO_2 Planes”. In: *Physical Review B* 50.5 (Aug. 1, 1994).

[16] Ronald Ulbricht. “Carrier Dynamics in Semiconductors Studied with Time-Resolved Terahertz Spectroscopy”. In: *Reviews of Modern Physics* 83.2 (2011).

[17] S. Fava et al. “Magnetic Field Expulsion in Optically Driven $YBa_2Cu_3O_{6.48}$”. In: *Nature* (July 10, 2024).

[18] J. File and R. G. Mills. “Observation of Persistent Current in a Superconducting Solenoid”. In: *Physical Review Letters* 10.3 (Feb. 1, 1963).

[19] Matthias Johannes Budden. “Metastable Light-Induced Superconductivity in K_3C_{60}”. doctoralThesis. Staats- und Universitätsbibliothek Hamburg Carl von Ossietzky, 2020.

[20] H. Kamerlingh Onnes. “Further Experiments with Liquid Helium. G. On the Electrical Resistance of Pure Metals, Etc. VI. On the Sudden Change in the Rate at Which the Resistance of Mercury Disappears.” In: *Through Measurement to Knowledge: The Selected Papers of Heike Kamerlingh Onnes 1853–1926*. Ed. by Heike Kamerlingh Onnes, Kostas Gavroglu, and Yorgos Goudaroulis. Dordrecht: Springer Netherlands, 1991.

[21] W. Meissner and R. Ochsenfeld. “Ein neuer Effekt bei Eintritt der Supraleitfähigkeit”. In: *Naturwissenschaften* 21.44 (Nov. 1, 1933).

[22] Stephen Blundell. *Magnetism in Condensed Matter*. Oxford Master Series in Physics. Oxford, New York: Oxford University Press, Oct. 4, 2001. 256 pp.

[23] R. Prozorov and V. G. Kogan. “Effective Demagnetizing Factors of Diamagnetic Samples of Various Shapes”. In: *Physical Review Applied* 10.1 (July 27, 2018).

[24] A. Gauzzi et al. “Scaling between Superconducting Critical Temperature and Structural Coherence Length in $YBa_2Cu_3O_{6.9}$ Films”. In: *Europhysics Letters* 51.6 (Sept. 15, 2000).

[25] J. Pearl. “Current Distribution in Superconducting Films Carrying Quantized Fluxoids”. In: *Applied Physics Letters* 5.4 (Aug. 15, 1964).

[26] A. A. Abrikosov. “On the Magnetic Properties of Superconductors of the Second Group”. In: *Sov. Phys. JETP* 5 (1957).

[27] Ch Jooss et al. “Magneto-Optical Studies of Current Distributions in High-Tc Superconductors”. In: *Reports on Progress in Physics* 65.5 (Apr. 2002).

[28] Y. Yuan, J. Theile, and J. Engemann. “Measurement of the Meissner Effect by a Magneto-Optic Ac Method Using Ferrimagnetic Garnet Films”. In: *Journal of Magnetism and Magnetic Materials* 95.1 (Apr. 1, 1991).

[29] Pål Erik Goa et al. “Real-Time Magneto-Optical Imaging of Vortices in Superconducting $NbSe_2$”. In: *Superconductor Science and Technology* 14.9 (Aug. 2001).

[30] M. R. Koblischka and R. J. Wijngaarden. “Magneto-Optical Investigations of Superconductors”. In: *Superconductor Science and Technology* 8.4 (Apr. 1995).

[31] P. E. Goa et al. “Magneto-Optical Imaging Setup for Single Vortex Observation”. In: *Review of Scientific Instruments* 74.1 (Jan. 1, 2003).

[32] M. R. Freeman. “Picosecond Studies of Nonequilibrium Flux Dynamics in a Superconductor”. In: *Physical Review Letters* 69.11 (Sept. 14, 1992).

[33] J. A. Riordan, Z. G. Lu, and X.-C. Zhang. “Free-Space Ultrafast Magneto-Optic Sampling”. In: *Conference on Lasers and Electro-Optics (1997), Paper CPD10.* Conference on Lasers and Electro-Optics. Optica Publishing Group, May 18, 1997.

[34] J.A. Riordan and X.-C. Zhang. “Sampling of Free-Space Magnetic Pulses”. In: *Optical and Quantum Electronics* 32.4 (May 1, 2000).

[35] D. F. Parsons and P. D. Coleman. “Far Infrared Optical Constants of Gallium Phosphide”. In: *Applied Optics* 10.7 (July 1, 1971).

[36] Herbert S. Bennett and Edward A. Stern. “Faraday Effect in Solids”. In: *Physical Review* 137 (2A Jan. 18, 1965).

[37] Merritt N. Deeter, Gordon W. Day, and Allen H. Rose. “Crystals and Glasses”. In: *CRC Handbook of Laser Science and Technology Supplement 2.* CRC Press, 1994.

[38] Martin Dressel and George Grüner. *Electrodynamics of Solids: Optical Properties of Electrons in Matter.* Cambridge: Cambridge University Press, 2002.

[39] Paul Fumagalli and Joachim Schoenes. *Magneto-Optics: An Introduction.* De Gruyter, Dec. 20, 2021.

[40] Charles Kittel. *Introduction to Solid State Physics. 8th Edition. Wiley.* Wiley.com.

[41] R. Merlin. *Unraveling the Effect of Circularly Polarized Light on Reciprocal Media: Breaking Time Reversal Symmetry with Non-Maxwellian Magnetic-esque Fields.* Oct. 13, 2023. arXiv: `2309.13622`. Pre-published.

[42] M. Basini et al. “Terahertz Electric-Field-Driven Dynamical Multiferroicity in $SrTiO_3$”. In: *Nature* 628.8008 (Apr. 2024).

[43] Jeffrey McCord. “Progress in Magnetic Domain Observation by Advanced Magneto-Optical Microscopy”. In: *Journal of Physics D: Applied Physics* 48.33 (Aug. 26, 2015).

[44] D. E. Aspnes and A. A. Studna. “Dielectric Functions and Optical Parameters of Si, Ge, GaP, GaAs, GaSb, InP, InAs, and InSb from 1.5 to 6.0 eV”. In: *Physical Review B* 27.2 (Jan. 15, 1983).

[45] H. Kirchner. “High-Resolution Magnetooptical Experiments on Magnetic Structures in Superconductors”. In: *Low Temperature Physics-LT 13: Volume 3: Superconductivity*. Ed. by K. D. Timmerhaus, W. J. O’Sullivan, and E. F. Hammel. Boston, MA: Springer US, 1974.

[46] P. Gierłowski et al. “London Penetration Depth of Electron-Irradiated $Ba_{0.47}K_{0.53}Fe_2As_2$”. In: *Physica C: Superconductivity and its Applications* 613 (Oct. 15, 2023).

[47] G. De Vecchi et al. *Generation of Ultrafast Magnetic Steps for Coherent Control*. Aug. 9, 2024. arXiv: `2408.05153`. Pre-published.

[48] Ernst Helmut Brandt and Mikhail Indenbom. “Type-II-superconductor Strip with Current in a Perpendicular Magnetic Field”. In: *Physical Review B* 48.17 (Nov. 1, 1993).

[49] E. H. Brandt. “Geometric Edge Barrier in the Shubnikov Phase of Type-II Superconductors”. In: *Low Temperature Physics* 27.9 (Sept. 1, 2001).

[50] Marwan Deb et al. “Picosecond Acoustic-Excitation-Driven Ultrafast Magnetization Dynamics in Dielectric Bi-substituted Yttrium Iron Garnet”. In: *Physical Review B* 98.17 (Nov. 6, 2018).

[51] T. G. H. Blank et al. “Effective Rectification of THz Electromagnetic Fields in a Ferrimagnetic Iron Garnet”. In: *Physical Review B* 108.9 (Sept. 28, 2023).

[52] Evgeny A. Mashkovich et al. “Terahertz-Driven Magnetization Dynamics of Bismuth-Substituted Yttrium Iron-Gallium Garnet Thin Film near a Compensation Point”. In: *Physical Review B* 106.18 (Nov. 30, 2022).

[53] T. Dietl et al. “Dynamics of Spin Organization in Diluted Magnetic Semiconductors”. In: *Physical Review Letters* 74.3 (Jan. 16, 1995).

[54] R. Rey de Castro et al. “Subpicosecond Faraday Effect in $Cd_{1\text{-}x}Mn_xTe$ and Its Application in Magneto-Optical Sampling”. In: *Applied Physics Letters* 85.17 (Oct. 25, 2004).

[55] Robert W. Boyd. *Nonlinear Optics*. 4th edition. London: Academic Press, Apr. 14, 2020.

[56] G. E. Jellison. “Optical Functions of GaAs, GaP, and Ge Determined by Two-Channel Polarization Modulation Ellipsometry”. In: *Optical Materials* 1.3 (Sept. 1, 1992).

[57] R. A. Kaindl et al. “Ultrafast Mid-Infrared Response of $YBa_2Cu_3O_{7\text{-}\delta}$”. In: *Science* 287.5452 (Jan. 21, 2000).

[58] R. D. Averitt et al. “Nonequilibrium Superconductivity and Quasiparticle Dynamics in $YBa_2Cu_3O_{7\text{-}\delta}$”. In: *Physical Review B* 63.14 (Mar. 12, 2001).

[59] J. Demsar et al. “Pair-Breaking and Superconducting State Recovery Dynamics in MgB_2”. In: *Physical Review Letters* 91.26 (Dec. 29, 2003).

[60] Robert A. Kaindl et al. “Dynamics of Cooper Pair Formation in $Bi_2Sr_2CaCu_2O_{8+\delta}$”. In: *Physical Review B* 72.6 (Aug. 25, 2005).

[61] A. Pashkin et al. “Femtosecond Response of Quasiparticles and Phonons in Superconducting $YBa_2Cu_3O_{7\text{-}\delta}$ Studied by Wideband Terahertz Spectroscopy”. In: *Physical Review Letters* 105.6 (Aug. 2, 2010).

[62] J. Demsar. “Non-Equilibrium Phenomena in Superconductors Probed by Femtosecond Time-Domain Spectroscopy”. In: *Journal of Low Temperature Physics* 201.5 (Dec. 1, 2020).

[63] E. Rowe et al. “Resonant Enhancement of Photo-Induced Superconductivity in K_3C_{60}”. In: *Nature Physics* 19.12 (Dec. 2023).

[64] D. You and P. H. Bucksbaum. “Propagation of Half-Cycle Far Infrared Pulses”. In: *JOSA B* 14.7 (July 1, 1997).

[65] A. von Hoegen et al. “Amplification of Superconducting Fluctuations in Driven $YBa_2Cu_3O_{6+x}$”. In: *Physical Review X* 12.3 (July 13, 2022).

[66] J. E. Hirsch. *On the Dynamics of the Meissner Effect*. Aug. 13, 2015. arXiv: `1508.03307`. Pre-published.

[67] C. H. Back et al. “Magnetization Reversal in Ultrashort Magnetic Field Pulses”. In: *Physical Review Letters* 81.15 (Oct. 12, 1998).

[68] C. H. Back et al. “Minimum Field Strength in Precessional Magnetization Reversal”. In: *Science* 285.5429 (Aug. 6, 1999).

[69] C. S. Davies et al. “Helicity-Independent All-Optical Switching of Magnetization in Ferrimagnetic Alloys”. In: *Journal of Magnetism and Magnetic Materials* 563 (Dec. 1, 2022).

[70] Alexey V. Kimel and Mo Li. “Writing Magnetic Memory with Ultrashort Light Pulses”. In: *Nature Reviews Materials* 4.3 (Mar. 2019).

[71] A. V. Kimel et al. “Fundamentals and Perspectives of Ultrafast Photoferroic Recording”. In: *Physics Reports*. Fundamentals and Perspectives of Ultrafast Photoferroic Recording 852 (Apr. 10, 2020).

[72] T. Zalewski et al. “Ultrafast All-Optical Toggle Writing of Magnetic Bits without Relying on Heat”. In: *Nature Communications* 15.1 (May 24, 2024).

[73] A. Yu. Galkin and B. A. Ivanov. “Dynamics of Antiferromagnets Exposed to Ultrashort Magnetic Field Pulses”. In: *JETP Letters* 88.4 (Oct. 1, 2008).

[74] S. V. Aradhya et al. “Nanosecond-Timescale Low Energy Switching of In-Plane Magnetic Tunnel Junctions through Dynamic Oersted-Field-Assisted Spin Hall Effect”. In: *Nano Letters* 16.10 (Oct. 12, 2016).

[75] H. Bourne, T. Kusuda, and Wei-Hau Wu. “The Effect of Pulse Rise Time on Nanosecond Switching in Magnetic Thin Films”. In: *IEEE Transactions on Magnetics* 6.2 (June 1970).

[76] Nobuaki Kikuchi et al. “Pulse Rise Time Dependence of Switching Field of Co/Pt Multilayer Dot”. In: *Electronics and Communications in Japan* 96.12 (2013).

[77] Zhao Wang et al. “Spin Dynamics Triggered by Subterahertz Magnetic Field Pulses”. In: *Journal of Applied Physics* 103.12 (June 18, 2008).

[78] D. Krökel, D. Grischkowsky, and M. B. Ketchen. “Subpicosecond Electrical Pulse Generation Using Photoconductive Switches with Long Carrier Lifetimes”. In: *Applied Physics Letters* 54.11 (Mar. 13, 1989).

[79] D. H. Auston. “Picosecond Optoelectronic Switching and Gating in Silicon”. In: *Applied Physics Letters* 26.3 (Feb. 1, 1975).

[80] Ho-Jin Song and Tadao Nagatsuma, eds. *Handbook of Terahertz Technologies: Devices and Applications.* New York: Jenny Stanford Publishing, Apr. 28, 2015. 612 pp.

[81] H. Hirori et al. “Single-Cycle Terahertz Pulses with Amplitudes Exceeding 1 MV/Cm Generated by Optical Rectification in $LiNbO_3$”. In: *Applied Physics Letters* 98.9 (Mar. 2, 2011).

[82] János Hebling et al. “Velocity Matching by Pulse Front Tilting for Large-Area THz-pulse Generation”. In: *Optics Express* 10.21 (Oct. 21, 2002).

[83] Ka-Lo Yeh et al. “Generation of High Average Power 1 kHz Shaped THz Pulses via Optical Rectification”. In: *Optics Communications* 281.13 (July 1, 2008).

[84] Charles P. Poole Ruslan Prozorov. *Superconductivity.* July 22, 2014.

[85] K. Winzer and G. Kumm. “Fluctuation-Enhanced Conductivity and Magnetoconductivity of High-Quality $YBa_2Cu_3O_{7-\delta}$ Crystals”. In: *Zeitschrift für Physik B Condensed Matter* 82.3 (Oct. 1, 1991).

[86] J. Krupka et al. “Complex Conductivity of YBCO Films in Normal and Superconducting States Probed by Microwave Measurements”. In: *IEEE Transactions on Applied Superconductivity* 23.2 (Apr. 2013).

[87] Fredrik Hansteen et al. “Optical and Magnetooptical Properties of Bismuth and Gallium Substituted Iron Garnet Films”. In: *Thin Solid Films.* The 3rd International Conference on Spectroscopic Ellipsometry 455–456 (May 1, 2004).

[88] P. Hansen, K. Witter, and W. Tolksdorf. “Magnetic and Magneto-Optic Properties of Lead- and Bismuth-Substituted Yttrium Iron Garnet Films”. In: *Physical Review B* 27.11 (June 1, 1983).

[89] A. R. Will-Cole et al. “Negligible Magnetic Losses at Low Temperatures in Liquid Phase Epitaxy Grown $Y_3Fe_5O_{12}$ Films”. In: *Physical Review Materials* 7.5 (May 31, 2023).

[90] Kin Fai Mak, Jie Shan, and Daniel C. Ralph. “Probing and Controlling Magnetic States in 2D Layered Magnetic Materials”. In: *Nature Reviews Physics* 1.11 (11 Nov. 2019).

[91] E. Beaurepaire et al. “Ultrafast Spin Dynamics in Ferromagnetic Nickel”. In: *Physical Review Letters* 76.22 (May 27, 1996).

[92] Katja Höflich et al. “Roadmap for Focused Ion Beam Technologies”. In: *Applied Physics Reviews* 10.4 (Dec. 26, 2023).

[93] C. E. Gough et al. “Flux Quantization in a High-Tc Superconductor”. In: *Nature* 326.6116 (Apr. 1987).

[94] T. F. Nova et al. “An Effective Magnetic Field from Optically Driven Phonons”. In: *Nature Physics* 13.2 (Feb. 2017).

[95] C. S. Davies et al. “Phononic Switching of Magnetization by the Ultrafast Barnett Effect”. In: *Nature* 628.8008 (Apr. 2024).

[96] Dominik M. Juraschek and Nicola A. Spaldin. “Orbital Magnetic Moments of Phonons”. In: *Physical Review Materials* 3.6 (June 6, 2019).

[97] S. R. Tauchert et al. “Polarized Phonons Carry Angular Momentum in Ultrafast Demagnetization”. In: *Nature* 602.7895 (Feb. 2022).

[98] K. v. Klitzing, G. Dorda, and M. Pepper. “New Method for High-Accuracy Determination of the Fine-Structure Constant Based on Quantized Hall Resistance”. In: *Physical Review Letters* 45.6 (Aug. 11, 1980).

[99] Tao Wu et al. “Magnetic-Field-Induced Charge-Stripe Order in the High-Temperature Superconductor $\mathrm{YBa_2Cu_3O_y}$”. In: *Nature* 477.7363 (Sept. 2011).

[100] Brian B. Zhou et al. “Spatiotemporal Mapping of a Photocurrent Vortex in Monolayer $\mathrm{MoS_2}$ Using Diamond Quantum Sensors”. In: *Physical Review X* 10.1 (Jan. 6, 2020).

[101] S. Castelletto et al. “Quantum Systems in Silicon Carbide for Sensing Applications”. In: *Reports on Progress in Physics* 87.1 (Dec. 2023).

[102] W. C. Lee and D. C. Johnston. “Superconducting and Normal-State Magnetic-Susceptibility Anisotropy in $\mathrm{YBa_2Cu_3O_7}$”. In: *Physical Review B* 41.4 (Feb. 1, 1990).

[103] Ruixing Liang et al. “Lower Critical Fields in an Ellipsoid-Shaped $\mathrm{YBa_2Cu_3O_{6.95}}$ Single Crystal”. In: *Physical Review B* 50.6 (Aug. 1, 1994).

[104] Ruslan Prozorov. “Meissner-London Susceptibility of Superconducting Right Circular Cylinders in an Axial Magnetic Field”. In: *Physical Review Applied* 16.2 (Aug. 9, 2021).